Report

Full of Economic-Environment Linkages and Integration dX/dt (FeliX)

Technical Model Documentation

Sibel Eker, Quanliang Ye, Ryan Tan, Deepthi Swamy, Qi Liu

October 2025

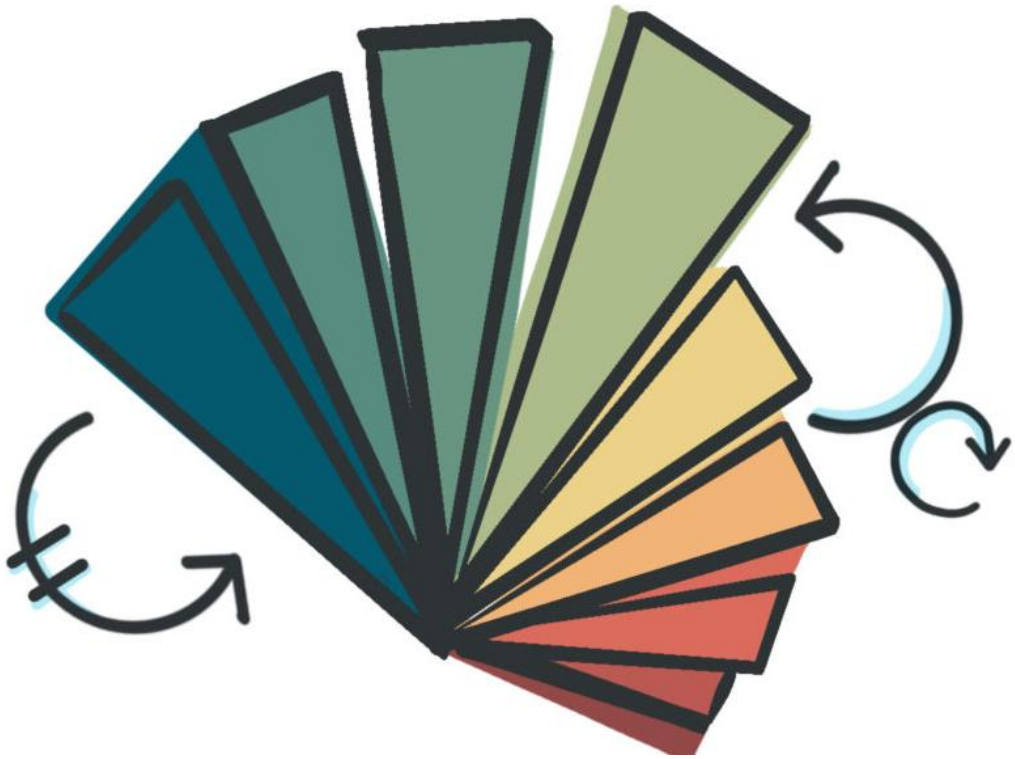

Table of contents

Abstract

FeliX is a global system dynamics model of climate, economy, environment and society that has been used to explore the long-term implications of human-earth system feedbacks in the context of climate change mitigation and sustainable development. This technical report documents the 12 core modules of the FeliX model, as well as a brief description of its regional version (FeliX-R5). In addition to the model description, the report includes a detailed explanation of the three baseline scenarios that are calibrated based on SSP1-3 yet include also the climate damages. This document is complementary to the peer-reviewed publications and can be referred to as a technical guide. An online version of the FeliX documentation can be seen on https://iiasa.github.io/felix_docs/.

About the authors

Sibel Eker is a Senior Research Scholar at IIASA's Energy, Climate and Environment Program. (Contact: eker@iiasa.ac.at)

Quanliang Ye is a Research Scholar at IIASA's Energy, Climate and Environment Program. (Contact: yequanliang@iiasa.ac.at)

Ryan Yi Wei Tan is a Researcher at IIASA's Energy, Climate and Environment Program. (Contact: tanryan@iiasa.ac.at)

Deepthi Swamy is a Research Scholar at IIASA's Energy, Climate and Environment Program. (Contact**:** swamy@iiasa.ac.at**)**

Qi Liu is a Researcher at Sichuan University, China, and a Guest Research Scholar at IIASA's Economic Frontiers Program. (Contact: liuqi@iiasa.ac.at; liuqi_67@stu.scu.edu.cn)

Acknowledgments

We are grateful to colleagues who contributed to the past model development and documentation: Felicjan Rydzak, Brian Walsh, Michael Obersteiner, Claudia Reiter, Michael Kuhn.

The authors gratefully acknowledge funding from the European Research Council for the research project 'TRANSPARENT ASSESSMENTS FOR REAL PEOPLE' (WorldTrans, 101081661), and 'Innovative Integrated Assessment Models for The Food Sector' (CHOICE, 101081617).

1. Introduction and Model Overview

Global modelling has long been an indispensable tool for understanding the interdependencies between social, economic, and environmental systems and exploring plausible future dynamics created by those (Meadows et al., 1983). FeliX is one of such models developed at IIASA first in 2006-2009 to support global earth observations within the GEO-BENE project funded by the European Commission. It is a globally aggregate, feedback-rich simulation model of climate, economy, environment, and society. FeliX has been used in various projects since then, for instance, to assess the socio-economic and environmental impacts of earth observation improvement (Obersteiner et al., 2012; Rydzak et al., 2010), to explore emission pathways when microalgae is used as a feedstock in livestock production (Walsh et al., 2015), and to analyze carbon cycle impacts of global emission pathways (Walsh et al., 2017; Walsh et al., 2015), and population dynamics of shifts to sustainable diets (Eker et al., 2019). The feedback-rich broad scope of FeliX has also enabled analyzing synergies and tradeoffs between sustainable development goals (SDGs) in long-term pathways beyond 2030 (Moallemi et al., 2022), and specifically the tradeoffs between environmental pressures and eradicating global poverty (Liu et al., 2023).

The FeliX model captures the core physical and anthropogenic mechanisms of global environmental and economic change within and between population, economy, energy, carbon cycle, climate, biodiversity, water, and land use. Figure 1 shows an overview of the main sectors in the model and their interconnections. Those cross-sectorial interconnections include the major human-earth system feedbacks, such as climate impacts on economic growth, crop yields, and human mortality or the impacts of economic growth on population dynamics, which are not endogenously covered in many global models.

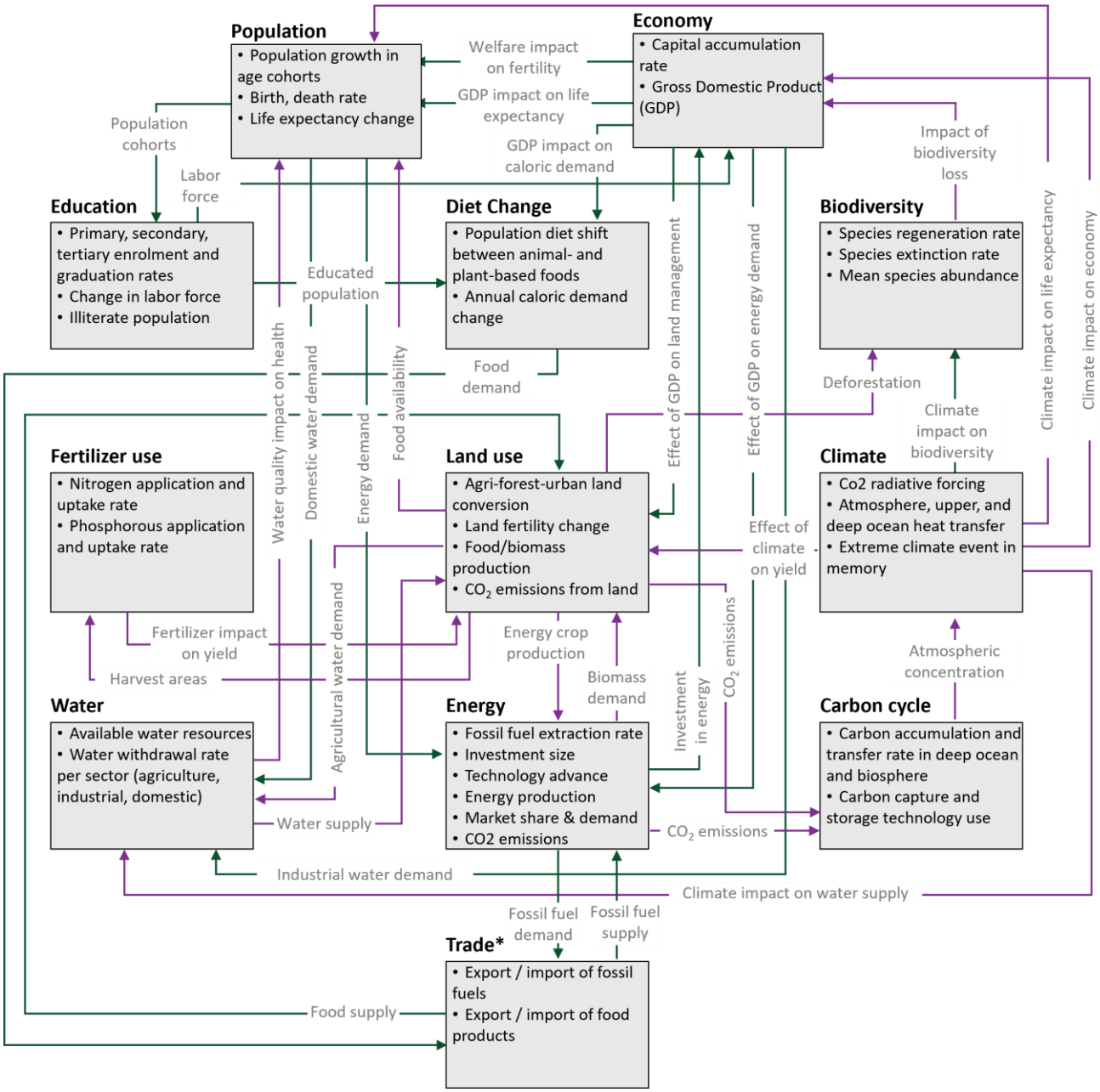

Figure 1: Overview of the FeliX model. Modified based on the figure in *Moallemi et al. (2022)*.

2. Population

The FeliX model has an endogenous population module that was conceptualized around two main dynamic mechanisms: population development and population ageing. Population development is governed by two key feedback loops visualized in Figure 2. The positive feedback loop describes the population growth mechanism: A growing *Population* leads to a higher economic output expressed in *Gross World Product (GWP) per capita*. This economic growth increases the *life expectancy at birth*, reduces mortality, and hence further increases the population. The two negative feedback loops describe the balancing effect of economic growth on population: *Fertility rates* decline as *GWP per capita* and educational attainment (expressed in the *Mean Years of Schooling* metric) increase. The population module connects several cross-system feedback loops, for instance through the effect of food supply per capita or climate change on life expectancy, or through the effects of educational attainment on dietary behavior and poverty rate. The sections below describe how the population module is formalized in the FeliX model.

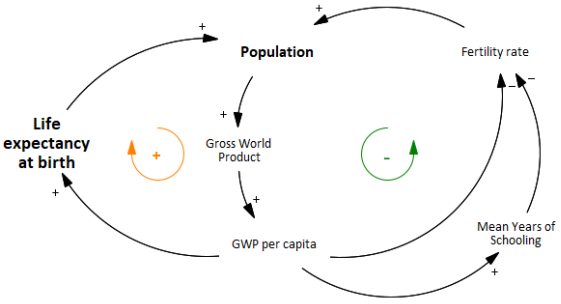

Figure 2: Main feedback loops in the population module

2.1. Ageing structure

This module describes population growth and population ageing based on an ageing chain and computes the male and female population size of 5-year age intervals between the ages of 0 and 100+. The chain structure in the model represents the transition of newborns through the age cohorts as they age, meaning that each age cohort except the "0–5" cohort has one inflow (maturation of the previous cohort) and two outflows (maturation to the next cohort and mortality). Figure 3 depicts this ageing chain, and the implementation of it on Vensim uses a compact form with subscripts. *Population* of each gender and age interval ($Population_{ij}$) is conceptualized in a stock variable that represents the accumulations, with three flows determining the net rate of change ($dPopulation_{ij}/dt$). These three flows are *birth rate* ($Birth_{ij}$), death rate ($Death_{ij}$) and maturation rate ($Maturation_{ij}$). Equation 2.1 shows the formulation of this net rate of change in the population depending on the age intervals, where the index ***i* refers to gender and *j* refers to age**. The maturation rate of each age group, that is, the transition to the next age interval, is formulated as the division of *Population* by the interval duration as in Equation 2.2, assuming a homogenous distribution of population within the age group. *Interval duration* is a parameter equal to 5 years.

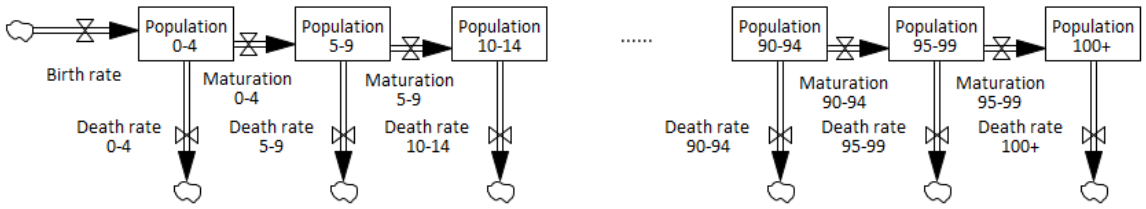

Figure 3: Ageing chain structure of the population module

$$\frac{dPopulation_{ij}(t)}{dt} = \begin{cases} Birth_i(t) - Maturation_{ij}(t) - Death_{ij}(t) \;\; ; if \;\; j = "0-4" \\ Maturation_{ij-1}(t) - Maturation_{ij}(t) - Death_{ij}(t) \;\; ; \;\; if \; "5\text{-}9" \leq j \leq "95\text{-}99" \\ Maturation_{ij-1}(t) - Death_{ij}(t) \;\; ; \; if \; j = "100+" \end{cases} \quad (2.1)$$

$$Maturation_{ij}(t) = \frac{Population_{i,}(t)}{Interval\ duration} \quad (2.2)$$

2.2. Birth rate and fertility

The birth rate[1], driven by education and gross domestic product (GDP) per capita, is the main factor affecting population dynamics (either growth or decline), alongside the reproductive female population represented by gender and age-cohort segmentation in the model. Equation 2.3 shows the formulation of *birth rate* per year, where the parameter g_i denotes the birth gender fraction, hence female infanticide, and the parameter *age interval duration* is 5 years. The numerator in the equation refers to the total births in a 5-year interval, formulated as the sum of births for women in each 5-year age interval between 15 and 50. $ASFR_j$ refers to the *Age-Specific Fertility Rate*, that is, number of births per woman in a particular age group during a five-year period. *ASFR* is formulated as a function of *Total Fertility* as shown in Equation 2.4, in order to take the effects of education and wealth on fertility into account in an aggregate manner. The functions representing the relationship between *ASFR* and *Total Fertility* are formulated as logistic functions and estimated based on historical relationships (including SSP2 projections) obtained from the Wittgenstein Centre Human Capital Data Explorer, as shown in Figure 4.

$$Birth_i(t) = g_i \times \frac{\sum_{j=15-19}^{45-49} Population_{female,j}(t) \times ASFR_j(t)}{Age\ interval\ duration} \quad (2.3)$$

$$ASFR_j(t) = f_j^{asfr}\big(Total\ Fertility(t)\big) \quad (2.4)$$

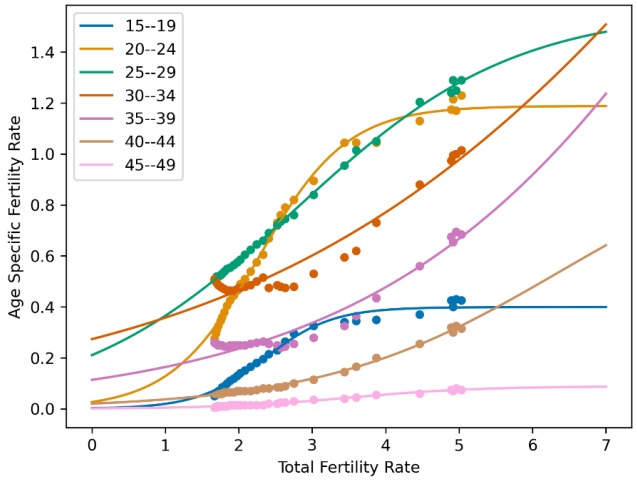

Age	R2
15--19	0.983
20--24	0.994
25--29	0.999
30--34	0.935
35--39	0.948
40--44	0.996
45--49	0.986

Figure 4: Relationship between Age-Specific Fertility Rate and Total Fertility. Dots refer to the N=30 historical data points SSP2 projections in 5-year intervals between 1955-2100 obtained from Wittgenstein Centre Human Capital Data Explorer. The lines show the logistic curve (f^{asfr}) fit to the historical data for each age interval in the reproductive period, and the right-hand-side table shows the R-squared values of the fitted curves.

Total Fertility represents the number of births per woman at reproductive age (15-50). It is formulated as a multiplicative function of *GWP per capita* and *Mean Years of Schooling (MYS)*. This formulation prevents a strong assumption on the monotonic dependence of fertility solely on economic output or solely on education.

[1] In system dynamics modelling, the term *rate* refers to the rate of change in a stock variable, that is, a flow. Therefore, here we use the term *rate* to refer to the flows, not to the fractions as used in demography.

Equation 2.5 shows this formulation, where *Normal Fertility* is the reference value equal to the historical value in year 2000, which is 2.63 births per woman.

$$Total\ Fertility(t) = Normal\ Fertility \times Impact_{fertility}^{education}(t) \times Impact_{fertility}^{GDP}(t) \quad (2.5)$$

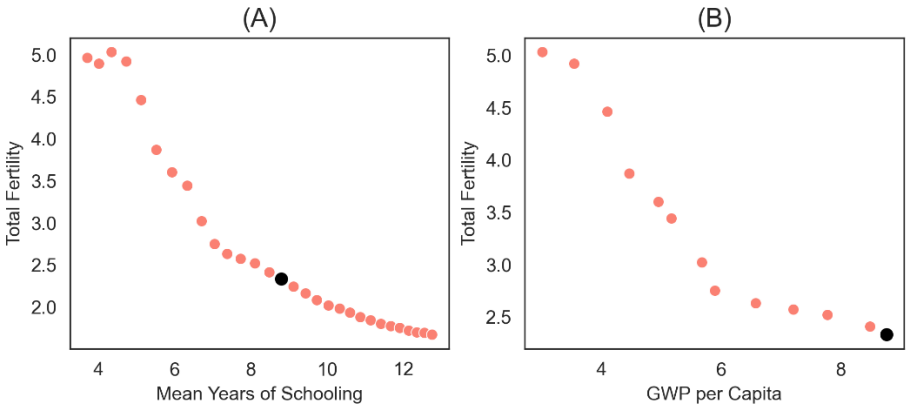

Figure 5: Observed relationship between fertility rate and its two drivers: **(A)** The relationship between the global average Total Fertility Rate (births per woman at the reproductive age) and Mean Years of Schooling based on the historical data of 1950-2015 and SSP2 projections for 2015-2100 of Wittgenstein Centre Human Capital Data Explorer (Lutz et al., 2018). **(B)** The relationship between the global average Total Fertility Rate and the GWP per Capita between the years 1960-2020. GWP per Capita is measured in 1000 USD 2005 PPP and obtained from World Bank data (The World Bank, 2023). The black dot shows the 2020 values.

Impact of Education on Fertility ($Impact_{fertility}^{education}$) is a nonlinear function that depends on global average *Mean Years of Schooling* (*MYS*) as formulated in Equation 2.6. In this formula, *L, k and* x_0 refer to the saturation, steepness and inflection point of the logistic curve, respectively. *MYS** is a normalized form of the model variable *Mean Years of Schooling,* that is, $MYS(t)/MYS_{2000}$, in order to make both Total Fertility and its drivers variable with respect to their values in year 2000. A functional form representing logarithmic decline is chosen, following the observed MYS-fertility relationship shown in Figure 5a. Similarly, *Impact of GDP on Fertility* ($Impact_{fertility}^{GDP}$) is a nonlinear (logistic) function that depends on *Gross World Product (GWP) per Capita* as formulated in Equation 2.7. This function form is chosen to represent the observed GDP-fertility relationship shown in Figure 5b. *GWP per Capita** is a normalized form of the model variable *GWP per Capita,* that is, $GWP\ per\ Capita(t)/GWP\ per\ Capita_{2000}$.

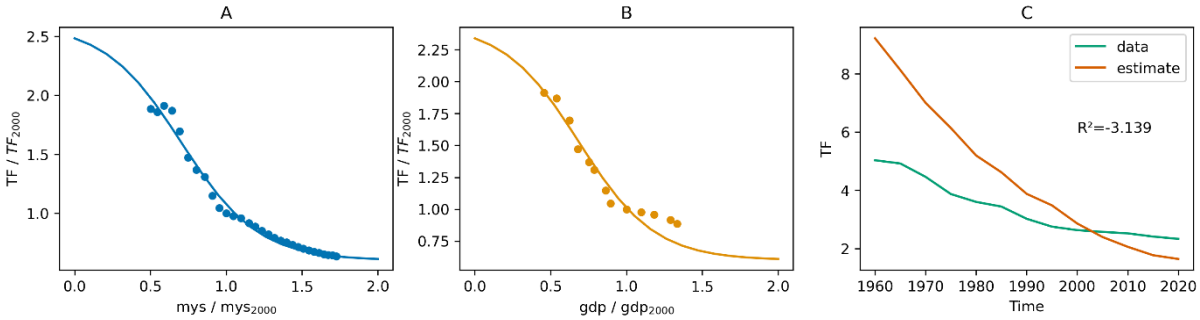

Figure 6: Step 1 of the calibration of the relations between Total Fertility and MYS and GWP per Capita. **(A)** The relationship between normalized Total Fertility Rate (y-axis) and normalized Mean Years of Schooling (x-axis). The dots refer to the historical data of 1950-2015 and SSP2 projections for 2015-2100 of Wittgenstein Centre Human Capital Data Explorer (Lutz et al., 2018). The line shows the logistic curve fitted to these data with R^2=0.985. **(B)** The relationship between normalized Total Fertility Rate (y-axis) and normalized GWP per Capita (x-axis). The dots refer to the historical data between 1960-2020 obtained from World Bank data (The World

Bank, 2023). The line shows the logistic curve fitted to these data with R^2=0.932. **(C)** Total Fertility rate over time as observed in historical data (green line) and as estimated according to Equation (2.5) and calibrated functions shown in (A) and (B).

$$Impact_{fertility}^{education}(t) = L_{0,edu} + \frac{L_{fer}^{edu}}{1 + e^{-k_{fer}^{edu} \times \left(MYS^*(t) - x0_{fer}^{edu}\right)}} \tag{2.6}$$

$$Impact_{fertility}^{GDP}(t) = L_{0,gdp} + \frac{L_{fer}^{gdp}}{1 + e^{-k_{fer}^{gdp} \times \left(GWP\ per\ Capita^*(t) - x0_{fer}^{gdp}\right)}} \tag{2.7}$$

Figure 6a and Figure 6b show the model functions denoted in Equations 2.6 and 2.7, respectively, of which parameters are calibrated according to the historical values. Since these *Step 1* calibrations do not take the joint effect of MYS and GWP into account, the resulting *Total Fertility* is far different from the observed values, as Figure 6c shows. To take the joint effect into account with a lower degree of freedom, we keep the parameters representing steepness and inflection of these functions (k_{edu}, $x_{0,edu}$, k_{gdp}, $x_{0,gdp}$) at the values obtained from the regression in Step 1 and re-calibrate the parameters representing the scale of the impacts (L_{edu} and L_{gdp}) to the historical values of total fertility. The resulting estimate of *Total Fertility* is shown in Figure 7c, and the updated functional forms of the impact of education and GDP are shown in Figure 7a and Figure 7b, respectively. These constitute the final model functions.

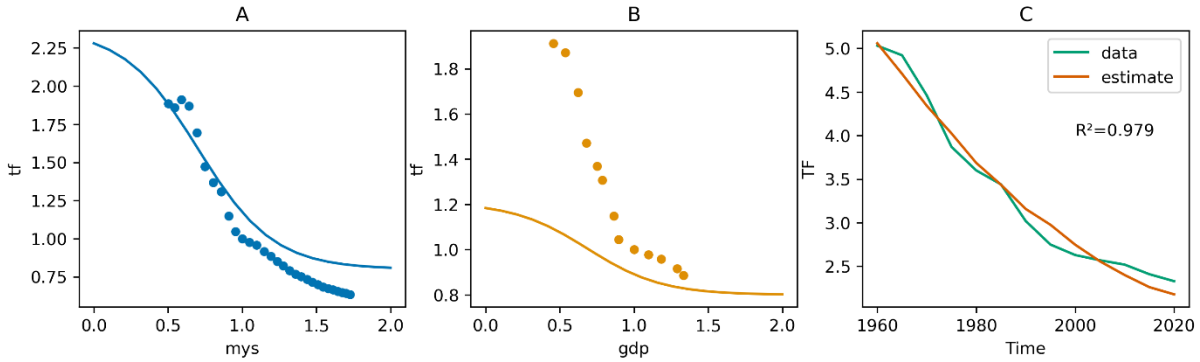

Figure 7: Step 2 of the calibration of the relations between Total Fertility and MYS and GWP per Capita. **(A and B)** The relationship between normalized Total Fertility Rate (y-axis) and normalized Mean Years of Schooling (x-axis, A) and normalized GWP per Capita (x-axis, B), respectively. The dots refer to the historical data. The lines show the logistic curve resulting from the fit of the parameters L_{edu} and L_{gdp}, whereas the other parameters are kept at the values obtained in Step 1 (Figure 6). **(C)** Total Fertility rate over time as observed in historical data (green line) and as estimated according to Equation (2.5) and calibrated functions shown in (A) and (B).

Based on the functional forms and calibration described above, the reference simulation of the model generates the trajectories for global average *Total Fertility* and *global Total Birth Rate* shown in Figure 8.

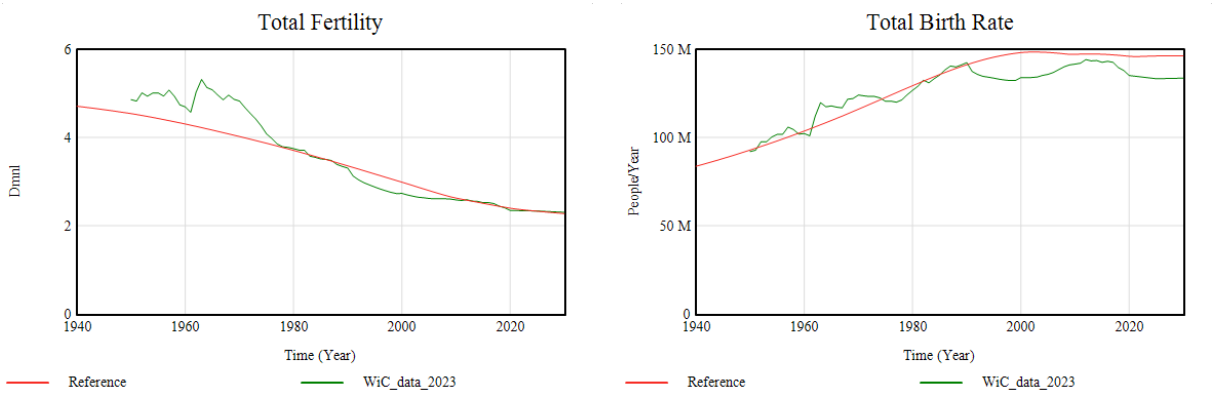

Figure 8: Reference simulation results (BAU, red line) and historical data (Data, green line) of Total Fertility and Total Birth Rate. The data for Total Fertility is obtained from Wittgenstein Centre Human Capital Data Explorer (Lutz et al., 2018). The data for Total Birth Rate is obtained from UN Population Prospects (United Nations, 2022).

2.3. Mortality rate and life expectancy at birth

Death rate (*Death*$_{ij}$) refers to the number of people who pass away in each demographic gender and age group per year. It is formulated as a fraction of the population of each group as Equation 2.8 shows, where *M*$_{ij,}$ denotes the mortality fraction. The mortality fraction for each age and gender group is assumed to be a function of global average life expectancy at birth (*LE*) (Equation 2.9). This assumption reflects the relationship between life expectancy and wider socioeconomic and environmental factors, such as education, wealth, climate change, aggregately; and, in turn, their relationship with mortality rates.

$$Death_{ij}(t) = Population_{ij}(t) \times M_{ij}(t) \tag{2.8}$$

$$M_{ij}(t) = Mor_{ij}(t) + \frac{L\,mor_{ij}}{1 + e^{\left(-K\,mor_{i,j} \times \left(\frac{LE(t)}{LE^*} - x_0\,mor_{ij}\right)\right)}} \tag{2.9}$$

LE^* is a reference value of life expectancy at birth used for normalization, and currently 28.8, referring to the values at the beginning of the 20th century. Mor_{ij}, $L\,mor_{ij}$, $K\,mor_{ij}$, and $x_0\,mor_{ij}$ are parameters obtained by the model calibration of mortality fractions. The model calibration of mortality fractions is conducted by fitting the model simulation results and historical data of each gender and age group. The historical data of the mortality fraction of each gender and age group is collected from UN Population Prospects (United Nations, 2022). Figure 9 shows the calibration results for the mortality fraction of each gender and age group, and Table 1 lists the R^2 values of the fit between the model output and historical data (including UN projections until 2100). It is important to note that climate impacts on mortality are not taken into account in this calibration, since the projections do not include it either.

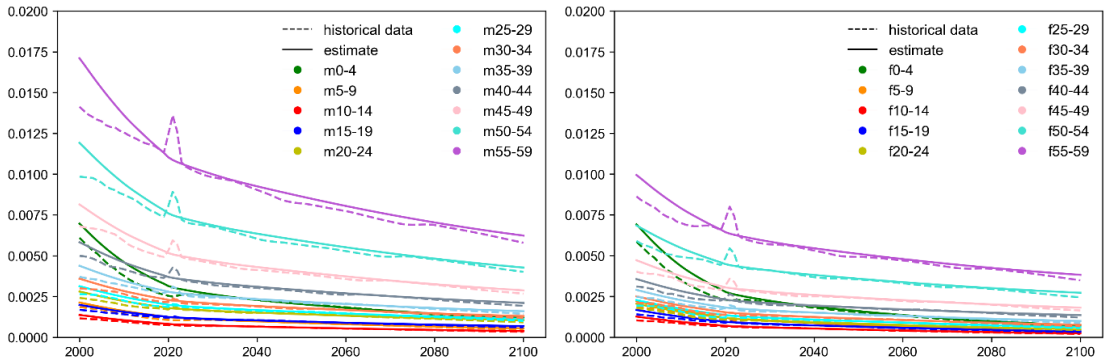

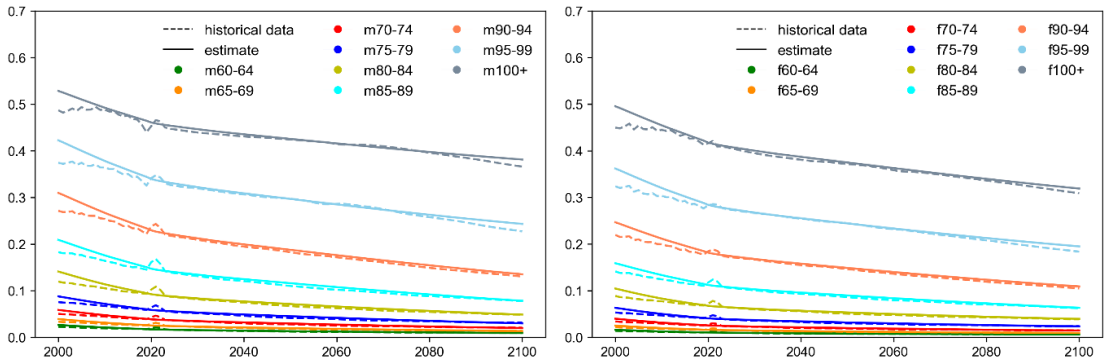

Figure 9: Calibration results of mortality fractions of different age groups excluding climate impacts on mortality. "m" and "f" indicate male and female, respectively. The source of historical data (including projections) is UN Population Prospects (United Nations, 2022).

Table 1: R^2 for the estimated values and historical data of mortality fractions grouped by gender and age (excluding climate impacts on mortality).

Age Cohort	Male	Female
0-4	0.9995	0.9998
5-9	0.9997	0.9996
10-14	0.9998	0.9995
15-19	0.9995	0.9995
20-24	0.9995	0.9998
25-29	0.9996	0.9997
30-34	0.9996	0.9997
35-39	0.9994	0.9995
40-44	0.9993	0.9993
45-49	0.9992	0.9991
50-54	0.9989	0.9987
55-59	0.9977	0.9986
60-64	0.9965	0.9984
65-69	0.9958	0.9987
70-74	0.9949	0.9988
75-79	0.9938	0.9988
80-84	0.9965	0.9989
85-89	0.9916	0.9949
90-94	0.9932	0.9952
95-99	0.9910	0.9934
100+	0.9895	0.9912

Life Expectancy at Birth (LE) is obtained by a multiplicative function of the impacts of *GDP per Capita*, *Mean Years of Schooling*, *Total Food Supply per Capita,* and climate change on a reference value of LE, that is, the observed life expectancy at birth in year 2000 (LE_{2000}) (Equation (2.10)). Each of these functions are assumed to follow a logistic function formulation which yields a flexible function form, e.g. pseudo-linear, depending on parameterization, as stated in Equation (2.11). Similar to the calibration of *Total Fertility* described in Section 2.2, these multiple impacts on life expectancy are calibrated in a step-wise manner. First, the impact of each driver is calibrated, as if it were the sole factor affecting life expectancy, as exemplified in Figure 10. Then, the parameters x_0 are kept constant at their calibrated values, and the other parameters that define the scale and

steepness of the function are varied to calibrate the joint impact of drivers. The resulting functions can be seen in Figure 11.

$$LE(t) = LE_{2000} \times Impact_{le}^{gdp}(t) \times Impact_{le}^{mys}(t) \times Impact_{le}^{food}(t) \times Impact_{le}^{climate}(t) \quad (2.10)$$

$$Impact_{le}^{gdp}(t) = \frac{L_{le}^{gdp}}{1 + e^{-k_{le}^{gdp} \times \left(GWP\ per\ Capita^{*}(t) - x0_{le}^{gdp}\right)}} \quad (2.11)$$

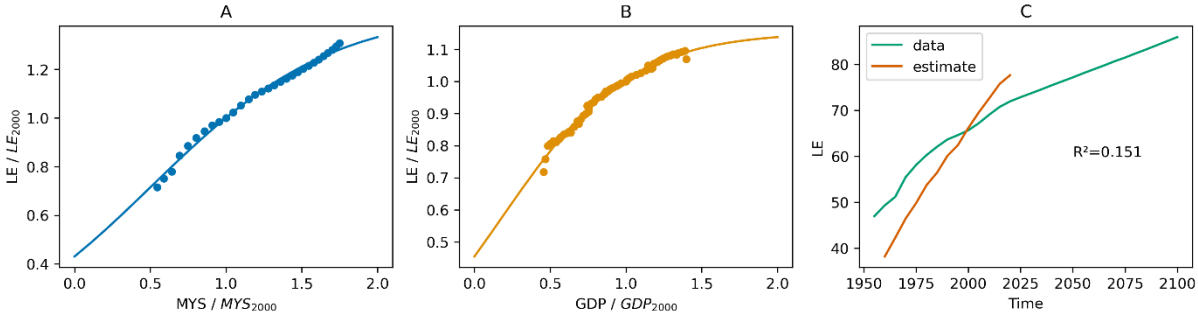

Figure 10: Initial calibration of the drivers of life expectancy at birth. In panels A and B, the dots refer to the historical data obtained from Wittgenstein Center for Data Explored (MYS and Life Expectancy), and from World Bank statistics (GDP per capita). Lines refer to the calibrated function.

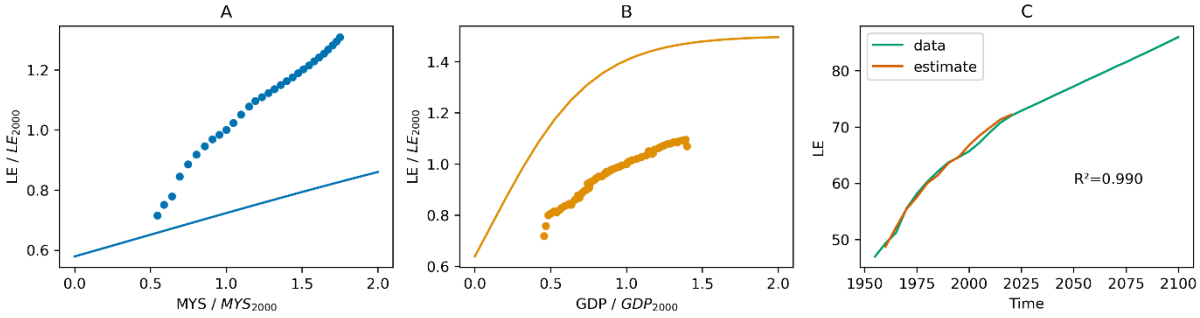

Figure 11: Final calibration of the impacts of education and economic growth on life expectancy at birth.

The impact of food supply on life expectancy ($Impact_{le}^{food}$) is formulated and calibrated similarly, taking the impacts of education and economic growth into account. Figure 12a shows the historical and model-generated relationship between Life Expectancy at Birth and Total Food Supply per Capita in the period 1960-2020, and Figure 12b depicts the multiplier function $Impact_{le}^{food}$ calibrated to this historical data while taking the impacts of education and economic growth into account.

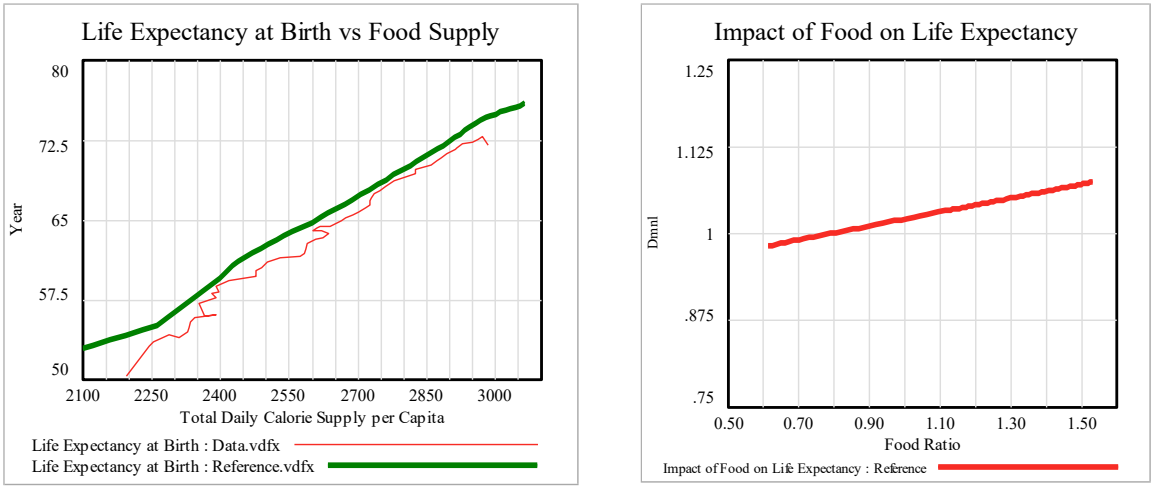

(a) (b)

Figure 12: Impact of food supply on life expectancy. In (a), the red line shows the historical values of global average Life Expectancy at Birth (obtained from Lutz et al., 2018) and Total Daily Caloric Food Supply per Capita (obtained from UN FAO Food Balance Sheets, *FAO, 2025c*). The green line shows the simulation results in the reference scenario. In (b), the impact of food supply on life expectancy, as a multiplier, can be seen, where the x-axis shows the ratio of total daily caloric food supply per capita to the subsistence caloric value, which 2000 kcal per day per person.

The last driver of life expectancy modeled in FeliX is the impact of climate change ($Impact_{le}^{climate}$). Since most of the impact is expected to be observed in future, we did not include it in the calibration to historical data, but we used the temperature-dependent estimates for future projections. Global temperature rise is the main driver of climate mortality, yet those impacts are expected to be mediated by education, therefore we used a formulation that takes both factors into account and calibrated it to the estimates of Bressler et al. (2021) for climate impacts on mortality.

The impact of climate change on life expectancy is inversely proportional to the impact of climate on the mortality fraction ($Impact_{mor}^{climate}$), as shown in Equation 2.12, assuming that global average mortality fraction is equal to $1/LE$. Bressler et al. (2021) estimate the climate impacts on mortality for a 0–4 °C increase in global temperature as compared to 2000–2019 levels. To account for temperature rise beyond this range, we first estimate the impact of temperature change on mortality based on a multivariate regression model, where we control for educational attainment in line with evidence on its role in terms of adaptive capacity (Butz et al., 2014; Lutz et al., 2014). Based on this model, we predict the mortality impact using a range of different values for both temperature change and education. In a next step, and to account for the nonlinearities, we use a logistic function as a proxy for this temperature – mortality impact function (Equation 2.13) and calibrate it to the estimates for the 0–5 °C temperature increase compared to preindustrial times (Figure 13a). This results in the parameter values 7.96, 0.68, 7.76 for y_{mor}, L_{mor}, and $x_{0,mor}$, respectively. In line with the literature and drawing on our regression predictions, we assume that the steepness of this function (k_{mor}) represents the impact of education. As Equation 2.14 shows, we implement two alternative formulations for k_{mor}, depending on *mean years of schooling* (MYS) or the *share of females aged 20-39 with minimum secondary education* (*FE*), respectively. While the former is a widely used summary measure for human capital, the latter was chosen as an alternative indicator that has been shown to be particularly relevant for a variety of socio-economic outcomes including climate risk vulnerability (Striessnig et al., 2013). Keeping the other parameters of $Impact_{mor}^{climate}$ at the values from their previous calibration to the aggregate impact function, we calibrate the steepness parameter, k_{mor}, according to the education-mediated mortality impacts for each discrete value of the independent education variable (MYS or FE). The resulting relationship between steepness and the respective education measure can be seen in Figure 13b and c. In the baseline scenarios, we set the switch for

the impact of education on climate mortality (S_{mor}) equal to 1, meaning that we use the formulation dependent on MYS for the education impacts on climate mortality.

$$Impact_{le}^{climate}(t) = \frac{1}{1 + Impact_{mor}^{climate}(t)} \tag{2.12}$$

$$Impact_{mor}^{climate}(t) = -y_{mor} + \frac{L_{mor}}{1 + e^{-k_{mor}(t) \times \left(T(t) - x_{0,mor}\right)}} \tag{2.13}$$

$$k_{mor}(t) = \begin{cases} 0, & if\ S_{mor} = 0 \\ f_{mor}^{MYS}\left(MYS(t)\right), & if\ S_{mor} = 1 \\ f_{mor}^{FE}\left(FE(t)\right), & if\ S_{mor} = 2 \end{cases} \tag{2.14}$$

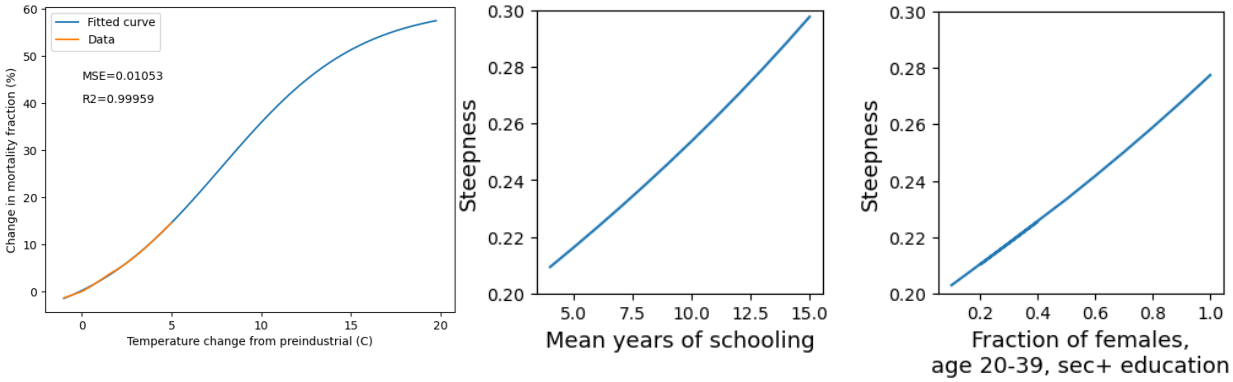

(a) (b) (c)

Figure 13: Calibration results of (a) change in mortality fraction with respect to global mean temperature increase from pre-industrial times, where the data shown in the orange line refer to the empirical estimates (Bressler et al., 2021); (b) the change in the steepness of the climate mortality function with respect to mean years of schooling; (c) the change in the steepness of the climate mortality function with respect to the share of 20-39 year-old females with minimum secondary education.

Finally, *Life expectancy at birth* (*LE*) is converted to *life expectancy* for each age group and gender (LE_{ij}) with constant coefficients (φ_{ij}) as shown in Equation 2.15. The ratio of life expectancy at any age to life expectancy at birth has been almost constant over time between 1990 and 2020 (Figure 14). Therefore, the coefficients φ_{ij} are estimated as the mean of historical values between 1990 and 2020 (Equation 2.16).

$$LE_{ij}(t) = LE(t) \times \varphi_{ij} \tag{2.15}$$

$$\varphi_{ij} = \frac{\sum_{t=1990}^{t=2019} \varphi_{ij}(t)}{30} \tag{2.16}$$

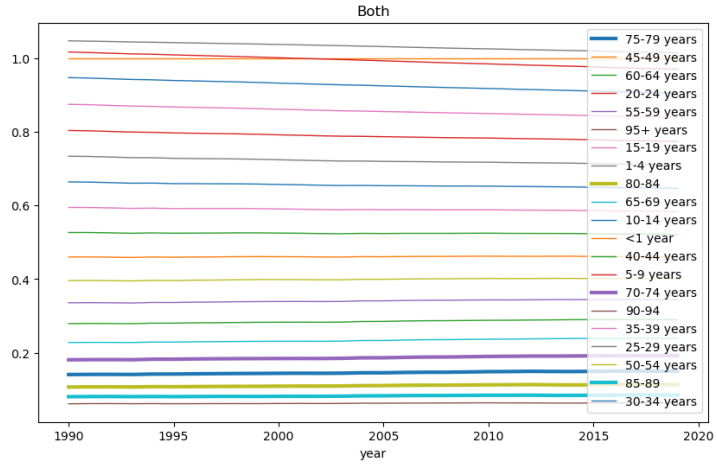

Figure 14: Ratio of life expectancy of each 5-year age group to life expectancy at birth for both genders over time. Data is obtained from the Global Burden of Disease dataset *(A. D. Lopez & Murray, 1998)*.

2.4. Educational attainment and mean years of schooling

The size of different age cohorts feeds into the education module to compute the population of primary, secondary, and tertiary education graduates through the feedback loops among the enrollment rates and graduation rates. The size of the population with each educational attainment level is formulated as another stock chain similar to the population chain shown in Figure 3, to account for the ageing of people who graduate from each level and for transitions between the education levels. Therefore, primary, secondary, and tertiary education graduates are represented by a stock variable for each gender and 5-year age group corresponding to the respective education level.

We make the following assumptions for the correspondence of age groups to education levels:

- Children enroll to primary education when they are 5-9 years old; therefore, the enrollment rate to primary education is a fraction of the population aged 5-9 ($Population_{i,5\text{-}9}$).
- Average duration of primary education is 6 years, as reported by the UNESCO Institute for Statistics for the recent decades. Therefore, children graduate from primary education when they are in the 10-14 or 15-19 age groups.
- A fraction of 10-14 and 15-19 years old primary education graduates enroll into secondary education. Average duration of secondary education is also 6 years, such that people are in the 15-19, 20-24 or 25-29 age groups when they graduate from secondary education.
- Enrollment to tertiary education occurs only in the 15-19, 20-24 and 25-29 age groups, and the average duration of tertiary education is 5 years. Therefore, people join the stock of tertiary education graduates in the age groups 20-24, 25-29 and 30-34.

2.4.1. Primary education

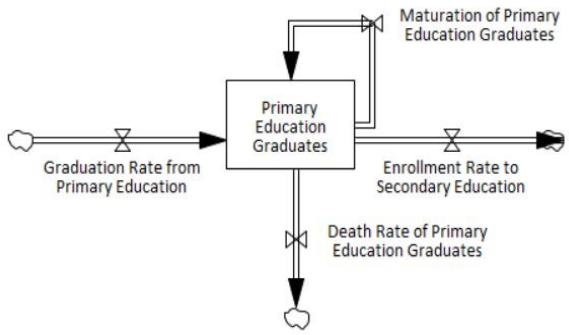

Figure 15: Stock-flow structure of the primary education graduates

The stock-flow structure repeatedly used for all education levels is exemplified in Figure 15, in a compact form of the ageing chain. The net rate of change of the primary education graduates (*PEG*$_{ij}$) for each gender-age group is formulated in Equation 2.17. Maturation ($Maturation_{ij}^{pri}$) and Death ($Death_{ij}^{pri}$) rates of primary education graduates are formulated as fractions of the maturation and death rates for the entire population, where this fraction is the ratio of primary education graduates to the total population, as shown in Equations 2.18 and 2.19.

$$\frac{dPEG_{ij(t)}}{dt} = \begin{cases} 0 \quad ; \quad if\ j\ in\ \{0\text{-}4,5\text{-}9\} \\ Graduation_{ij}^{pri}(t) - Enrollment_{ij}^{sec}(t) - Maturation_{ij}^{pri}(t) - Death_{ij}^{pri}(t) \quad ; \quad if\ j\ in\ \{10\text{-}14,15\text{-}19\} \\ Maturation_{ij-1}^{pri}(t) - Maturation_{ij}^{pri}(t) - Death_{ij}^{pri}(t) \quad ; \quad if\ j > 20\text{-}24 \end{cases} \tag{2.17}$$

$$Maturation_{ij}^{pri}(t) = Maturation_{ij}(t) \times \frac{PEG_{ij}(t)}{Population_{ij}(t)} \tag{2.18}$$

$$Death_{ij}^{pri}(t) = Death_{ij}(t) \times \frac{PEG_{ij}(t)}{Population_{ij}(t)} \tag{2.19}$$

The graduation rate from primary education ($Graduation_{ij}^{pri}$) is equal to enrollment rate to primary education ($Enrollment_{i}^{pri}$), yet after a delay (d_{pri}) equal to the average duration of primary education. *DELAY1* is a function that represents first order exponential delay. Following enrollment within the age group 5-9, we assume that 80% of the children graduate when they are 10-14 years old, and 20% graduate when they are 15-19 years old.

$$Graduation_{ij}^{pri}(t) = \begin{cases} DELAY1\left(Enrollment_{i}^{pri}(t), d_{pri}\right) \times \frac{4}{5} \quad ; \quad if\ j = 10\text{-}14 \\ DELAY1\left(Enrollment_{i}^{pri}(t), d_{pri}\right) \times \frac{1}{5} \quad ; \quad if\ j = 15\text{-}19 \end{cases} \tag{2.20}$$

The enrollment rate is a fraction of the population aged 5-9. The primary education enrollment fraction (*PEF*) for each gender is defined as a reference value (PEF_i^*) multiplied by the impact of GDP ($Impact_{i,pri}^{gdp}$). PEF_i^* corresponds to the maximum possible enrollment fraction. According to the formulation in Equation 2.23 the impact of GDP is assumed to be a logistic (S-shaped) function that saturates at 1, where the parameters P_2 and P_0 refer to the steepness and inflection point, respectively, and where $GWP\ per\ Capita^*$ is the ratio of gross world product per capita to its value in 2000.

$$Enrollment_{i}^{pri}(t) = Population_{i,5-9}(t) \times PEF_i(t) \tag{2.21}$$

$$PEF_i(t) = PEF_i^* \times Impact_{i,pri}^{gdp}(t) \tag{2.22}$$

$$Impact_{i,pri}^{gdp}(t) = \frac{1}{1 + e^{-P_{2,i} \times (GWP\ per\ Capita^*(t) - P_{1,i})}} \tag{2.23}$$

The formulation of secondary and tertiary education graduates follows Equations 2.17–2.23, with differences in the age groups explained in the list of assumptions above. Enrollment to secondary (tertiary) education is assumed to be fraction of the primary (secondary) education graduates, implying that the previous education level is a prerequisite for enrollment. The effect of GWP on enrollment for each education level is calibrated to historical data from Wittgenstein Center Human Capital Data Explorer for the period 1950-2020, and the updated SSP2 projections for the rest of the century. Figure 16a shows the calibration results for the impact of GDP on primary, secondary and tertiary education enrollment. The effect of GDP on secondary education enrollment is much steeper than the effect on tertiary education, yet the effect on primary education is much flatter, resonating with the historical observations that primary education enrollment is triggered mostly by regulation rather than income. Figure 16b-d show the model-generated dynamic behavior in the reference simulation and the historical data for the three education levels. The difference between model behavior and observed data can be attributed to the limitations of the model structure described above, such as the persistence rates at primary and secondary education persistence of pupils to graduate after enrollment) that are excluded from the model, and our set assumptions about the enrollment ages. It is important to note that Figure 16 visualizes the model output in a business-as-usual (BAU) scenario aligned with SSP2 narrative. The other two baseline scenarios, corresponding to SSP1 and SSP3, used for analyzing the future wellbeing dynamics (Section 13) deviate from this BAU scenario and thus imply different model-generated educational attainment dynamics.

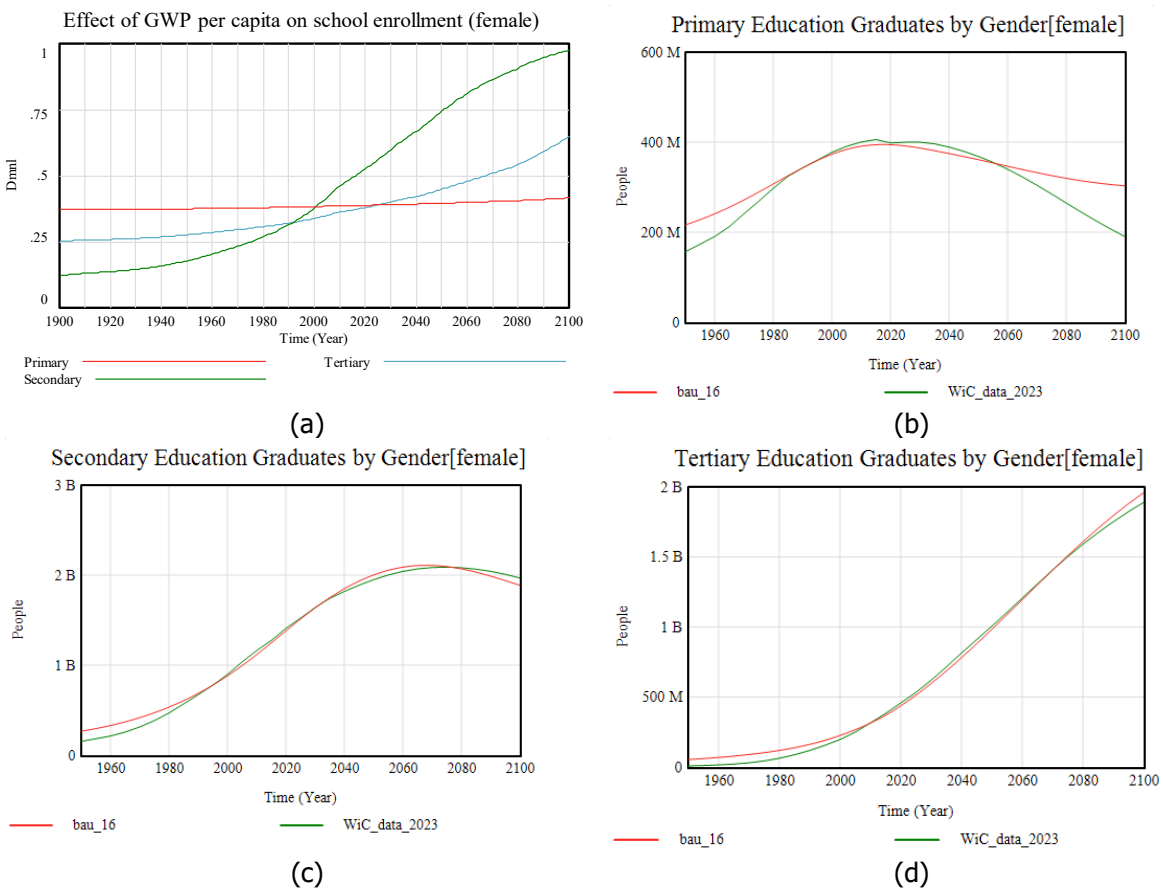

Figure 16: Calibration of the education module for females: (a) Impact of GDP per capita on enrolment to each education level, (b-d) Primary, secondary, and tertiary education graduates over time in the BAU simulation (bau_16) and the historical data obtained from the Wittgenstein Center, including the updated SSP2 projections for the post 2020 period (WiC_data_2023).

2.4.2. Mean years of schooling

Mean years of schooling (MYS) is the indicator used in defining the effect of education on fertility rates and life expectancy. We formulate MYS as the weighted average of the duration of each education level, where the weights are determined by the total number of graduates for the respective education level relative to the population aged 15 and above. Note that this formulation does not include schooling that results in drop-out. Equation 2.24 denotes this formulation, where *SEG* and *TEG* refer to secondary and tertiary education graduates, respectively.

$$MYS(t) = \frac{d_{pri} \times \sum_{j\geq 15} PEG_j(t) \; + \; (d_{pri} + d_{sec}) \times \sum_{j\geq 15} SEG_j(t) \; + \; (d_{pri} + d_{sec} + d_{ter}) \times \sum_{j\geq 15} TEG_j(t)}{\sum_{j\geq 15} Population_j(t)} \qquad (2.24)$$

MYS would be overestimated with the current average durations reported by UN IES, yet there is no data available for the historical average duration of education at each level. Therefore, we assume that the average primary education duration was 2 years in the year 1900 and subsequently increased at an increasing rate to 6 years. Similarly, secondary and tertiary education duration is assumed to start from 1 and 2 years, respectively, in 1900, and subsequently to increase to the current duration of 6 and 5 years, respectively. Figure 17 shows the model behavior resulting from this formulation in comparison to the historical data and SSP2 projections.

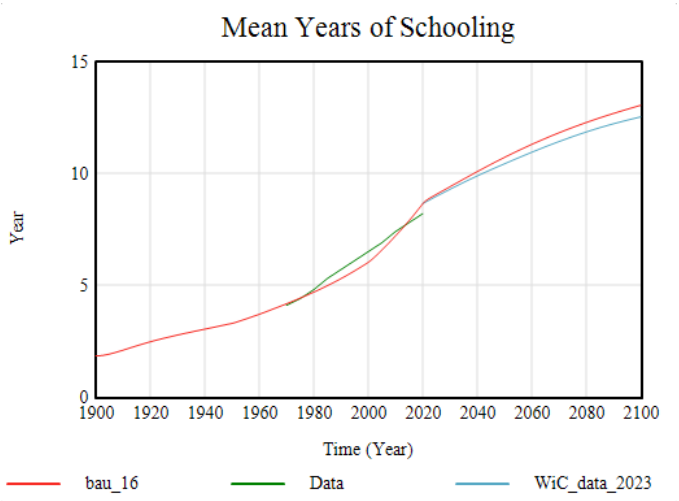

Figure 17: Mean Years of Schooling in the reference simulation results (BAU, red line) and historical data (Data, green line). Data is obtained from the Wittgenstein Centre Human Capital Data Explorer (Lutz et al., 2018) and includes the SSP2 projections updated in 2023 (blue line).

2.5. Labor force

We assume that the size of the skilled labor force is the sum of the total population aged 15-64 with tertiary education, and half of the population aged 15–64 with secondary education (Equation 2.25, j=15-64). The size of the unskilled labor force is determined by the remaining population aged 15–64 (Equation 2.26). The labor force input in the calculation of the economic output is the corresponding labor force multiplied by the labor force participation rates for the respective groups (Equations 2.27 and 2.28).

$$LF_{i,j}^{skilled}(t) = Tertiaty\ education\ graduates_{i,j}(t) + 0.5 \times Secondary\ education\ graduates_{i,j}(t) \qquad (2.25)$$

$$LF_{i,j}^{unskilled}(t) = NonEducated_{i,j}(t) + Primary\ education\ graduates_{i,j}(t) + 0.5 \times Secondary\ education\ graduates_{i,j}(t) \qquad (2.26)$$

$$LFinput_{i,j}^{skilled}(t) = \frac{LF_{i,j}^{skilled}(t)}{Initial\ LF_{i,j}^{skilled}} \times LF\ participation\ rate_{i,j}(t) \quad (2.27)$$

$$LFinput_{i,j}^{unskilled}(t) = \frac{LF_{i,j}^{unskilled}(t)}{Initial\ LF_{i,j}^{unskilled}} \times LF\ participation\ rate_{i,j}(t) \quad (2.28)$$

3. Economy

3.1. GDP

Gross world production (GWP) is calculated by total reference economic output (REO), adjusted for the impact of climate change $IF_{\substack{climate \\ on\ GWP}}$ and biodiversity $IF_{\substack{biodiversity \\ on\ GWP}}$ (Equation (3.1)). The total REO is the sum of the REO generated by the skilled and unskilled labor force and determined according to a Cobb-Douglas production function (Equations 3.1-3.4) (Hughes, 2015; Zellner et al., 1966), depending on technology and capital allocated to the skilled/unskilled labor force and the size of this labor force input $LFinput_{i,j}^{\frac{skilled}{unskilled}}$. In FeliX, technological progress is assumed to relate to the energy technology and all other technology (Equation 3.5), where the energy technology is endogenously determined by investments in the energy module and all other technology follows an exogenous trend. Capital is determined by capital investments in the energy and all other sectors, which are also captured within the energy module and as an exogenous trend, respectively (Equations 3.6-3.7). The shares of technology and capital, $Ratio\ of\ technology_{skilled}$, $Ratio\ of\ capital_{skilled}$, , attributed to the skilled and unskilled, sectors, respectively, and the capital elasticity of output for the two sectors, $c_{skilled}$, $c_{unskilled}$, respectively, are assumed to be exogenous parameters and determined by the model calibration based on historical data of GWP and GWP per capita from the World Bank (The World Bank, 2023).

$$GWP(t) = REO(t) \times IF_{\substack{climate \\ on\ GWP}}(t) \times IF_{\substack{biodiversity \\ on\ GWP}}(t) \quad (3.1)$$

$$REO(t) = REO_{skilled}(t) + REO_{unskilled}(t) \quad (3.2)$$

$$REO_{skilled}(t) = REO_{initial} \times Output_{1900} \times Ratio\ of\ technology_{skilled}(t) \times Technology(t) \times \left(Ratio\ of\ capital_{skilled}(t) \times \frac{Capital(t)}{Capital_{inital}}\right)^{c_{skilled}} \times \sum_{i,j=15-64} LFinput_{i,j}^{skilled\ (1-c_{skilled})}(t) \quad (3.3)$$

$$REO_{unskilled}(t) = REO_{initial} \times Output_{1900} \times \left(1 - Ratio\ of\ technology_{skilled}(t)\right) \times Technology(t) \times \left(\left(1 - Ratio\ of\ capital_{skilled}(t)\right) \times \frac{Capital(t)}{Capital_{inital}}\right)^{c_{unskilled}} \times \sum_{i,j=15-64} LFinput_{i,j}^{unskilled\ (1-c_{unskilled})}(t) \quad (3.4)$$

$$Technology(t) = Energy\ Technology(t) + Other\ Technology(t) \quad (3.5)$$

$$\frac{dCapital(t)}{dt} = Capital\ investment(t) \quad (3.6)$$

$$Capital\ investment(t) = Capital\ investment_{energy}(t) + Capital\ investment_{other}(t) \quad (3.7)$$

3.2. Climate impacts

The earlier versions of the FeliX model included climate damages on GDP based on early estimates as used in the DICE model (W. Nordhaus, 2007). In the last ten years, the estimation of the aggregate economic impact of climate change has been updated substantially based on new empirical data and methods, resulting in larger damage estimates. In many economic modelling studies (Dietz & Stern, 2015; Kalkuhl & Wenz, 2020; W. D. Nordhaus, 2017; Weitzman, 2012), climate damage is formulated as a fraction of GDP, with a quadratic function that yields additional damages at an increasing rate for a rising global mean temperature anomaly. In an extensive and widely accepted empirical analysis, Burke et al. (2015) estimate the aggregate climate damage based on micro impacts such as the daily temperature effect on labor productivity per person, agricultural productivity and adaptation efforts across different countries. Burke et al. estimate damage at much larger values compared to the earlier literature, even for relatively modest temperatures. In Figure 18, the black line shows the average damage estimate of Burke et al. when rich and poor countries are assumed to respond identically to the temperature change (pooled response), and the annual GDP is assumed to be affected by temperature changes in a 1 year duration (short-run effect). When the countries are assumed to give a differentiated response and long-run (5 year) effects of temperature change are considered, the damage becomes much higher, reaching the upper end of the gray shaded area in Figure 18, reaching almost 80% of loss at 5°C of warming.

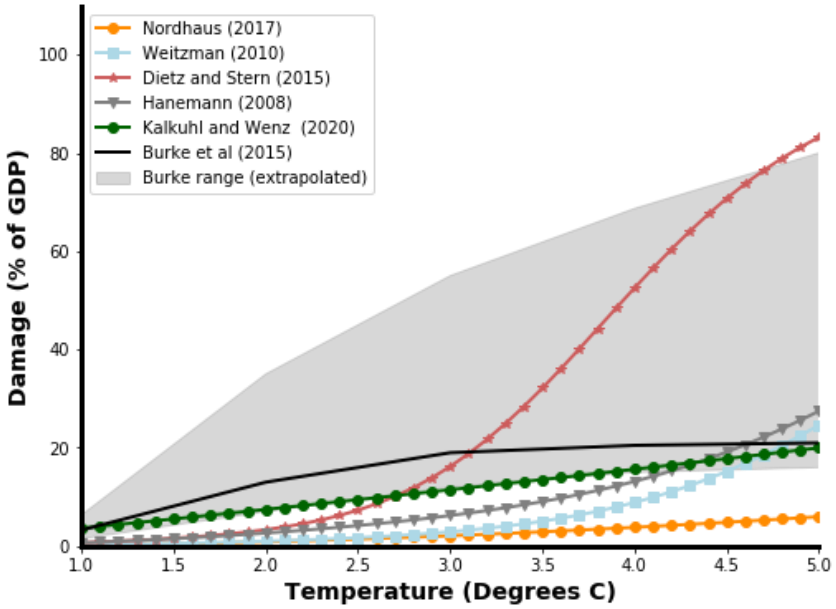

Figure 18: Damage functions and estimates commonly used in the literature

In FeliX, climate damage is formulated as a fraction of global GDP, that is, Gross World Product (GWP). We have an optional structure that enables using the damage functions obtained from the abovementioned studies, or a custom function defined in a flexible logistic form. Equation 3.9 shows this optional formulation, where *Climate Damage Function Switch* (s_{damage}) is the user-defined parameter that enables switching between the options.

$$IF_{\substack{climate \\ on\ GWP}}(t) = 1 - D(t) \tag{3.8}$$

$$D(t) = \begin{cases} 0, if\ s_{damage} = 0 \\ D_N(t), if\ s_{damage} = 1 \\ D_{DS}(t), if\ s_{damage} = 2 \\ D_{B1}(t), if\ s_{damage} = 3 \\ D_{B2}(t), if\ s_{damage} = 4 \\ D_L(t), if\ s_{damage} = 5 \end{cases} \quad (3.9)$$

$D_N(t)$ in Equation 3.10 is the damage function used by W. D. Nordhaus (2017), where T is the global mean temperature change from preindustrial times and the parameters α and β are -0.00118 and 0.00278, respectively yielding the percentage damage. Equation 3.11 shows the function used by Dietz & Stern (2015), where the parameters δ_1, $\delta_2, \epsilon_1, \varepsilon_2$ are 12.2, 4, 2 and 7.02, respectively. $D_{B1}(t)\ and\ D_{B2}(t)$ refer to the short-term pooled and long-term differentiated damage estimates of Burke et al. (2015), and they are defined in a lookup form digitalized from the figures in their paper. Table 2 lists those point estimates used in the model.

$$D_N(t) = 1 - \frac{1}{1 + \alpha T(t) + \beta T(t)^2} \quad (3.10)$$

$$D_{DS}(t) = 1 - \frac{1}{1 + \left(\frac{T(t)}{\delta_1}\right)^{\epsilon_1} + \left(\frac{T(t)}{\delta_2}\right)^{\varepsilon_2}} \quad (3.11)$$

Table 2: Damage estimates of Burke et al. (2015) for short-term pooled (D_{B1}) and long-term differentiated (D_{B2}) responses

T (°C)	D_{B1}(%)	D_{B2}(%)
1	1	6.3
2	13	35
3	19	55
4	20.5	68.7
5	21	80

$D_L(t)$ is the logistic function shown in Equation 3.12 that can be used to define custom-shaped damage functions using the three parameters that represent the saturation level (L_{damage}), steepness (k_{damage}) and the inflection point ($x0_{damage}$). The values of these parameters that yield the abovementioned four damage functions can be seen in Table 3.

$$D_L(t) = \frac{L_{damage}}{1 + e^{-k_{damage}(T(t) - x0_{damage})}} \quad (3.12)$$

Table 3: The parameter values of the logistic function calibrated to the four damage functions obtained from the literature

	D_N	D_{DS}	D_{B1}	D_{B2}
L_{damage}	0.073953	0.935478	0.206988	0.75716
k_{damage}	1.09955	1.795846	1.888017	1.43089
$x0_{damage}$	3.89219	3.863367	1.773525	2.2569

3.3. Poverty

The poverty module captures the dynamic relationships between the poverty rate of the global population and relevant drivers from the economy, population, education, as well as the impacts from energy, and land-use modules (Figure 19).

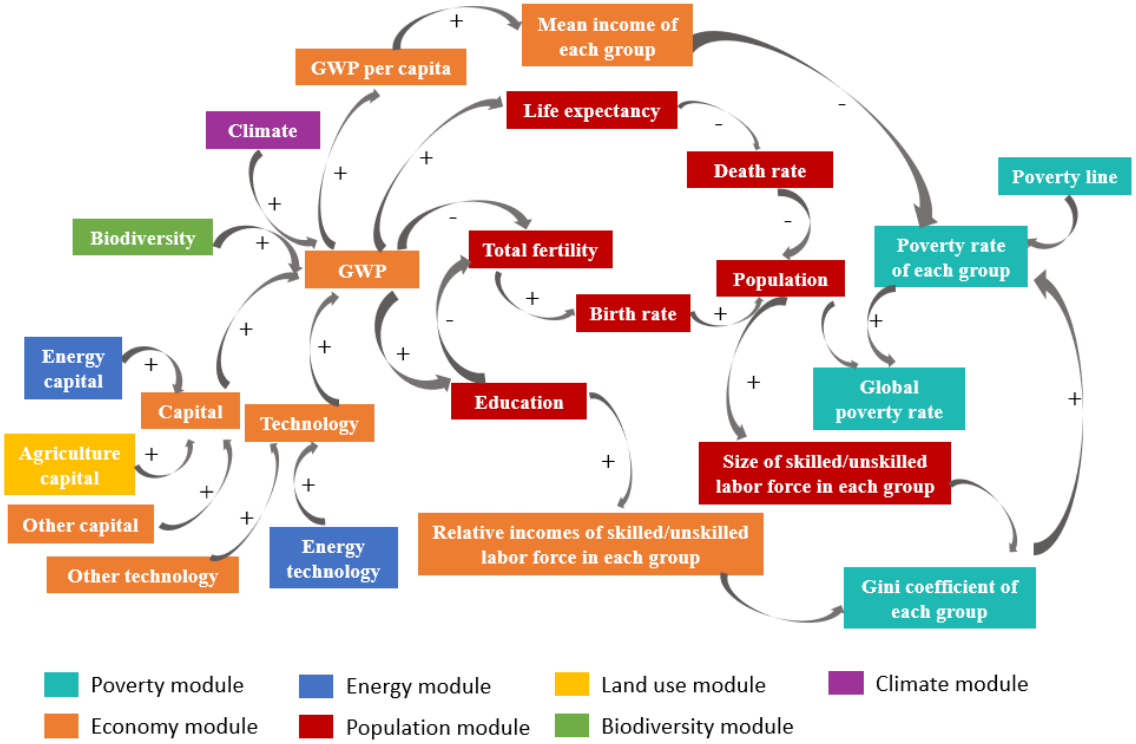

Figure 19: Conceptual relationships between the poverty module and other modules. Each text box indicates a variable, and the background color of the text box indicates the module from which the variable proceeds. Each arrow represents a causal relationship between two variables. The +/- sign on an arrow indicates a positive/negative relationship. The poverty rate of each population group is determined by the poverty line, mean income and Gini coefficient of each group. The Gini coefficient is related to the sizes and relative incomes (incomes share) of skilled and unskilled labor forces.

The global poverty rate *PR* is calculated as the sum of the poverty rates across the different population groups aged over 15 weighted by their corresponding population shares (Equation 3.13).

$$PR(t) = \frac{\sum_{i=male,female} \sum_{j=15-19}^{100+} PR_{i,j}(t) \times Population_{i,j}(t)}{\sum_{i=male,female} \sum_{j=0-4}^{100+} Population_{i,j}(t)} \quad (3.13)$$

The poverty rate $PR_{i,j}$ of each population group is defined as the share of the population living below a specified poverty level *PL* (Fosu, 2010; Hughes, 2015) (Figure 20). In the calculation of $PR_{i,j}$, income is assumed to follow a log-normal distribution, which has been widely used in the assessment of global and regional inequality and poverty (Crespo Cuaresma et al., 2018; Hughes, 2015; Lakner et al., 2022; Soergel et al., 2021) and has been verified by statistical analyses for various data sets (Kemp-Benedict, 2001; Kot, 2016; J. H. Lopez & Luis, 2006). Therefore, $PR_{i,j}$ is formulated as:

$$PR_{i,j}(t)(x \leq PL) = \emptyset\left(\frac{\ln(PL) - \mu_{i,j}(t)}{\sigma_{i,j}(t)}\right) \quad (3.14)$$

where *x* is the income per capita of each group, where *PL* is set to the international extreme poverty line ($2.15 per capita per day in 2017 purchasing power parity), and where μ and σ are the mean and the standard deviation of the normal distribution function of *ln(x)*, respectively.

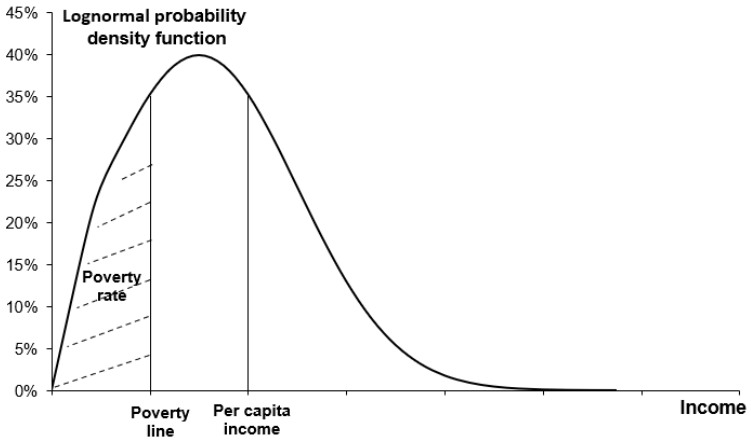

Figure 20: The lognormal probability density function of income. The shaded area is equal to the poverty rate.

The standard normal cumulative distribution function $\emptyset(X)$ is formulated by Equation 3.15, the value of which can be obtained by looking up the standard normal distribution table. The probability density function of income is shown by Equation 3.16 (Figure 20) (Mendez Ramos, 2019). Let μ and σ denote the mean value and the standard deviation of the normal distribution function $N(\mu, \sigma)$. Then $X = \frac{\ln(PL)-\mu_{i,j}(t)}{\sigma_{i,j}(t)}$ conforms to the standard normal distribution.

$$\emptyset\left(\frac{\ln(x)-\mu_{i,j}(t)}{\sigma_{i,j}(t)}\right) = \int_{-\infty}^{\frac{\ln(x)-\mu_{i,j}(t)}{\sigma_{i,j}(t)}} \frac{1}{\sqrt{2\pi}} e^{-\frac{\left(\ln(x)-\mu_{i,j}(t)\right)^2}{2\sigma_{i,j}^2(t)}} dx \tag{3.15}$$

$$f(x,\mu,\sigma,t) = \frac{1}{\sqrt{2\pi}\sigma_{i,j}(t)} e^{-\frac{\left(\ln(x)-\mu_{i,j}(t)\right)^2}{2\sigma_{i,j}^2(t)}}, \ln(x) \sim N(\mu,\sigma) \tag{3.16}$$

To get the poverty rate $PR_{i,j}$ of each group, given the poverty line, only $\mu_{i,j}$ and $\sigma_{i,j}$ need to be computed. Equations 3.17 and 3.18 formulate the relationship between income per capita, $\mu_{i,j}$, and $\sigma_{i,j}$ of each group (Chotikapanich et al., 1997; Dixon et al., 1987). $\sigma_{i,j}$ can be expressed as a function of the Gini coefficient, whereas $\mu_{i,j}$ is a function of $\sigma_{i,j}$ and the income per capita of the population (Dixon et al., 1987). $\emptyset^{-1}(\cdot)$ is the inverse standard normal cumulative distribution function, the value of which can be obtained through the inverse query of the standard normal distribution. To calculate $\mu_{i,j}$ and $\sigma_{i,j}$, we thus need to calculate the Gini coefficient and income per capita.

$$e^{\mu_{i,j}(t)+\frac{\sigma_{i,j}^2(t)}{2}} = Income\ per\ capita_{i,j}(t) \tag{3.17}$$

$$\sigma_{i,j}(t) = \sqrt{2}\emptyset^{-1}\left(\frac{Gini_{i,j}(t)+1}{2}\right) \tag{3.18}$$

The Gini coefficient is a numerical value derived from the Lorenz curve[38] Figure 21as a graphical measure of the income distribution (Figure 21). Let *A* denote the area between the perfect equality line and the Lorenz curve, and *B* the area beneath the Lorenz curve (Figure 21). The Gini coefficient for each population group can thus be defined by Equation (3.19) (Dixon et al., 1987). Following the International Futures model (Hughes, 2015),

we divide the labor force of each group into unskilled and skilled. *B* can thus be expressed as the sum of B_1 and B_2, which represent the areas beneath the Lorenz curve for the unskilled and skilled labor force, respectively (Figure 21).

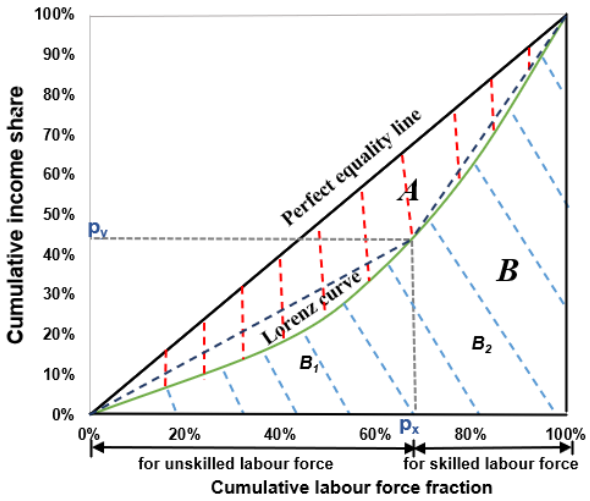

Figure 21: Income distribution measured by Lorenz curve. The cumulative labor force fraction at a point on the x-axis is defined as the size of cumulative labor force at this point divided by the size of the total labor force. The x-value of px and a y-value of py mean that the unskilled labor force (the bottom px of the labor force) controls the proportion py of the total income. The Gini coefficient is a numerical value derived from the Lorenz curve to measure income distribution, which is defined as *A/(A+B)*. Here, *A* and *B* represent the sizes of the red and blue striped areas. *B* is the sum of B_1 and B_2. The sum of *A* and *B* is 0.5. The perfect equality line corresponds to a Gini coefficient of 0, indicating that every person has the same income.

By using a triangle and a trapezoid to approximate the areas of B_1 and B_2[19], the Gini coefficient can be reformulated by Equation 3.20. $Relative\ income_{i,j}^{Total}$, $Relative\ income_{i,j}^{unskilled}$ and $Relative\ income_{i,j}^{skilled}$ denote the relative income share of the total, unskilled, and skilled labor force of the corresponding population group, respectively. $Population_{i,j}^{unskilled}$ and $Population_{i,j}^{skilled}$ denote the population size of the total, unskilled, and skilled labor force of the corresponding population group, respectively.

$$Gini_{i,j}(t) = \frac{A_{i,j}(t)}{A_{i,j}(t) + B_{i,j}(t)} = \frac{0.5 - B_{i,j}(t)}{0.5} = 1 - 2B_{i,j}(t) \tag{3.19}$$

$$Gini_{i,j}(t) = 1 - \frac{1}{Relative\ income_{i,j}^{Total} \times Population_{i,j}(t)} \times \left(\begin{array}{c} Population_{i,j}^{unskilled}(t) Relative\ income_{i,j}^{unskilled} \\ + Population_{i,j}^{skilled}(t)\left(2Relative\ income_{i,j}^{unskilled} + Relative\ income_{i,j}^{skilled}\right) \end{array} \right) \tag{3.20}$$

The value of $Relative\ income_{i,j}^{Total}$ is assumed to be 100. The values of $Relative\ income_{i,j}^{unskilled}$ and $Relative\ income_{i,j}^{skilled}$ are based on relative earnings data for OECD countries (Equations 3.21 and 3.22). The value 65 approximates the average relative earnings share of the skilled population in OECD countries. The $Adjustment\ parameter\ for\ relative\ incomes\ of\ skilled_{i,j}$ for each group adjust the relative incomes of skilled labor force in line with the model calibration.

$$Relative\ income_{i,j}^{skilled} = 65 \times Adjustment\ parameter\ for\ relative\ incomes\ of\ skilled_{i,j} \tag{3.21}$$

$$Relative\ income_{i,j}^{unskilled} = Relative\ income_{i,j}^{Total} - Relative\ income_{i,j}^{skilled} \quad (3.22)$$

$Income\ per\ capita_{i,j}$ is formulated by Equation 3.23, where $Real\ earnings\ parameter_{i,j}$ is determined by model calibration.

$$Income\ per\ capita_{i,j}(t) = GWP\ per\ capita(t) \times Real\ earnings\ parameter_{i,j} \quad (3.23)$$

In the model calibration, values of $Adjustment\ parameter\ for\ relative\ incomes\ of\ skilled_{i,j}$ and $Real\ earnings\ parameter_{i,j}$ are determined based on three assumptions: (1) the relationship between income and age tends to exhibit an inverted-U-shape pattern. Income rises with age and then drops slightly as individuals enter retirement (Mincer, 1989; Skirbekk, 2004). (2) Males have more income than females in the same age group (Bar-Haim et al., 2023; Polachek, 2003). (3) The relative income share of the skilled population in each group is larger than that of unskilled population. In addition, due to the limited availability of relevant historical data and in order to make the calibration process more reliable, the population age groups are divided into three wider age groups: childhood (0-14 years old), working age (15-64) and old age (65+). Parameters are then distinguished only across these three age groups.

The model calibration results for global poverty rates are shown in Figure 22.

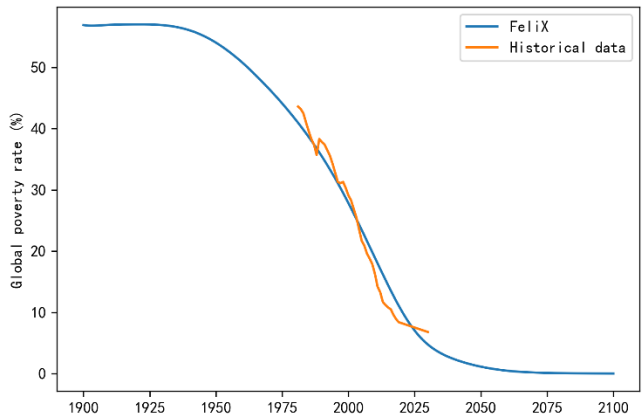

Figure 22: Business-as-usual simulation results for global poverty rates. Source of the historical data: https://data.worldbank.org/indicator/SI.POV.DDAY

4. Energy

In line with the real-life developments when it was built, FeliX model focuses on 6 key energy sources: coal, oil and gas on the fossil fuels side; solar, wind and bioenergy on the renewables side. The model captures the investment cycles, technology and capacity development, and eventual production of energy from these sources to meet the global primary energy demand. The market share of these six sources is determined by the relative price and the production volumes adjust to the corresponding primary demand for each source, while the total energy demand is driven by population and energy demand per capita, which in turn is determined by wealth of the population, captured by gross world product.

Regarding the technology and capacity development, the model takes the chain of upstream activities such as exploration, development and extraction into account for fossil fuel production. The model assumes that all existing (identified) reserves have been proven, hence ready for energy production, with capital investments made to establish production capacities. However, only a fraction of the fossil fuel reserves is recoverable with a

given technology. Therefore, the model also takes investment into technology development into account. Eventually, production volumes are on one hand determined by production capacity and on the other by price-based market share of a given source of energy.

For the renewables, the model also includes the investments and development of capacity and technology, with learning effects on installation and production costs. The difference from the fossil fuels is expectedly the absence of resource constraints on production, yet the available capacity and capacity factors are considered as the main drivers of energy generation from the renewables.

Capital investments in production capacity for all different kinds of energy contribute to global capital stock increase. Energy technology development contributes to global technology increase. Both processes influence Gross World Product.

4.1. Energy Demand

The structure of the FeliX model depicts the causality between the wealth of the society and the energy demand, similar to the Kaya identity, yet it does not distinguish between different end use sectors. Energy Demand per Capita is an average value and currently does not distinguish between population subgroups by age and gender. *Energy Demand per Capita* multiplied by *Population* constitutes the *Total Energy Demand*.

Energy Demand per Capita is formulated as a ratio of the (global average) *Maximum Energy Demand per Capita*, which is assumed to be 56,100 kWh/person/year (4.8e-06 Mtoe/person/year), noting that the global average primary energy demand per capita was 21,654 kWh in 2024 (Energy Institute, 2024). The ratio, which is the *Impact of GDP on Energy Demand* is a nonlinear function of *GDP per Capita*, and it is calibrated to the historical data of total primary energy demand between 1965 and 2020 obtained from the Energy Institute Statistical Review (formerly BP Energy Statistics).

The Energy Demand compared to Energy Production (sum of production from all considered in the model energy sources) constitutes Energy Demand Fulfillment Ratio which is an indicator of how well the investment in energy and production efficiency is able to secure the demand of the energy users.

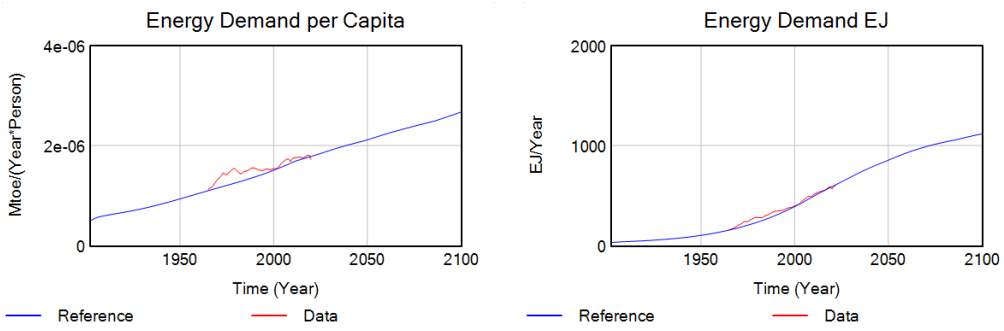

Figure 23: Energy Demand per Capita and Total Energy Demand in the Reference simulation compared to the historical dynamics (Data source: Energy Institute, 2024)

4.2. Market Shares

The *Total Energy Demand* is split up between different energy sources according to the market share of each energy source. The market share depends on the price and its competitive price elasticity. The FeliX model sector mimics the dynamics of energy market shares in two steps.

In the first step the price of each specific energy source is averaged over a period of time. The *Average Energy Price* is calculated as arithmetic mean of all averaged energy prices. Price competitive factor is calculated for all energy sources as a comparison of the averaged energy source price and *Average Energy Price*.

In the second step the Price Competitive Factor for each energy source is adjusted by elasticity of that energy source price to demand. Based on the competitiveness and elasticity the market share of a specific energy source is adjusted. In case of biomass the market share is additionally separated into forest and crops related resources.

This simple market share representation is based only on relative market prices assuming full possible substitutability among the primary energy sources and does not capture path-dependency and infrastructure lock-ins. Therefore, the discrepancies between the model output and historical data (primary energy consumption by source obtained by Energy Institute, 2024) can be explained by this modeling choice on the simple price-based representation.

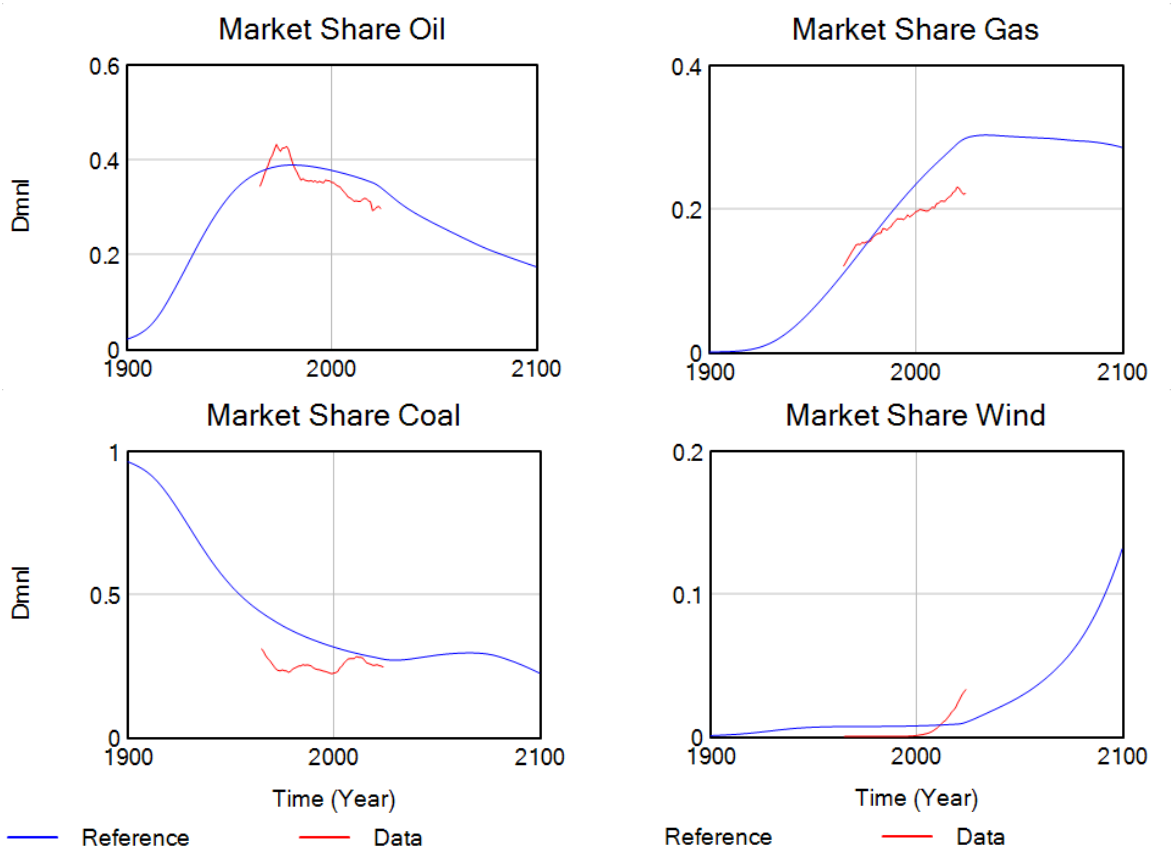

Figure 24: Share of oil, natural gas, coal and wind in the primary energy consumption in the Reference simulation compared to the historical dynamics (Data source: Energy Institute, 2024)

4.3. Fossil Fuels

The model structure representing the fossil fuels (coal, oil, natural gas) captures the natural gas extraction and upstream market dynamics. It is adapted from Davidsen et al. (1990) and Eker (2016). Figure 25 provides and overview of this model structure used for all three fossil fuel sources, with the stock-chain of undiscovered resources, identified reserves and cumulative production (Note that this categorization of natural resources is more detailed with intermediary steps in some industry sources).

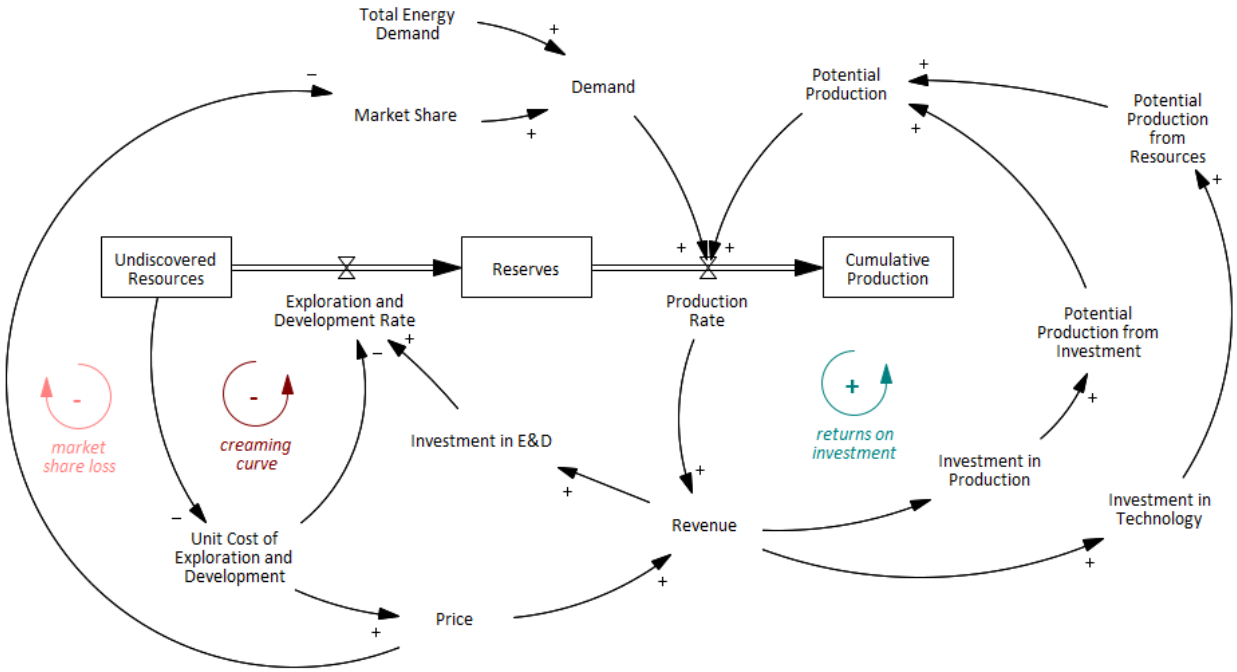

Figure 25: Overview of the model structure for fossil fuel extraction and market

Exploration activities deplete the *Undiscovered Oil Resources* and after infrastructure development, add them to the stock of *Identified Reserves*, which is depleted by *Production Rate*. Potential *Exploration and Development (E&D) Rate* is formulated as the investments divided by the unit cost of E&D, and takes also the desired value of exploration by the industry to keep the reserves at a certain coverage level of demand (years in future). Unit costs of exploration and development increase as the undiscovered resources decline, representing the phenomena known as *creaming curve* in the industry.

Similarly, *Production Rate* is the minimum of demand for this particular energy source and its potential production. The demand represents price-dependent fraction (Market Share) of total Energy Demand. Potential production considers both the recoverable reserve availability (economically profitable to produce) and investments in production, which determine the potential production volume based on its unit cost. Investments are formulated as a fraction of the revenue, hence forming a positive feedback loop through eventual production, and a negative feedback loop through the unit costs (more production results in higher unit costs of exploration and development, hence price, through the upstream).

Figure 26 shows the annual production volume of three fossil fuel energy sources resulting from the model structure described above, and as obtained from the historical statistics.

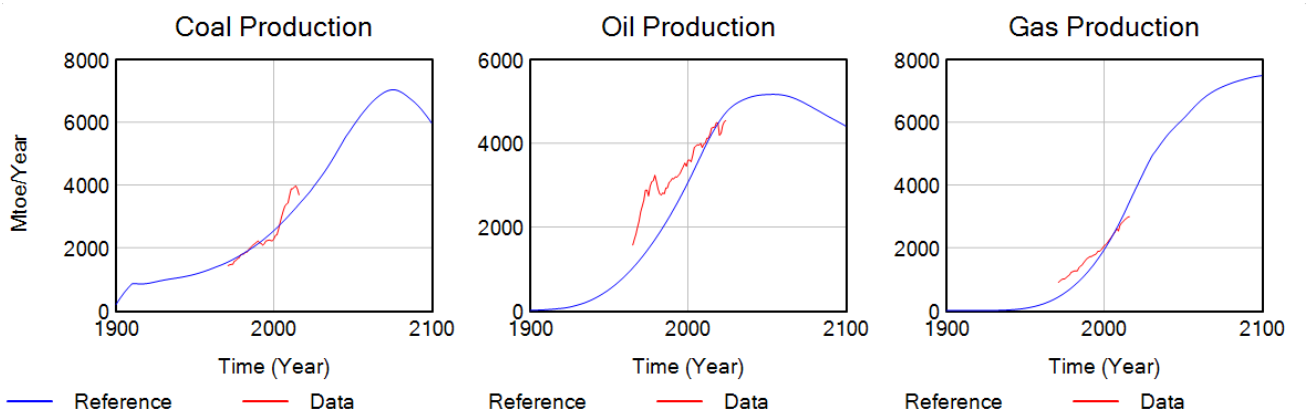

Figure 26: Production of coal, oil, and natural gas in the Reference simulation compared to the historical dynamics (Data source: Energy Institute, 2024); the R^2 values between the model and data are 0.928, 0.912, and 0.993 for coal, oil and gas, respectively.

4.4. Renewable Energy

The basic model structure for all renewable energy model sectors – solar, wind and biomass – is very similar and differs only due to specifics of the energy source, for instance related to weather. Figure 27 depict the overview of this representation with the main relations and feedback loops between costs, capacity installation and investments.

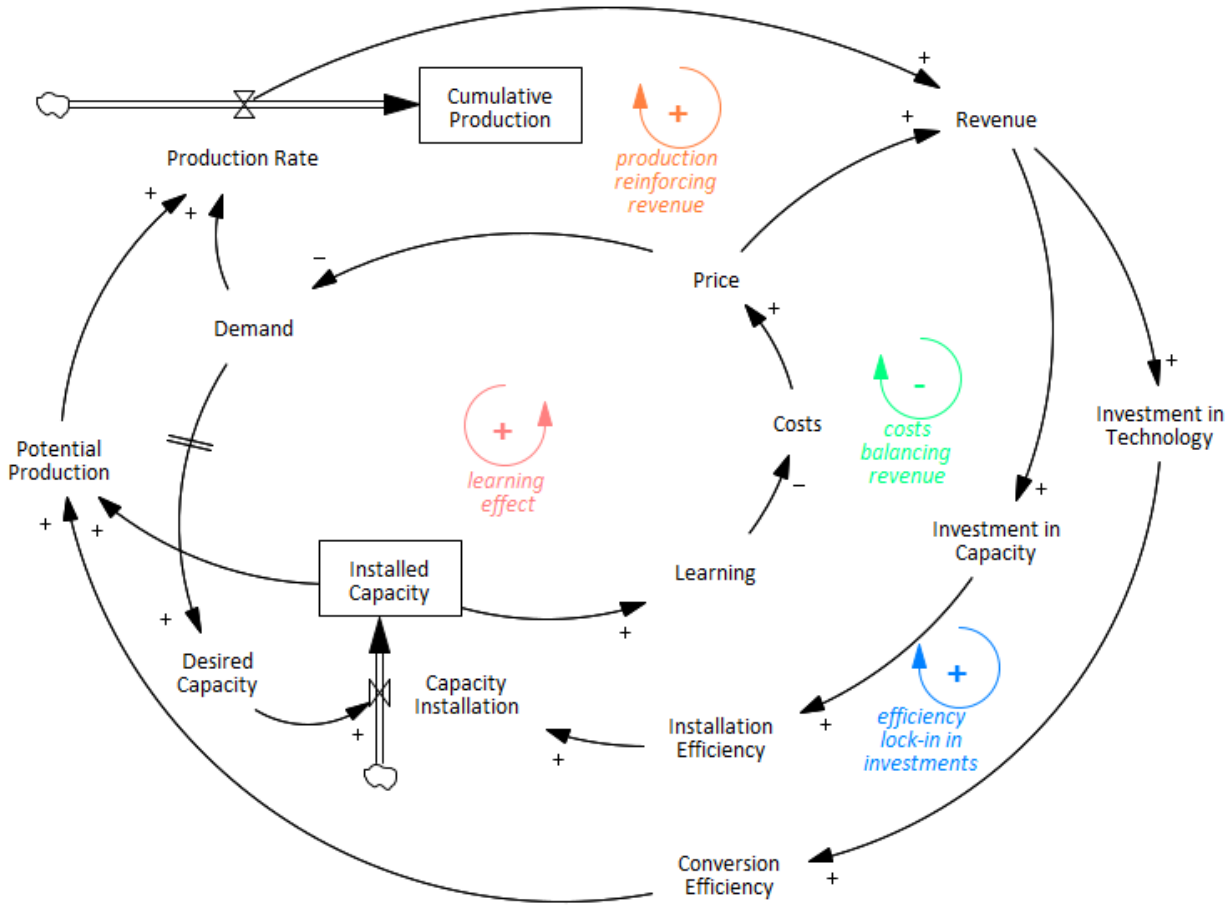

Figure 27: Overview of the model structure for renewable energy capacity development and production

Demand is determined by the market share of the corresponding source, e.g. solar, and the total *Energy Demand*, which drives the production. *Production rate,* however, is constrained by *Potential Production* that depends on the *Installed Capacity* and *Conversion Efficiency*. The factors specific to technologies, such as the weather for wind or solar radiation are also added to the formulation of the potential production. *Installed Capacity* is the accumulation of the difference between new capacity installations and depreciation due to ageing. In FeliX, installed capacity of solar and wind energy is measured in terms of area (m^2) to take the land constraints into account explicitly. Correspondingly, sun radiation is assumed to be 1.3 kW/m^2 and the average power density for wind is estimated as 0.0191 kW/m^2 based on the historical observations and the assumption of 93% onshore, 7% offshore wind (Enevoldsen & Jacobson, 2021).

Capacity Installation includes the replacement of depreciated infrastructure as well as the difference between the desired and currently available capacity. The *Desired Capacity* is adjusted by a factor of *Installation Efficiency* due to technology advancement resulting from investments.

Conversion Efficiency, that represents the energy productivity of the infrastructure, e.g. solar panels, is driven by the investment in technology and is the main factor determining potential production.

As in the case of fossil fuels, investments are determined by the revenue, meaning that independent investments in renewable energy are not taken into account and all investments are considered in a closed system. This is a difference of the model from reality, yet captures the profitability dimension in investment decisions.

Revenue is determined by the production volume and *Price,* which mainly depends on the costs, a constant profit margin and the supply-demand ratio. The costs are formulated, in line with the simple LCOE calculations, as the sum of installation costs (CAPEX) and operational costs (OPEX), where the former also includes financial costs. The learning effects are formulated with respect to the ratio of *Installed Capacity* to a threshold value of it. For every doubling of this ration, the installation costs decline by the learning rate, which is taken as 25% and 20% for solar and wind, respectively.

The historical data used for calibrating the solar and wind modules is obtained from the following resources: Installed capacity and production volumes from the IRENA statistics (IRENA, 2024); costs and learning rates from IRENA Renewable Power Generation Costs report 2024 (IRENA, 2024); additional wind capex values from Lawrence Berkeley National Laboratory (LBL, 2025); and conversion efficiencies from NREL (NREL, 2025) and US DoE (DoE, 2022) for solar and wind, respectively.

Figure 28 below exemplifies the model output generated by the model structure described above in the Reference (baseline) simulation compared to the historical dynamics. The model captures the observed cost reduction dynamics relatively well, yet overestimates the capacity and production due to the simplified, price-based market share structure described in Section 4.2.

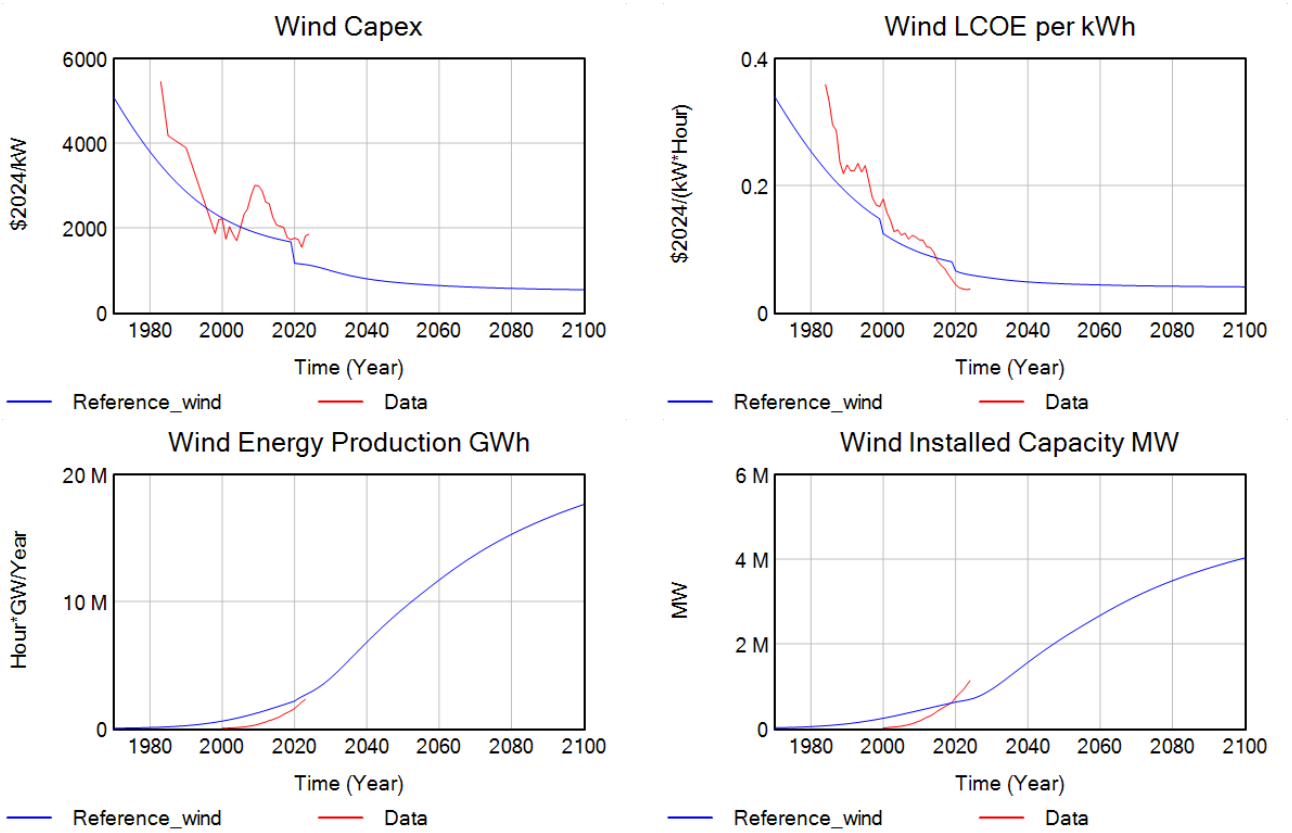

Figure 28: Capex, LCOE, Production and Installed Capacity values for the wind energy in the Reference simulation compared to the historical dynamics (Data source: IRENA, see the main text); the R^2 values between the model and data for these four variables are 0.595, 0.955, 0.899, and 0.954, respectively.

5. Water

The water module mainly quantifies global average water scarcity, that is, the balance between water availability and use. Water availability is a function of available water resources, water recovery of used water in economic sectors, and a drought rate for the impact of climate change. Total water use considers water withdrawal from economic sectors to meet their water demand.

5.1. Water supply and water availability

Available water resources consist of water supply rate of fresh and non-conventional water, water recovery rate of used water resources by the three economic sectors, and drought out rate representing extreme drought events. Water supply is estimated by multiplying desired water supply rate and water supply fulfillment rate (describing water supply fulfillment as a relation of water supply and demand). Desired water supply rate (*WatSupDes*) is to cover water consumption (*WatCons*, i.e., water use decreased by recovery of used water resources of three economic sectors) and available water resources adjustment (*WatAvailAdj*, taking into account dynamics of total water demand and water safety stock coverage).

$$WatSupDes(t) = \mathrm{MAX}\big(0, WatCons(t) + WatAvailAdj(t)\big) \tag{5.1}$$

With growing water demand, the supply fulfillment (*WatSupFul*) might be impaired which relates to infrastructure design and its operating limits. This relationship is modeled as a logistic function dependent on

the amount of water that can be reliably provided (*WatSupReli*) on annual basis for agricultural, industrial, and domestic sectors due to resources and infrastructure availability.

$$WatSupFul(t) = \frac{2}{1 + e^{-WatSupFulfParam * \frac{WatSupReli(t)}{WatSupDes(t)}}} \quad (5.2)$$

where *WatSupFulfParam* determines the strength of infrastructure operating limits on water supply fulfillment. Associated data are obtained from 2030 Water Resources Group (2009).

5.2. Water demand, water withdrawal, and water use

Water is demanded for economic production by agriculture, industrial, and domestic sectors. Agricultural water demand (*WatDem*$_{agr}$) is dependent on two ways of land watering—irrigation and rainfed.

$$WatDem_{agr}(t) = WatInt_{irr}(t) * A_{irr}(t) + WatInt_{rain}(t) * A_{rain}(t) \quad 5.3$$

where *WatInt*$_{irr}$ and *WatInt*$_{rain}$ represent average agricultural water demand per square (i.e., water intensity) of irrigated or rainfed agricultural areas, respectively. Irrigated agricultural land (*A*$_{irr}$) is calculated by multiplying total agricultural land areas with the percentage of irrigated land areas, which is estimated by considering the impact of wealth (represented by *GWP per Cap*) and their upper and lower limits. This approach is also applied to estimate water intensities and total water demand for industrial sector based on their own upper and lower limits, respectively. Domestic water demand is quantified based on total population and average domestic water demand per capita. Domestic water demand per capita is estimated by considering the impact of wealth (represented by *GWP per Cap*) and their upper and lower limits.

Agricultural, industrial, and domestic water demand drives water resources withdrawal from available water resources. Similar to water supply, agricultural, industrial, and domestic water withdrawal rates (e.g. *Withdrawal*$_{agr}$) slow down when their demands approaching max water withdrawal rate. This process is represented by water withdrawal fulfillment rate (*Fulfillment*). Particularly for agricultural water withdrawal (*Withdrawal*$_{agr}$), impacts from extreme drought (*drought*) is also considered to simulate the decrease in *Withdrawal*$_{agr}$ and available water resources due to drought.

$$Withdrawal_{agr}(t) = WatDem_{agr}(t) * Fulfillment(t) * (1 - drought) \quad (5.4)$$

Agriculture, industrial, and domestic water withdrawal rates accumulate as total used water resources. As mentioned in section 5.1, a fraction of total used water resources (set as 10%) can be recovered and supplied as available water resources.

6. Land use and agriculture

FeliX represents the global land use and land use change dynamics based on four main categories of land use as defined by FAO (FAO, 2025d): agricultural, forest, urban/industrial, and the other land that does not fall into any of the first three categories. Each land category is modeled as a stock variable. Land use change refers to the conversion of land among these four categories. Considering the historical and expected dynamics, we assume a bi-directional conversion between agricultural land and forest land and between the agricultural land and other land. The rest of land use changes are considered one directional conversion, that is, from agricultural land to urban and industrial land, from forest land to urban and industrial land, and from other land to forest land (Figure 29).

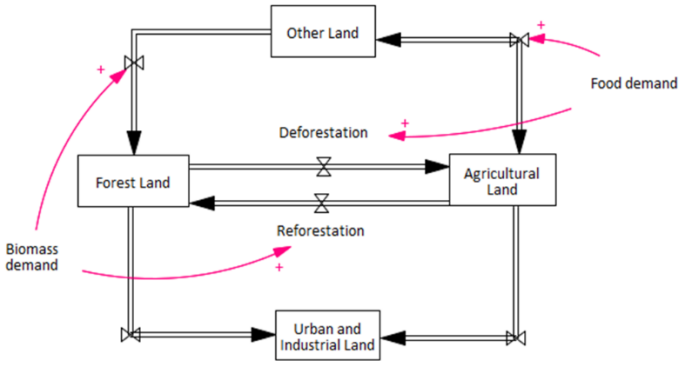

Figure 29: Stylized stock-flow diagram of land use module in FeliX

The main underlying driver of land use change is the food system, in addition to bioenergy and forest management practices. The land conversion flows are modeled to be dynamic natural or anthropogenic processes. For instance, abandoning any human activities in a part of agriculture land and allowing certain duration of time the agriculture land will be covered by grass, later by shrubs, yet later by trees and eventually it will be classified as forest. In case of forest–other land conversion, forest–agriculture land conversion and agriculture–other land conversion, there are additional forces apart from natural conversion processes that drive and increase the rate of expansion or shrinking of the forest, other and agriculture land areas. We set a constant ratio of other land and forest land areas as protected land. In case of forest land, the protected area increases successively. The protected areas are excluded from any transformation processes.

Agricultural land requirement increases due to the growing population and income levels which lead to more food demand. In Felix, agricultural land is further divided into three sub-categories as arable land, permanent cropland, and permanent meadows and pastures. Land use shifts due to food demand are considered based on plant- and animal-based food that have their own land allocation and yields.

FeliX includes 8 food categories: 4 plant-based categories that include pulses, grains, vegetables and fruits, and other crops such as sugar and oil crops; and 4 animal-based food categories that are pasture-based meat, crop-based meat, dairy, and eggs. This categorization of especially animal products were motivated by the land use shares: The pasture-based meat category includes the red meat sources such as beef, sheep and goat, since 96% of the global average land use per unit of beef production is attributed to pasture land, that is, 12 of 12.5 ha per million kcal (Ranganathan et al., 2016). As for poultry and pork, the average land use footprint is less than 2 hectares (ha), while a large portion of this is on cropland, since grains provide the 71% of the total feed demand (FAO, 2025c).

For each plant-based food category, the arable land needed (ALN_{Plant}) is formulated according to the desired production rate ($ProdDes_{Plant}$) and the expected crop yield ($YieldExp_{Plant}$), which is a 1-year time-averaged value of the crop yield over time.

$$ALN_{Plant}(t) = \frac{ProdDes_{Plant}(t)}{YieldExp_{Plant}(t)} \tag{6.1}$$

$ProdDes_{Plant}$ of each plant crop is the sum of the demand for that crop to be used as food, livestock feed, and in other sectors. The estimate procedures of crops to be used as food and livestock feed are described in the section. Crop to be used in other sectors is quantified as a constant ratio of total plant-based food demand. The actual production of each plant crop is the lower value of $ProdDes_{Plant}$ and the production volume calculated as crop yield multiplied by the area harvested. Crop yield is formulated with respect to a reference yield value in 2016 with the dynamic multiplicative impact of fertilizer application, water withdrawal rate and technology change. The total agricultural land requirements are estimated by dividing ALN_{Plant} by the annual share of arable land in the total agricultural land. The rest of agricultural land is proportionally distributed as permanent cropland and permanent meadows and pastures according to their annual share in agricultural land.

The discrepancy between agricultural land requirement and available agricultural land pushes agricultural production systems either towards more fertilizer use to increase the crop yields and reduce the land requirement, or to deforestation and other land requisition to expand the agricultural land. Eventually, food supply is dependent on the land available, hence harvested, for each food category, and the crop (or meat) yields that depend on fertilizer use, water availability and other agricultural management practices.

FeliX includes nitrogen and phosphorus fertilizer use in agriculture, from commercial sources or livestock manure. Both fertilizers, as well as their impacts, are modeled in a similar framework that focuses on chemical inflows to and outflows from agricultural land. Here we describe the model structure only for phosphorus (P) as an example.

Global *P* balance with major inflows and outflows follows an input and output framework (MacDonald et al., 2011) and the biochemical processes of phosphorus (Dumas et al., 2011). In general, the global P stock in soil accumulates with the commercial P fertilizer inflow and the inflow of manure as a fertilizer, and depletes with two outflows: the uptake by crops and the loss of P via erosion, leaching to freshwater systems and surface runoff. The residual P stock and flows are modeled in terms of the volume of elemental P, except the commercial fertilizer production and application, which are reported as the volume of P_2O_5 content and then converted to elemental P. The application of commercial P fertilizers is modeled as the minimum of P demand from agriculture and P supply. P demand from agriculture is formulated based on a reference application rate, taking into account the effect of income levels and land scarcity, capturing the phenomenon that wealthy countries use more fertilizers. Both effects are formulated as logistic functions based on GWP and the land pressure (ratio of global agricultural land demand to the available agricultural land), respectively. P supply for agriculture is a fraction of the total P rock extraction. This fraction is set as 0.9, since the agricultural use has been on average 90% of the total P_2O_5 produced between 2002 and 2015. P uptake by crops are estimated as a weighted average of the P contents in individual food category, using the data from USDA Food Composition Databases (USDA, 2020). We assume a nonlinear relation between P uptake and crop yields, based on the agronomic dynamics of crop growth (Yin & Struik, 2010) that result in sigmoid growth.

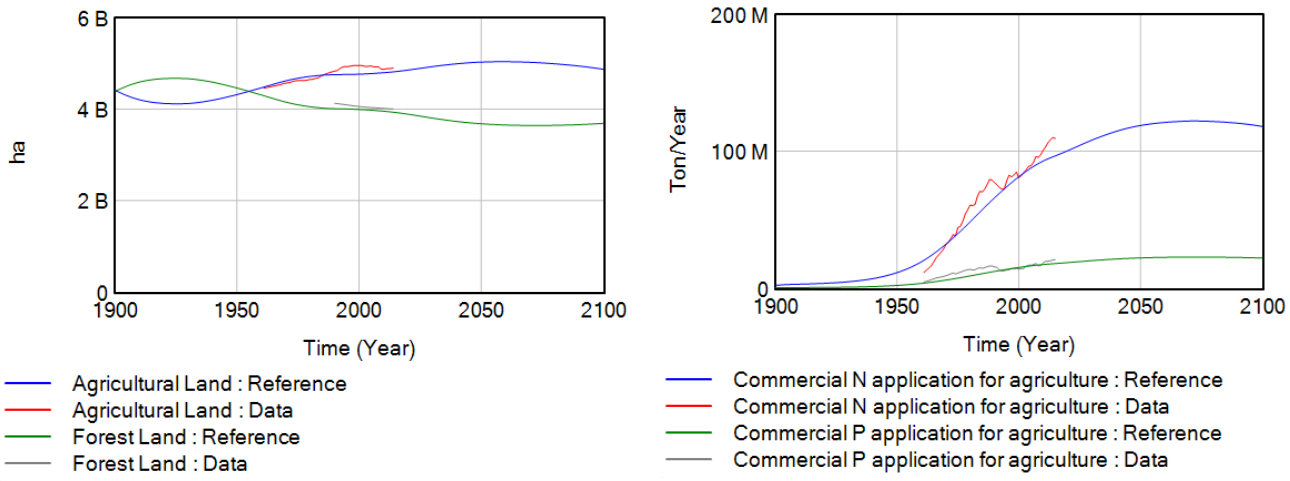

(a) Agricultural and Forest Land **(b)** Commercial N and P Fertilizer Application

Figure 30: Land use (a) and fertilizer application (b) in the Reference simulation compared to the historical dynamics (Data source: FAO, 2025c).

7. Biodiversity

The biodiversity module is based on population carrying capacity, representing global biomes mean species abundance (*MSA*). *MSA* is formulated as a stock variable increased by species regeneration rate (*Regeneration*) and decreased by species extinction rate (Extinction). In addition, *MSA* approaching species carrying capacity (*SpecCapacity*) limits the *regeneration* rate and intensifies the extinction rate. These processes are quantified as logistic functions and based on the ratio between the *MSA* and the species capacity, the regeneration factor and the extinction factor.

$SpecCapacity$ is calculated based on the maximum value of species carrying capacity ($SpecCapacity_{Max}$), representing maximum sustained population size, and influencing factors related to fertilizers consumption ($Impact^{Fertilizer}_{Biodiversity}$), biomass production for energy purposes ($Impact^{Biomass}_{Biodiversity}$), climate damage ($Impact^{Climate}_{Biodiversity}$) and land use change ($Impact^{Land}_{Biodiversity}$). The four influencing factors are estimated by logistic functions. All these drivers are known to adversely affect biodiversity, yet their precise impacts are not quantified yet. Therefore, these functions are quantified to explore different scenarios but not calibrated formally due to the lack of data. Still, the rate of change in MSA indicator aligns with other modeling studies (Leclère et al., 2020; Schipper et al., 2020) in terms of the order of magnitude and the rate of change in 2010-2050.

$$SpecCapacity(t) = SpecCapacity_{max} * Impact^{fertilizer}_{biodiversity}(t) * \\ * Impact^{biomass}_{biodiversity}(t) * Impact^{climate}_{biodiversity}(t) * Impact^{land}_{biodiversity}(t) \quad 7.1$$

8. Food demand and social dynamics

In the FeliX model, social dynamics of dietary shifts are captured by dividing the population into two groups (in addition to gender and age sub-groups): (i) Conventional diet followers, such as meat eaters, and (ii) alternative diet followers, such as vegetarians. The population flows between these two dietary choices depend on income (represented by GDP per capita) and social and behavioral factors such as climate and health risk

perception, self-efficacy and social norms that underly pro-environmental behavior. The modelling of these psychosocial mechanisms is described in Eker et al. (2019).

Followers of conventional and alternative diets are assumed to consume a predefined mix of eight food categories. The dietary compositions for each of these two consumer groups are taken into account in terms of the fractions of the total daily caloric demand, whereas the total caloric consumption is assumed to be gender and age dependent based on the caloric need estimates by the USDA Center for Nutrition Policy and Promotion (USDA, 2020). The model includes the flexibility to assign a different dietary composition to each consumer group. For instance, the conventional diet followers can be assumed to consume the world's average diet as estimated from the FAO Food Balance Sheets, and the alternative diet followers can be assumed to consume a flexitarian, that is, EAT-Lancet diet (Springmann et al., 2018).

Equation 8.1 exemplifies the demand calculations for grains as a representative of the eight categories. Total annual caloric demand for grains ($FoodDemand_{grains}$) is the sum of total grain-based caloric intake by the conventional and alternative diet followers, where $Intake_{grains,alt}$ is the annual per capita intake of grain-based calories in the alternative diet. Pop_{alt} refers to the population of alternative diet followers. This average intake (Equation 8.2) is a fraction of the annual total caloric intake per capita ($Intake_{total}$), and the fraction ($p_{grains,alt}$) is 52%. The global average of total caloric consumption per capita has been increasing in the past decades mainly due to increasing wealth. Therefore, $Intake_{total}$ is formulated (Equation 8.3) as the multiplication of a reference intake per capita ($Intake_{total}^{*}$) and the effect of income on food intake. The effect of income on food intake is a logistic function calibrated according to the historical data of the Gross World Product and average total caloric consumption.

$$FoodDemand_{grains}(t) = \left(Intake_{grains,alt}(t) * Pop_{alt}(t) + Intake_{grains,conven}(t) * Pop_{conven}(t)\right) \quad (8.1)$$

$$Intake_{grains,alt}(t) = p_{grains,alt} * Intake_{total}(t) \quad (8.2)$$

$$Intake_{total}(t) = Intake_{total}^{*} * f_{income}\left(GWP\ per\ cap(t)\right) \quad (8.3)$$

Since caloric intake depends on age and gender, $Intake_{total}$ was adjusted for each age cohort and gender based on the estimated calorie needs for moderate activity levels. We did not include heterogeneity for physical activity levels, assuming that the moderate level represents the average of various activity and consumption levels. Therefore, Equation 8.1 can be written in detailed form as in Equation 8.4.

$$FoodDemand_{grains}(t) = \sum_{i}\sum_{j}\begin{pmatrix} Intake_{grains,alt,i,j}(t) * Pop_{alt,i,j}(t) + \\ Intake_{grains,conven,i,j}(t) * Pop_{conven,i,j}(t) \end{pmatrix} \quad (8.4)$$

Food production in the model was eventually steered by waste-adjusted food demand. In other words, the food demand including waste ($FoodDemand^{waste}$) was formulated as in Equation 8.5, where w_{grains} is the waste fraction of supply. For grains, the waste fraction is 0.30, meaning that 30% of all grain production is eventually wasted. For vegetables, fruits, roots and tubers, the waste fraction is 45%, and for the remaining food categories, it is 20% (FAO, 2015)

$$FoodDemand_{grains}^{waste}(t) = \frac{FoodDemand_{grains}(t)}{1 - w_{grains}} \quad (8.5)$$

9. Nutrition

The Nutrition Module in FeliX focuses on estimating caloric and nutritional availability based on the food produced. It serves two main purposes. First, it links nutritional outcomes to social indicators such as health and well-being, allowing for a better understanding of how food system performance affects human development. Second, it establishes key baseline indicators to assess the efficiency of food systems, for example, measuring freshwater withdrawal per unit of protein.

9.1. Caloric and Nutritional Availability

Availability refers to the amount of food content available for human consumption after losses in the supply chain, but before accounting for food waste at the consumer level. While this does not represent actual intake, availability is commonly used for health-related metrics (such as PoU) because it is more readily available than direct intake data.

Caloric Availability captures the total amount of energy available from food (Equation 9.1) and also how they might be distributed based on age-sex subgroup (Equation 9.2). The caloric value ($CalValue_{Food}$) used is calculated using FAO (2025c) data on food supply in calories, divided by production in tonnes, and then reaggregated into the eight FeliX food categories. The caloric distribution of availability ($CalDistribution_{Age,Sex}$) is assumed to be a constant that follows the same distribution of caloric demand in each group (Age, Sex). Both distributions are estimated based on a reference dataset from 2000-2015.

For total caloric availability:

$$CalAvail(t) = \sum_{Food} Supply_{Food}(t) \times CalValue_{Food} \tag{9.1}$$

For each Age-Sex subgroup:

$$CalAvail_{Age,Sex}(t) = CalAvail(t) \times CalDistribution_{Age,Sex} \tag{9.2}$$

Where:

- $Food$ indexes food items,
- Age, Sex index age and sex groups,
- $CalDistribution_{Age,Sex}$ is the share of calories allocated to group (Age, Sex) (assumed constant, based on a reference from 2000–2015).

Nutritional Availability accounts for key macronutrients—i.e. fat and protein—available in the food supply. The model captures total nutrient availability (Equation 9.4), disaggregated by food categories (Equation 9.3) and further by age–sex groups (9.5). Nutritional values ($NutrValue_{Food,Nutr}$) are calculated using FAO (2025c) data on protein and fat availability, divided by total food availability in calories, and then reaggregated into the eight FeliX food categories. The distribution of nutrients based on age-sex groups follows the caloric distribution ($CalDistribution_{Age,Sex}$).

For each Nutrient and Food:

$$NutrAvail_{Food,Nutr}(t) = Supply_{Food}(t) \times NutrValue_{Food,Nutr} \tag{9.3}$$

Total availability of each Nutrient:

$$NutrAvail_{Nutr}(t) = \sum_{Food} N\,utrAvail_{Food,Nutr}(t) \tag{9.4}$$

For each Age-Sex subgroup:

$$NutrAvail_{Nutr,Age,Sex}(t) = NutrAvail_{Nutr}(t) \times CalDistribution_{Age,Sex} \tag{9.5}$$

where $Nutr$ indexes nutrients, i.e., protein and fat.

Both Caloric and Nutritional Availabilities are compared with historical data from FAO (2025c), where caloric and nutritional values are further calibrated (within 15% alignment of historical values) to have a better fit with historical data. The model generally displays a good fit for both availabilities. As illustrated in Figure 31, the model provides a detailed representation of each nutrient by food category, capturing food-level detail that is important for analyses such as examining how diet composition influences nutritional intake.

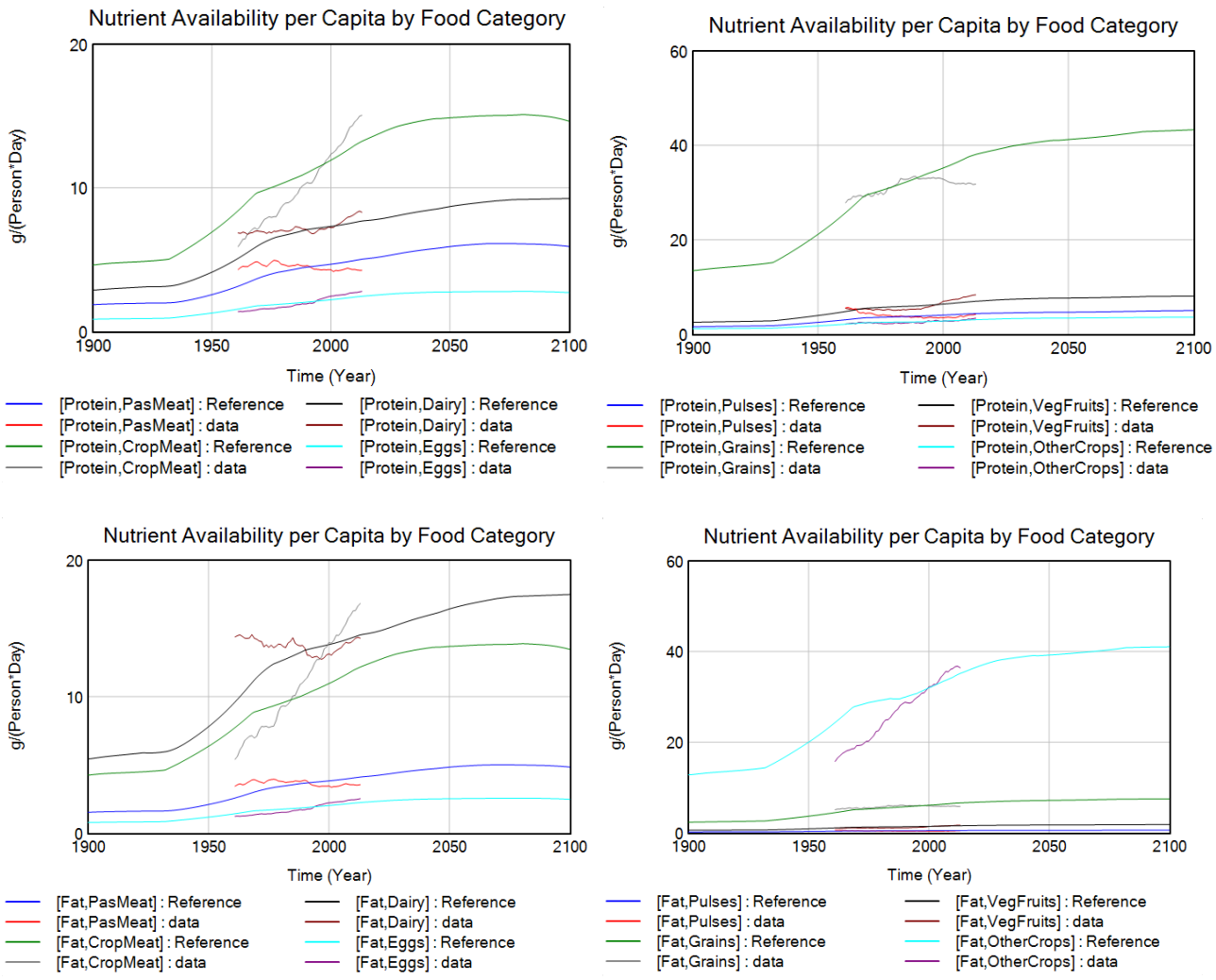

Figure 31: Comparing historical and simulated nutritional availabilities. Rows in this figure are by Nutrient Type (i.e. Protein and Fat, respectively). Columns are by Food Type (i.e. Animal Food and Plant Food, respectively). All simulated results show a good fit against FAOSTAT data.

9.2. Prevalence of Undernutrition (PoU)

Prevalence of Undernourishment (PoU) is the Sustainable Development Goal (SDG) Indicator 2.1.1, used to monitor progress towards ending hunger and ensuring access to safe, nutritious and sufficient food. PoU effectively estimates the proportion of a population whose habitual dietary energy consumption is insufficient to meet the minimum energy requirements for an active and healthy life.

It is calculated by comparing the distribution of Dietary Energy Supply (DES) with the Minimum Dietary Energy Requirement (MDER). The DES represents the average per capita caloric availability of food, while the MDER defines the lower threshold of adequate intake for each population group. By integrating these two measures, the PoU quantifies the share of individuals whose energy consumption falls below the minimum required level. This approach follows the FAO (2014) methodology and is calibrated using Food Balance Sheet data (FAO, 2025c).

Log-Normal Distribution of Dietary Energy Supply

For each age–sex subgroup, the Dietary Energy Supply is modelled using a lognormal distribution (see Equation 9.6). This distribution adequately represents empirical patterns of energy supply across populations. The lognormal form is particularly appropriate as it is bounded by zero, reflecting the realistic condition that no individual within a population cohort can have a negative energy intake. The main parameters of the distribution are the mean (μ), which corresponds to the caloric availability described in the previous section, and the variance (σ^2), which captures the degree of variability—larger values indicate greater dispersion.

The formulation applied is the updated approach of FAO (2014), which incorporates a skewness parameter to the original formula by Naiken (2002) for the purpose of capturing distributional (a)symmetries at national or regional scales, such as increasing inequalities within populations. As FeliX is at an aggregated global scale, the baseline assumption is no skew and that any variation of this skew can be explored in scenario experiments or the Regional FeliX.

$$\ln\left(DES_{Age,Sex}(t)\right) \sim \mathcal{N}(\mu, \sigma^2, \alpha) \tag{9.6}$$

where:

- Mean: $\mu = \ln\left(CalAvail_{Age,Sex}(t)\right) - \frac{\sigma^2}{2}$
- Variance: $\sigma = 0.3$ (average variability based on FAO (2025c) from 2000-2024)
- Skew: $\alpha = 0$ (baseline assumes no skew)

Minimum Dietary Energy Requirement (MDER)

Human energy requirements for an individual in a given sex/age class are determined based on normative requirements for basic metabolic rate (BMR) per kilogram of body mass, multiplied by the ideal weights that a healthy person of that sex/age class may have, given his or her height, and then multiplied by a coefficient of physical activity level (PAL) to take into account physical activity.

Specific formulas for basal metabolic rate (BMR) are provided in the Human Energy Requirements report (FAO, 2008). BMR estimates rely on BMI reference values from WHO guidelines combined with average heights from WHO growth standards (WHO, 2025).

$$MDER_{Age,Sex} = BMR_{Age,Sex} \times PAL_{Age,Sex} \tag{9.7}$$

where:

- $BMR_{Age,Sex}$ = basal metabolic rate for the subgroup (kcal/day), depending on age, sex, and body weight.
- $PAL_{Age,Sex}$ = physical activity level, reflecting typical energy expenditure. Here we assume $PAL = 1.5$ based on UN guidelines.

Prevalence of Undernourishment

The PoU for each subgroup is the probability that DES is below MDER. The total PoU for the population is obtained by aggregating across all subgroups, weighted by population size.

$$PoU_{Age,Sex}(t) = P\left(DES_{Age,Sex}(t) < MDER_{Age,Sex}\right) = \Phi\left(\frac{\ln\left(MDER_{Age,Sex}\right) - \mu}{\sigma}\right) \tag{9.8}$$

$$PoU_{Total}(t) = \sum_{Age,Sex} PoU_{Age,Sex}(t) \cdot Population_{Age,Sex}(t) \tag{9.9}$$

where Φ is the standard normal cumulative distribution function (CDF)

Figure 32 compares historical and simulated values for Dietary Energy Supply (DES), Minimum Dietary Energy Requirement (MDER), and the resulting Prevalence of Undernourishment (PoU). Both DES and MDER show very good agreement with historical data, supporting the assumption of a constant standard deviation (spread) of 0.3 for the period 2000–2024. Because PoU is derived from the relationship between DES and MDER, this close fit results in a strong fit for PoU as well. However, as seen in PoU estimates before the 1950s—where values are extremely high—these default parameters may differ depending on historical context. From 1950 onwards, though, the chosen parameters provide a reasonable and consistent representation of undernourishment.

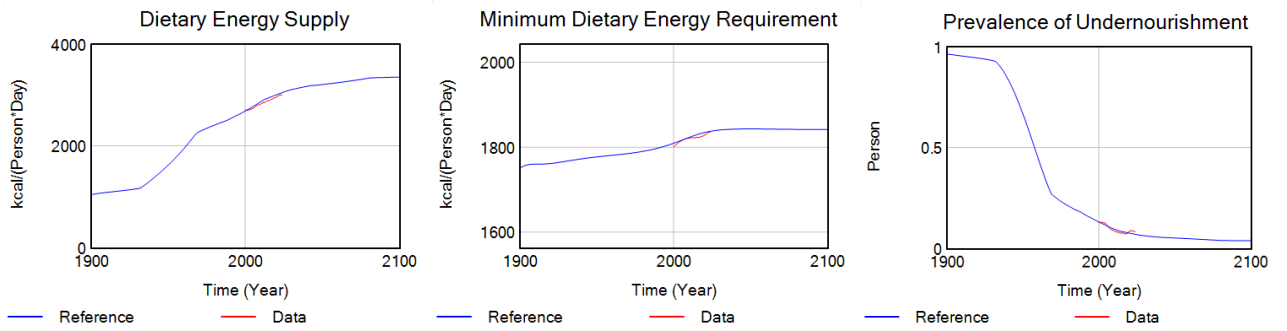

Figure 32: Comparing historical and simulated Dietary Energy Supply (DES), Minimum Dietary Energy Requirement (MDER), and Prevalence of Undernourishment (PoU). DES and MDER show close agreement with historical data, resulting in a strong fit for PoU. Extremely high PoU before the 1950s indicates parameter sensitivity in earlier periods, but from 1950 onwards, the model captures undernourishment accurately.

10. Emissions

FeliX models emissions of three major greenhouse gases: CO_2, CH_4, and N_2O. These emissions originate from four main sectors: (1) Agriculture, (2) LULUCF (Land Use, Land-Use Change, and Forestry), (3) Energy, and (4) Industry & Waste.

FeliX uses an activity-based emission accounting approach, in which it estimates emissions indirectly from activities and outputs across different sectors through emission factors. Emission factors ($EF^{Gas}_{Activity}$) are determined in this order of priorities: (1) IPCC default values, (2) Historical data calculations, (3) Model calibration.

$$Emis^{Gas}_{Activity}(t) = Activity(t) \times EF^{Gas}_{Activity},\ Gas \in CO_2, CH_4, N_2O \tag{10.1}$$

The key activities contributing to the various emissions are described in Table 4. Categories of activities from Agriculture, LULUCF and Industry & Waste are based on FAOSTAT (2025b), while Energy sector activities follow IEA (2025) guidelines. Emissions for individual activities are likewise calibrated from these sources, while aggregated emissions for each gas are calibrated using data from the RCMIP protocol (Nicholls et al., 2019).

Table 4: Sector, Activity, and Greenhouse Gas Emission Contributions.

Sector	Activity	CO_2	CH_4	N_2O	Equation
Agriculture	Livestock & Manure		●	●	10.2
	Rice Cultivation		●		10.3
	Crop Residue Burning		●	●	10.4
	Agricultural Soils			●	10.5
LULUCF	Burning Biomass	●	●	●	10.6
	Net Forest Conversion	●			10.7
	Forestland	●			10.8
	Drained Organic Soils	●			10.9
Energy	Oil Production	●	●	●	10.10–12
	Coal Production	●	●	●	10.10–12
	Gas Production	●	●	●	10.10–12
	Biomass Production	●	●	●	10.10–12
	Solar Production	●			10.10–12
	Wind Production	●			10.10–12
Industry & Waste	Waste Disposal		●		10.13
	Industrial Activity			●	10.14

10.1. Agriculture Emissions

Agriculture activities contribute primarily to CH4 and N2O emissions. FeliX quantifies agricultural emissions based on the production rate of various food items (see Land use and agriculture). Even the emission formula from agricultural soils ($Emis^{N2O}_{AgricultureSoils}$) which are based on IPCC (2006) guidelines, are derived from nitrogen flows (N), which themselves are calculated using the production rates of animal-based food.

$$Emis^{Gas}_{LivestockManure}(t) = \sum_{AnimalFood} Prod_{AnimalFood}(t) \times EF^{Gas}_{LivestockManure} \times \frac{1}{Yield(t)},\ Gas \in CH_4, N_2O \tag{10.2}$$

$$Emis^{CH4}_{RiceCultivation}(t) = Prod_{Grains}(t) \times Grains\_to\_Rice\_Ratio \times EF^{CH_4}_{RiceCultivation} \quad (10.3)$$

$$Emis^{Gas}_{CropBurning}(t) = \sum_{PlantFood} Prod_{PlantFood}(t) \times Residue\_to\_Production \times EF^{Gas}_{CropBurning}, Gas \in CH_4, N_2O \quad (10.4)$$

$$Emis^{N2O}_{AgricultureSoils}(t) = N_{Commercial}(t) \times EF_{Direct} + N_{Manure}(t) \times EF_{Volatilization} + N_{Leaching}(t) \times EF_{Leaching} \quad (10.5)$$

where emission factors $EF^{Gas}_{LivestockManure}$, $EF^{Gas}_{RiceCultivation}$, and $EF^{Gas}_{CropBurning}$ were calculated from historical data in FAOSTAT based on the same relationship. For $EF^{Gas}_{LivestockManure}$, where the relationship between production and emissions was not linear due to productivity changes, an adjustment factor ($\frac{1}{Yield(t)}$) was introduced since emissions tend to be tied to animal heads rather than production rate (Dong et al., 2009).

Figure 33 compares simulated agricultural emissions from FeliX with historical data from FAOSTAT. The model shows a numerical fit for both CH_4 and N_2O emissions, and within expected range of aggregate emission levels across time. However, slight deviations are observed in behaviour fit, likely due to the limited representation of production-side dynamics and efficiency improvements within the model structure. Despite these differences, the main patterns and magnitudes of agricultural emissions are represented fairly.

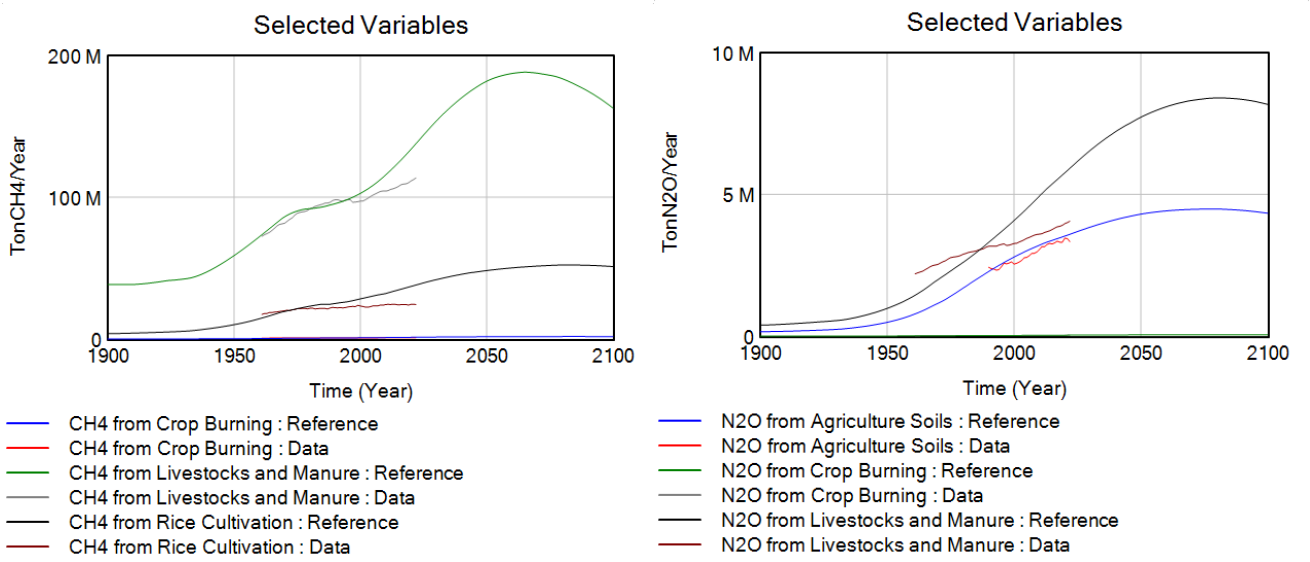

Figure 33: Agricultural emissions, comparing simulated results from FeliX with historical FAOSTAT data. The model reproduces CH_4 (left) and N_2O (right) emissions with good numerical fit, though some deviations in temporal behaviour arise from the simplified representation of production and efficiency factors.

10.2.LULUCF Emissions

Land Use, Land Use Change and Forestry (LULUCF) activities contribute primarily to CO_2 emissions, with minor contributions to N_2O and CH_4 from biomass burning. FeliX quantifies LULUCF emissions based largely on forest land changes and agricultural land changes relative to initial year 1900 stocks ($\frac{ForestLand(t)}{ForestLand_0}$ and $\frac{AgriLand(t)}{AgriLand_0}$ respectively). See Land use and agriculture for details on the drivers of land use changes.

$$Emis^{CO2}_{NetForest}(t) = \frac{ForestLand(t)}{ForestLand_0} \times EF^{CO2}_{NetForest} \quad (10.6)$$

$$Emis^{CO2}_{ForestLand}(t) = ForestLand(t) \times EF^{CO2}_{ForestLand} \quad (10.7)$$

$$Emis^{Gas}_{BurningBiomass}(t) = \frac{AgriLand(t)}{AgriLand_0} \times BurntFraction \times EF^{Gas}_{BurningBiomass}, Gas \in CO_2, CH_4, N_2O \quad (10.8)$$

$$Emis^{Gas}_{DrainedSoils}(t) = \frac{AgriLand(t)}{AgriLand_0} \times EF^{Gas}_{DrainedSoils}, Gas \in CO_2, CH_4, N_2O \quad (10.9)$$

where all emission factors $EF^{CO2}_{NetForest}$, $EF^{CO2}_{ForestLand}$, $EF^{Gas}_{BurningBiomass}$ and $EF^{Gas}_{DrainedSoils}$ were all calibrated within the model using FAO (2025d) emission data.

As illustrated in Figure 34, the simulated LULUCF emissions show a good fit with historical FAOSTAT data at the activity level, capturing the contributions of CO_2 from burning biomass, drained organic soils, and forest conversions, as well as CH_4 and N_2O from biomass burning. Note that CO_2 from Forestland ($Emis^{CO2}_{ForestLand}$) produces a negative value because it refers to the uptake of atmospheric carbon. This is part of the atmosphere to biomass flux in the carbon cycle (see Figure 37 in Carbon Cycle), alongside similar processes in other terrestrial, oceanic, freshwater and coastal ecosystems.

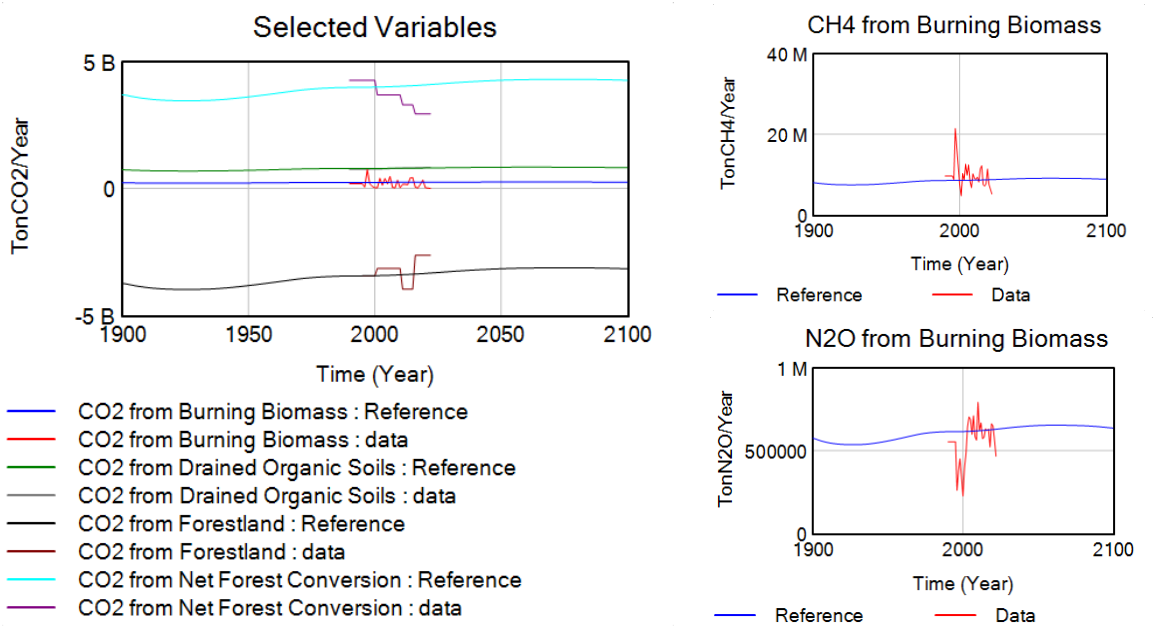

Figure 34: LULUCF Emissions, comparing simulated results from FeliX with historical data FAOSTAT. Much of LULUCF emissions are CO_2 across activities such as Burning Biomass, Drained Organic Soils, Forest Conversions, but also produce some CH_4 and N_2O from Burning Biomass.

10.3.Energy Emissions

Energy emissions contribute primarily to CO_2 emissions, with smaller contributions to CH_4 and N_2O. CO_2 is released from widespread fuel burning for electricity, heat, and transportation; CH_4 is emitted mostly from natural gas systems and coal mining; and N_2O arises from certain combustion processes for fossil fuels. The energy sector supports various end uses, including industrial activities, agricultural production, residential and commercial energy use, and transportation.

Emissions from the energy sector are based solely on the annual production rates of different fossil and renewable energy sources ($Prod_{Energy}$ in Energy), including oil, coal, gas, biomass, solar, and wind. Carbon emissions from fossil fuels also include the effect of carbon capture and storage technology.

$$Emis_{Energy}^{CO_2}(t) = \sum_{Energy} Prod_{Energy}(t) \times EF_{Energy}^{CO_2}, Energy \in Oil, Coal, Gas, Biomass, Solar, Wind \quad (10.10)$$

$$Emis_{Energy}^{CH_4}(t) = \sum_{Energy} Prod_{Energy}(t) \times EF_{Energy}^{CH_4}, Energy \in Oil, Coal, Gas, Biomass \quad (10.11)$$

$$Emis_{Energy}^{N_2O}(t) = \sum_{Energy} Prod_{Energy}(t) \times EF_{Energy}^{N_2O}, Energy \in Oil, Coal, Gas \quad (10.12)$$

where emission factors $EF_{Energy}^{CO_2}$, $EF_{Energy}^{CH_4}$, $EF_{Energy}^{N_2O}$ are calibrated to historical emissions within the uncertainty ranges of the unit emissions of energy production (IPCC, 2014).

Figure 35 compares simulated energy-related emissions from FeliX with historical data from IEA. The left panel presents total aggregate carbon emissions from fossil fuel combustion, showing both strong numerical agreement and consistent temporal behaviour with observed trends. The right panel presents CH_4 emissions by energy source—oil, gas, coal, and biomass—illustrating how sectoral contributions behave over time. Generally, the model captures the overall magnitude of energy emissions and their underlying source-level detail with reasonable accuracy.

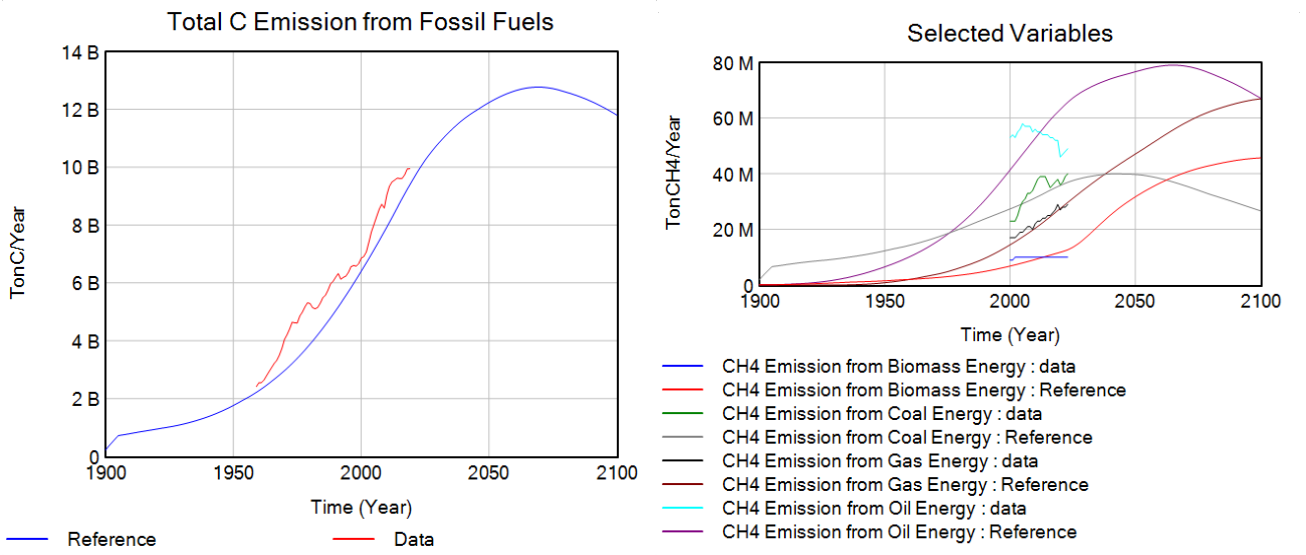

Figure 35: Energy emissions, comparing simulated results from FeliX with historical FAOSTAT data. Left: total aggregate carbon emissions from fossil fuels, showing good numerical and behavioural fit. Right: CH_4 emissions disaggregated by energy source (oil, gas, coal, biomass), illustrating consistent representation of source-level trends.

10.4.Industry and Waste Emissions

In FeliX, emissions from Industry and Waste are modeled indirectly through their relationship with Gross World Product (see GWP in Economy).

CH4 from Waste emissions are calculated using the Municipal Solid Waste (MSW) disposal rate, which is estimated from GWP using the IPCC (2000) formulation:

$$Emission_{Waste}^{CH_4}(t) = MSW(GWP)(t) \times EF_{Waste}^{CH_4} \quad (10.13)$$

where MSW is derived from a linear regression with GWP (gradient = 0.027, constant = 0.5695). The emission factor $EF_{Waste}^{CH_4}$ is calibrated within IPCC default uncertainty ranges, using a weighted average of different waste disposal site conditions.

N2O from Industry emissions are calculated as:

$$Emission_{Industrial}^{N_2O}(t) = Industrial\_Activity(t) \times EF_{Industrial}^{N_2O} \times Abatement\_Adoption(t) \quad (10.14)$$

where $Abatement\_Adoption(t)$ is modeled as a logistic curve from 1980-2000 with a maximum abatement fraction of 0.8, representing the gradual adoption of N_2O abatement technologies. The emission factor $EF_{Industrial}^{N_2O}$ is calibrated using FAO (2025b) emission data.

Figure 36 compares simulated industry and waste emissions from FeliX with historical FAOSTAT data. The left panel shows CH_4 emissions from waste, which display a very good numerical and behavioural fit with historical trends, showing the accuracy of IPCC's linear regression formula for MSW. The right panel presents N_2O emissions from industry and waste, which also show a good overall fit. This illustrates the usefulness of abatement adoption representation, which captures the flattening of the N_2O emission curve over time.

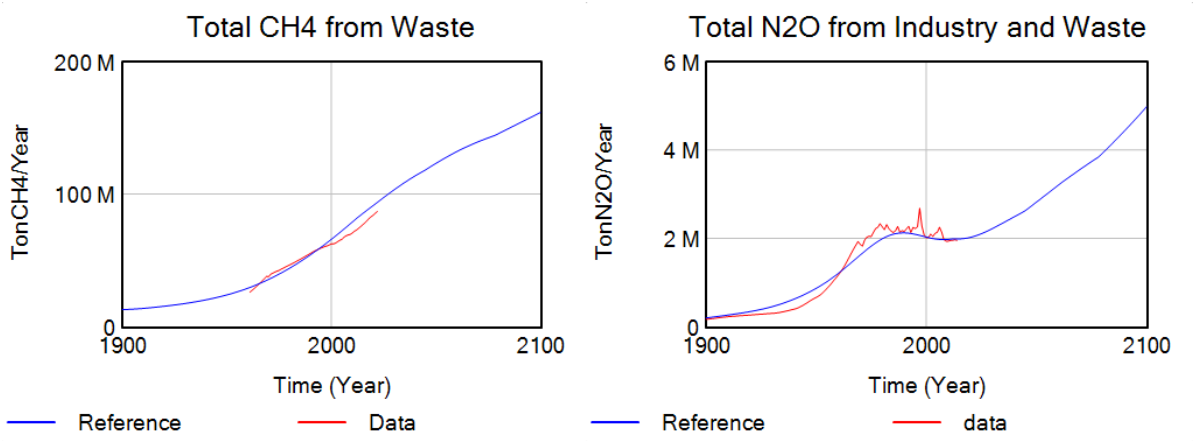

Figure 36: Industry and waste emissions, comparing simulated results from FeliX with historical FAOSTAT data. Left: CH_4 emissions from waste, showing good numerical and behavioural fit. Right: N_2O emissions from industry and waste, with good fit due to the abatement adoption and the resulting flattening of emission trends.

11. Gaseous Cycles

FeliX models the atmospheric cycles of three major greenhouse gases: CO_2, CH_4, and N_2O. These gases accumulate in the atmosphere through emissions from various sectors (see Emissions). The atmospheric concentrations are calculated by converting their respective stocks (C_Stk_{Atm}, $CH4\_Stk_{Atm}$, and $N2O\_Stk_{Atm}$) from mass units (tons) to volume mixing ratios (ppm or ppb), using their molar masses and the total number of moles in the atmosphere.

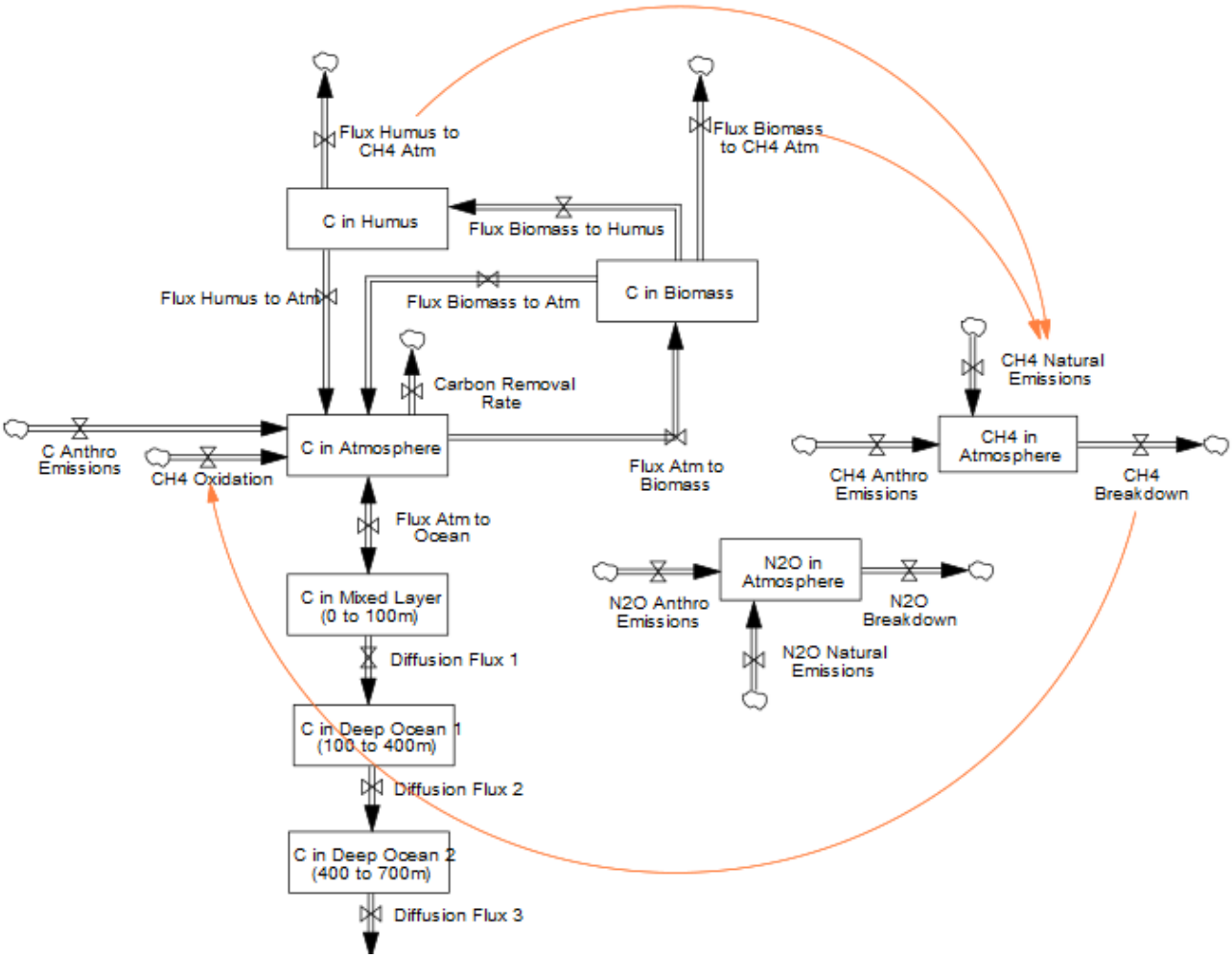

Figure 37: Stocks and associated flux for major greenhouse gases (i.e., CO_2, CH_4, N_2O) in FeliX

CO_2 is modeled explicitly through exchanges with the atmosphere, biosphere, soil, and ocean on C-ROADS (J. Sterman et al., 2012; J. D. Sterman et al., 2013), while CH_4 and N_2O are represented as first-order impulse-response with single atmospheric stocks with chemical lifetimes adapted from FaIRv2.0.0 (Leach et al., 2021).

The cycles of these gases are also interconnected in the atmosphere. Orange arrows in Figure 37 indicate key interactions: carbon fluxes from soil and biomass generate natural CH_4 emissions, linking the CO_2 and CH_4 cycles. Furthermore, the breakdown of CH_4 in the atmosphere produces carbon compounds, creating a feedback into the carbon cycle.

11.1.Carbon Cycle

Stocks of carbon are considered in the atmosphere, biosphere, mixed ocean layer, and four deep ocean layers (Figure 37). Carbon in the atmosphere (C_Stk_{Atm}) accumulates through total carbon emissions formulated above. Carbon in the biosphere is captured in biomass (C_Stk_{Biom}) and soil (C_Stk_{Soil}). C_Stk_{Biom} includes carbon stock in leaves, branches, stems, and roots, whereas C_Stk_{Soil} includes carbon stock in litter and humus. As the concentration of C_Stk_{Atm} rises, it forces an increase of the uptake by ocean and biosphere. Carbon flux from the atmosphere to the biomass is modeled according to the formula in Wullschleger et al. (1995) and grows logarithmically as the concentration of C_Stk_{Atm} increases. The residence of C_Stk_{Biom} depends on average lifespan. The outflow of C_Stk_{Biom} is partitioned between carbon flux from the biomass to the atmosphere and to the humus according to humification fraction. The outflow from C_Stk_{Soil} is equal to its content divided by its average lifespan in the humus. The flux between C_Stk_{Atm} and carbon stock in the mixed ocean layer (C_Stk_{Ocn}) adjusts to an equilibrium that considers buffer factor, a measure of the resistance to atmospheric carbon dioxide being absorbed by the ocean surface layer. The buffer factor itself rises with the atmospheric concentration which decreases ocean absorption capacity. Deep ocean diffusion fluxes are modeled as a simple eddy-diffusion structure.

11.2.Methane Cycle

Methane (CH_4) is modeled as a first-order impulse-response system with a single atmospheric stock. The system includes inflows from natural and anthropogenic emissions, while outflows occur through atmospheric breakdown with a chemical lifetime ($\tau_{CH_4} \approx 12$ years).

Atmospheric Methane Stock:

$$CH4\_Stk_{Atm}(t+1) = CH4\_Stk_{Atm}(t) + Emis^{CH4}_{Anthropogenic}(t) + Emis^{CH4}_{Natural}(t) - \frac{CH4\_Stk_{Atm}(t)}{\tau_{CH_4}(t)} \quad (11.1)$$

Natural Methane Emissions:

$$Emis^{CH4}_{Natural}(t) = (C\_Flux_{Biom \to CH4Atm} + C\_Flux_{Soil \to CH4Atm}) \times Effect\big(TempChange(t)\big) \quad (11.2)$$

where $Effect\big(TempChange(t)\big)$ represents the impact of temperature change on biological CH_4 release.

Methane Lifetime Dynamics:

$$\tau_{CH_4}(t) = \tau_0 \times Effect\big(TempChange(t)\big) \times Effect\left(\frac{N(t)}{N_0}, \frac{M(t)}{M_0}\right) \quad (11.3)$$

where τ_0 is the baseline lifetime, $Effect\big(TempChange(t)\big)$ is the temperature-dependent scaling factor, and $Effect\left(\frac{N(t)}{N_0}, \frac{M(t)}{M_0}\right)$ accounts for the influence of atmospheric N_2O and CH_4 concentrations. Formula is inspired by the FaIR Model (Leach et al., 2021) and calibrated in FeliX.

11.3.Nitrous Oxide Cycle

Nitrous oxide (N_2O) is modelled as a first-order impulse-response system with a single atmospheric stock. The system includes inflows from natural and anthropogenic emissions, while outflows occur through stratospheric reactions with a chemical lifetime ($\tau_{N_2O} \approx 114$ years).

Atmospheric Nitrous Oxide Stock:

$$N2O\_Stk_{Atm}(t+1) = N2O\_Stk_{Atm}(t) + Emis^{N2O}_{Anthropogenic}(t) + Emis^{N2O}_{Natural}(t) - \frac{N2O\_Stk_{Atm}(t)}{\tau_{N_2O}(t)} \quad (11.4)$$

Natural Nitrous Oxide Emissions:

$$Emis^{N2O}_{Natural}(t) = Emis_0 \times Effect\big(TempChange(t)\big) \quad (11.5)$$

where $Effect\big(TempChange(t)\big)$ represents the impact of temperature change on biological N₂O release.

Nitrous Oxide Lifetime Dynamics:

$$\tau_{N_2O}(t) = \tau_0 \times Effect\big(N2O_{Stk(t)}\big) \quad (11.6)$$

where τ_0 is the baseline lifetime, and $Effect\big(N2O\_Stk(t)\big)$ is a scaling factor that grows exponentially with atmospheric N_2O stock. Formula is adapted from the FaIR model (Leach et al., 2021) and calibrated in FeliX.

Figure 38 presents the comparison of atmospheric concentrations for CO_2, CH_4, and N_2O with respect to historical data, which serve as key indicators for assessing the reliability of each gas cycle in FeliX. Among these, CO_2 and N_2O show very good numerical and behavioural agreement with observed atmospheric concentrations, indicating that the model represents their respective emission sources and sinks well. CH_4 exhibits a weaker fit, largely due to the challenges in accurately capturing methane emissions, which are highly sensitive to technological factors and activity-level details. Additionally, the short atmospheric lifetime of CH_4 causes its concentration to respond quite sensitively to variations in emissions.

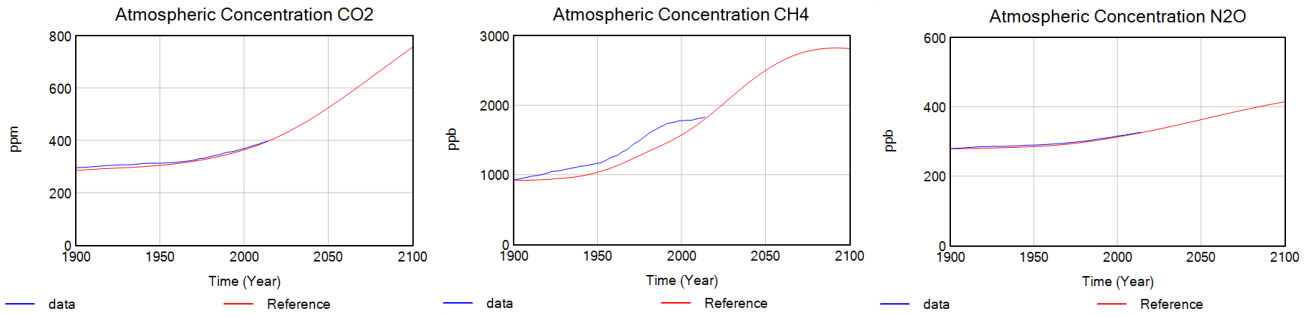

Figure 38: Comparison of simulated atmospheric concentrations for CO_2, CH_4, and N_2O with respect to historical data taken from the RCMIP protocol. CO_2 and N_2O show strong numerical and behavioural fit with observations, while CH_4 displays greater deviation due to its sensitivity to technological and activity-level factors and its shorter atmospheric lifetime.

12. Climate

The climate module in FeliX is based on the C-ROADS model (J. Sterman et al., 2012), which in turn refers to FREE model (Fiddaman, 2002) and DICE model (W. D. Nordhaus, 1992). The Earth's radiation budget is constrained to the temperature change due to carbon dioxide (CO_2), methane (CH_4), nitrous oxide (N_2O), halocarbons and other forcings (e.g., aerosols, O_3, etc.).

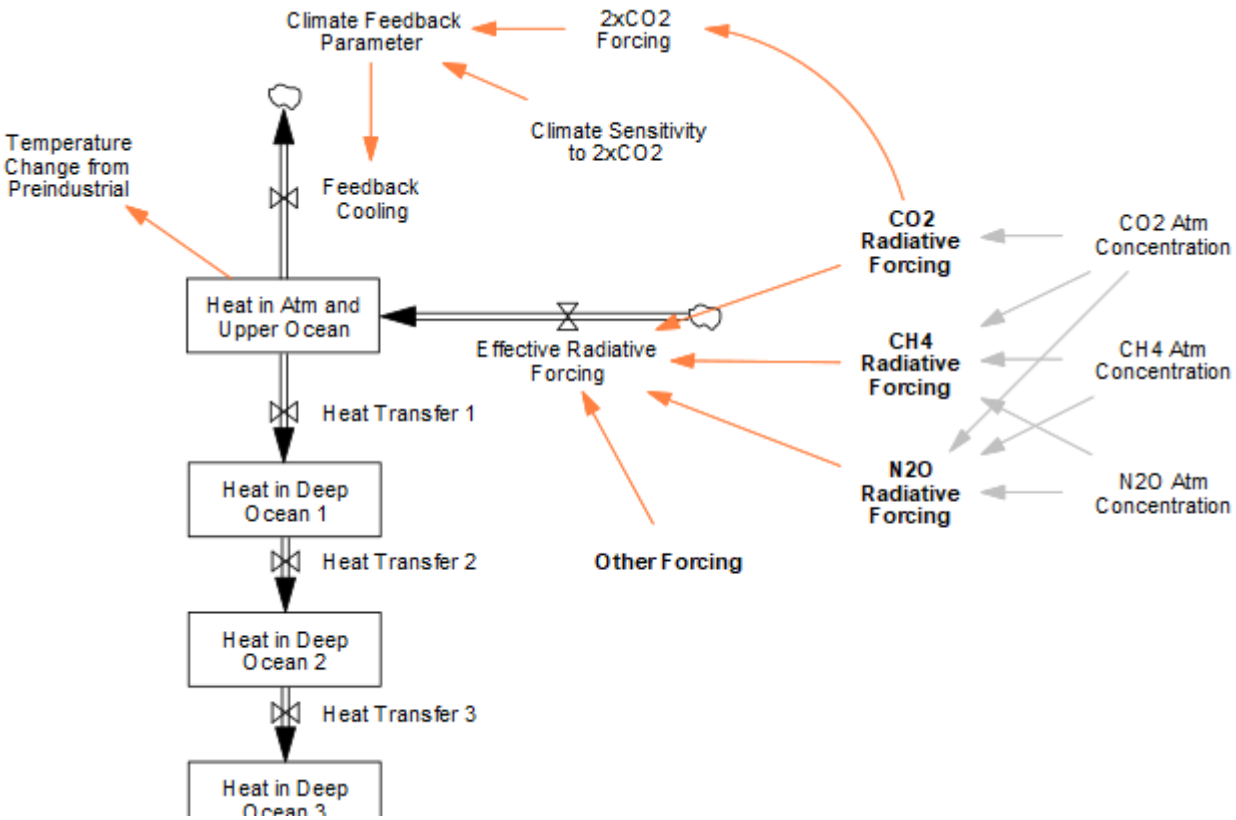

Figure 39: Energy Balance Model. Heat is exchanged among the atmosphere and upper ocean, and four deep ocean layers. The figure illustrates the different heat fluxes that drive the climate system in this model.

As shown in Figure 39, the temperature change in the model is driven by three main mechanisms: radiative forcings from greenhouse gases, feedback cooling from outbound longwave radiation, and heat transfer between atmospheric-upper ocean and deep ocean layers. The temperature change ($TempChange$) is calculated as the ratio of current heat content in the atmosphere and upper ocean ($Heat_{AtmUpperOcn}$) to their combined heat capacity:

$$TempChange = \frac{Heat_{AtmUpperOcn}}{HeatCapacity_{AtmUpperOcn}} \tag{12.1}$$

12.1. Radiative Forcing

In FeliX, temperature change is driven by forcings from CO_2, CH_4, and N_2O, computed based on atmospheric concentrations as described in Gaseous Cycles. These three gases account for approximately 87% of total anthropogenic effective radiative forcing as of 2019, according to IPCC AR6 (IPCC, 2023). The remaining forcings are generated exogenously based on historical data and the future projections from Representative Concentration Pathways (RCPs) (Byers et al., 2022).

Total effective radiative forcing (RF_{gas}) is the sum of the contributions from CO_2, CH_4, and N_2O and other climate drivers:

$$RF_{Total}(t) = RF_{CO2}(t) + RF_{CH4}(t) + RF_{N2O}(t) + RF_{Others}(t) \tag{12.2}$$

CO_2, N_2O, and CH_4 forcings: The radiative forcing of each of these gases is calculated based on their atmospheric concentrations, as determined by the gaseous cycles module. The formulas are adapted from (Meinshausen et al., 2020), which accounts for overlapping effects among the gases:

$$RF_{CO2}(t) = \left(a' + C_1\sqrt{N(t)}\right) \cdot \ln\frac{C(t)}{C_0} \tag{12.3}$$

$$RF_{N2O}(t) = \left(a_2\sqrt{C(t)} + b_2\sqrt{N(t)} + c_2\sqrt{M(t)} + d_2\right) \cdot \left(\sqrt{N(t)} - \sqrt{N_0}\right) \tag{12.4}$$

$$RF_{CH4}(t) = \left(a_3\sqrt{M(t)} + b_3 \cdot \left(\sqrt{N(t)} + d_3\right)\right) \cdot \left(\sqrt{M(t)} - \sqrt{M_0}\right) \tag{12.5}$$

Where $C(t), N(t), M(t)$ are the atmospheric concentrations of CO_2, N_2O, and CH_4 at time t, and C_0, N_0, M_0 are their pre-industrial values. $a', a_2, b_2, c_2, d_2, a_3, b_3, d_3$ are coefficients which can be found in Table 3 of Meinshausen et al. (2020).

Other forcings: Forcings from halocarbons, aerosols, ozone, and other climate drivers are applied exogenously based on RCP projections. This formulation ensures that radiative forcing responds dynamically to the emissions of the primary greenhouse gases while maintaining consistency with established climate projections for secondary forcing agents.

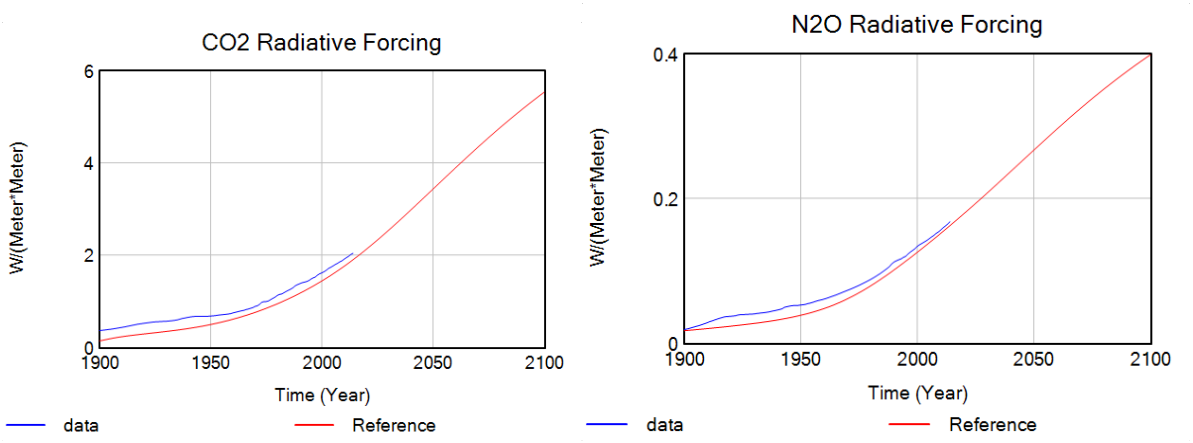

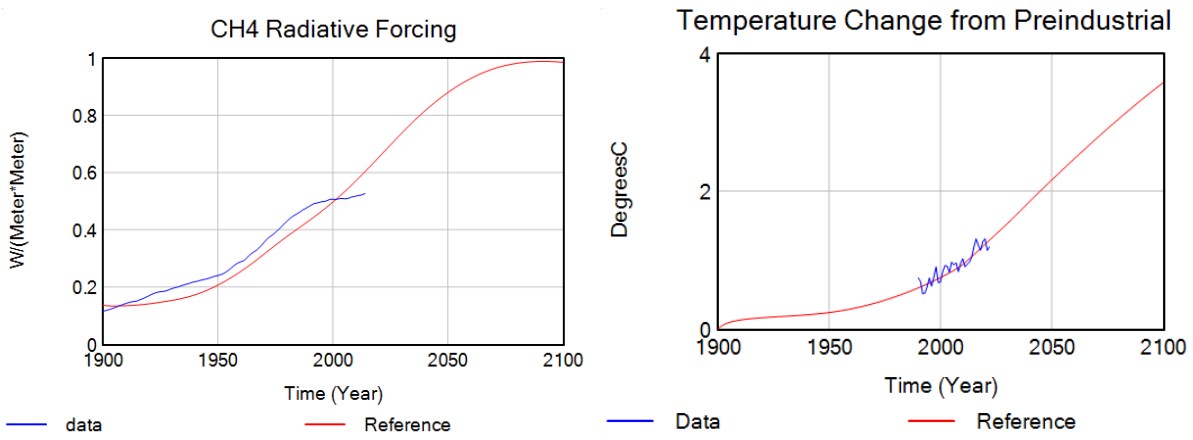

12.2. Feedback cooling

Feedback cooling due to outbound longwave radiation governs the feedback mechanism of the atmosphere and the upper ocean. The rate of cooling is determined by the climate sensitivity—a metric used to characterise the response of the global climate system to a given forcing. It is broadly defined as the equilibrium global mean surface temperature change following a doubling of atmospheric CO_2. This is estimated as 3°C based on IPCC AR4 (Hegerl et al., 2007).

12.3. Heat transfer

The Energy Balance Model in FeliX tracks heat stocks between the atmosphere, the upper ocean, and four layers of the deep ocean. Heat transfer into the deeper ocean layers is modeled as a function of eddy diffusion, which also governs the movement of carbon through the deep ocean. FeliX represents four distinct deep-ocean layers: 100–200 m, 200–700 m, 700–2000 m, and 2000+ m.

13. Wellbeing (Years of Good Life)

We operationalize wellbeing mostly through the novel comprehensive wellbeing indicator YoGL (Years of Good Life), a measure developed by which aims at estimating the remaining years of life an individual can expect to live in a "good" state. By considering the changing characteristics of human populations that reflect the overall wellbeing of society, YoGL is specifically designed to assess the sustainability of long-term development trajectories (Lutz et al., 2021).

YoGL is built on the fundamental assumption that for individuals to experience any quality of life, they must first be alive. However, recognizing that mere survival alone is insufficient to capture wellbeing, YoGL is contingent upon meeting minimum standards of both objectively observable conditions (capable longevity) and subjective life satisfaction. Drawing on earlier works by Desai, Sen, Boltvinik, et al. (1992), the objective conditions measuring "capable longevity" are further divided into three dimensions: being out of poverty, being cognitively enabled, and being physically healthy. To be considered as "good" years in the YoGL calculation, individuals must surpass critical thresholds in all three objective dimensions and report also a minimum level of overall life satisfaction.

To calculate YoGL, we apply the well-established Sullivan method (Sullivan, 1971). It combines data from a regular life table with cross-sectional data on a specific phenomenon of interest, allowing for the quantification of proportions of the population in different states. In the case of YoGL, the state space includes different levels of subjective satisfaction with life, as well as the objectively assessed states of poverty, cognition, and health. The proportions of people in different states are calculated at different ages before they are used as weights for the age-specific life table person years lived, from which life expectancies in different states can be obtained using conventional life table techniques. The formula for calculating YoGL at age x is depicted in Equation 4.1:

$$YoGL_x(t) = \frac{1}{l_x(t)} \sum_{j=x}^{A} \pi_j(t)\, L_j(t) \tag{4.1}$$

$$\pi_{ij}(t) = p_{ij}(t)\, h_{ij}(t)\, e_{ij}(t) \tag{4.2}$$

where l_x stands for number of survivors at age x (beginning of interval j), L_j stands for the person-years lived in the age interval j and π_j stands for the prevalence of the state of interest in the age interval j, i.e., age-specific proportions of the population that are not living in poverty, are (at least) in basic physical and cognitive health, and report positive life satisfaction. Finally, A denotes the last (open) age group in the life table (i.e., 100+).

While π_j should be ideally derived from objectively assessed individual characteristics as measured in representative cross-sectional surveys (Lutz et al., 2021), such an approach is not possible to implement in a global macro model such as FeliX. Therefore, the different dimensions of YoGL are estimated as endogenous variables as will be explained further in the following sub-sections. π_j is then calculated as the product of age and gender specific proportions of people out of poverty (p_{ij}), people meeting or exceeding basic health (h_{ij}), and people meeting or exceeding basic cognitive functioning (e_{ij}) as Equation 4.2 shows. Given the lack of data on subjective life satisfaction on the global level, we exclude it from the formulation of the dynamic prevalence rates.

13.1. Being out of poverty

The age- and gender-specific proportion of people out of poverty *($p_{i,j}$)* is directly derived from the poverty rate $PR_{i,j}$ (as detailed in Section 3.3), following Equation 4.3:

$$p_{ij}(t) = 1 - PR_{ij}(t) \tag{4.3}$$

13.2. Basic physical health

The proportion of people with basic physical health *(h)* is estimated using the ratio of health-adjusted life expectancy *(HALE*) to life expectancy *(LE)*, for each gender *i* and age group *j*, as shown in Equation 4.4.

$$h_{ij}(t) = \frac{HALE_{ij}(t)}{LE_{ij}(t)} \tag{4.4}$$

LE_{ij} is derived from *life expectancy at birth (LE)* as described in Section 2.3. $HALE_{ij}$ is derived from *healthy life expectancy at birth ($HALE_i$)* with coefficients (ρ_j) estimated from historical data (Equation 4.5). The ratio of *HALE* at any age to *HALE at birth* has been almost constant over time, as shown by historical data obtained from the Global Burden of Disease (GBD) data for the years 1990-2020 (A. D. Lopez & Murray, 1998) and depicted in Figure 40. Therefore, the age coefficients of *HALE* are assumed to remain constant in the future, too, and are set equal to the mean of the historical values as shown in Equation 4.6.

$$HALE_{ij}(t) = HALE_i(t) \times \rho_j \tag{4.5}$$

$$\rho_j = \frac{\sum_{t=1990}^{t=2019} \rho_j(t)}{30} \tag{4.6}$$

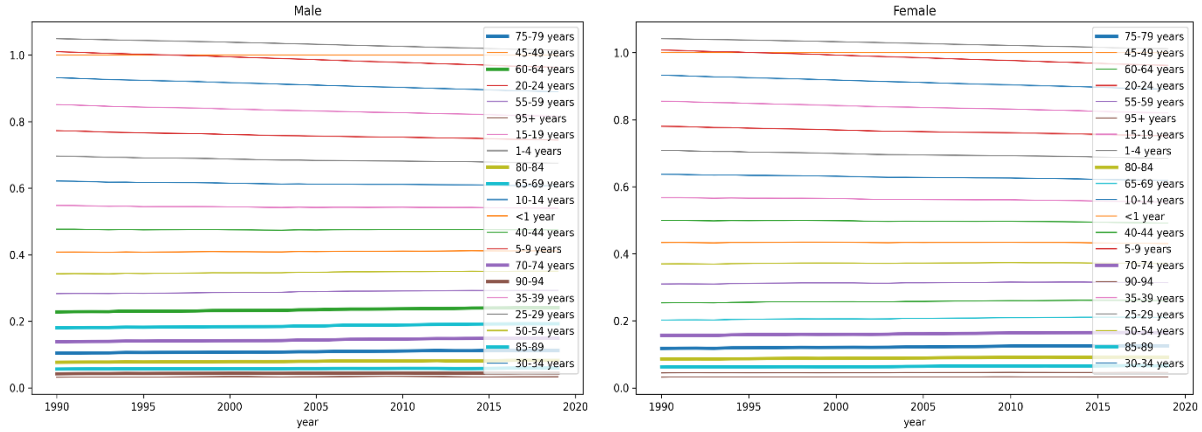

Figure 40: Ratio of Healthy Life Expectancy to Healthy Life Expectancy at Birth for each 5-year age group and over time for males (a) and females (b)

HALE at birth is formulated as a function of *GDP per capita* and *daily food supply per capita*, especially from sugar and oil crops. This choice was motivated by the recent findings of Aanegola et al. (2022), who analyzed the drivers of *HALE* based on panel data from 30 European countries using machine learning algorithms designed to infer causality (causal forests). Their findings show that the most important factors affecting HALE are gross national income (GNI) and body mass index (BMI), followed by educational expenditure. This strong relationship between HALE, GDP and BMI can be found in global data too, as demonstrated in Figure 41. In FeliX, we take the GWP per capita as a proxy for GNI, and we approximate BMI by the caloric supply per person. BMI has increased over time depending on food supply, as Figure 42 shows. If BMI continues to increase as a result of food supply, the HALE-food relationship would be reversed, though, due to adverse health effects observed in the overweight population. We derive this non-linear relationship between HALE and food supply from the panel data across 204 countries over years 1990-2019, using *locally estimated scatter plot smoothing*, as demonstrated in Figure 43.

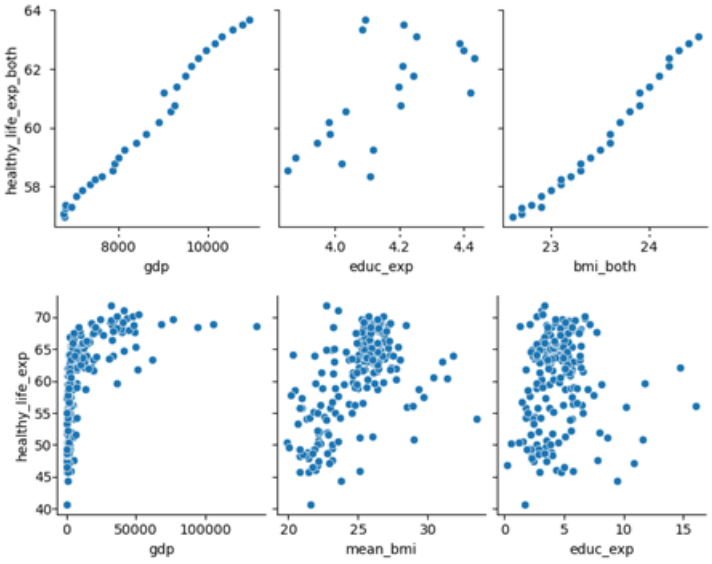

Figure 41: Relationship between average healthy life expectancy at birth (healthy_life_exp) and GDP per capita (gdp), average body mass index (bmi) and educational expenditure as a percentage of GDP (educ_exp). The top row shows the relationships over time, where each data point refers to the global average value in a year between 1990 and 2019. The bottom row shows the relationships across countries, where each data point refers to the values per country averaged over time. The data for healthy life expectancy and BMI is obtained from the Global Burden of Disease dataset. The GDP and educational expenditure data is obtained from the World Bank statistics.

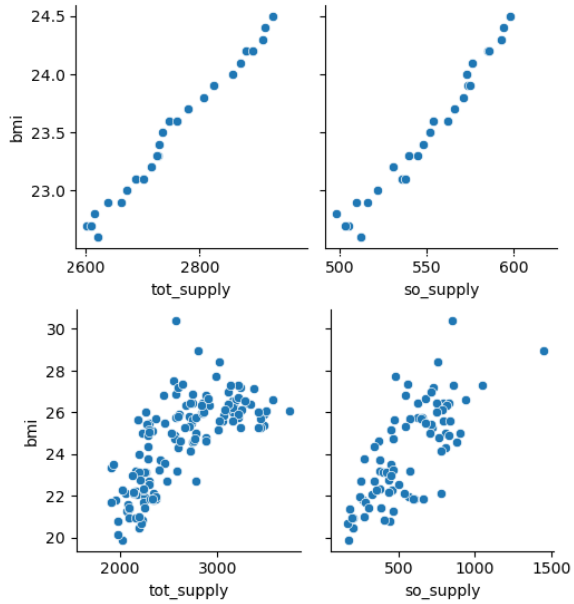

Figure 42: Relationship between body mass index (bmi) and total food supply (tot_supply) and food supply from sugar and oil crops (so_supply) as calories per person per day. The top row shows the relationships over time, where each data point refers to the global average value in a year between 1990 and 2019. The bottom row shows the relationships across countries, where each data point refers to the values per country averaged over time. The data for BMI is obtained from the Global Burden of Disease dataset. The food supply data is from the FAO food balance sheets.

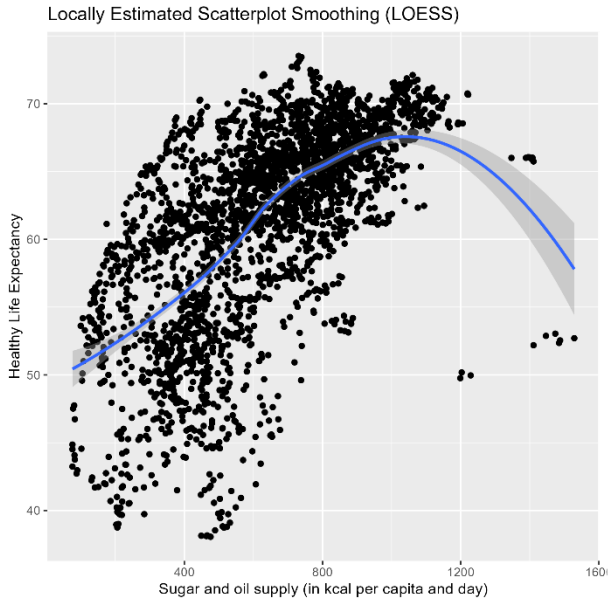

Figure 43: Inverted U-shaped relationship between healthy life expectancy and sugar and oil supply

Therefore, we formulated HALE at birth (*HALE*$_i$) as in Equation 4.7, where the global average HALE for males and females in year 2000 is the reference value, and the impact of food supply and GDP per capita are multipliers over this reference value. The impact of food supply on HALE is formulated as a lookup function (*f*), replicating the approximation in Figure 43, yet normalized on both the x and y axes according to the actual value in year 2000 (Equation 4.8). Considering the logarithmic pattern of relationship observed in Figure 41 between HALE and GDP per capita, we use the exponential function form denoted in Equation 4.9 to define the impact of GDP on HALE. The parameters *a* and *b* are calibrated according to the historical values of HALE at

birth for both males and females in period 1990-2019, after setting the impact of food as defined in Equation 4.8. The resulting function form for the effect of GDP is shown in Figure 44. It is important to note that HALE-GDP relationship is calibrated in an earlier version of the model where the GDP outcome was different, and it will be adjusted in the upcoming revision.

$$HALE_i(t) = HALE_i^{2000} \times Impact_{hale}^{gdp}(t) \times Impact_{hale}^{food}(t) \tag{4.7}$$

$$Impact_{hale}^{food}(t) = f\left(\frac{Food_{oil\&sugar}(t)}{Food_{oil\&sugar}(2000)}\right) \tag{4.8}$$

$$Impact_{hale}^{gdp}(t) = a \times \left(GWP\ per\ Capita^{*}(t)\right)^{b} \tag{4.9}$$

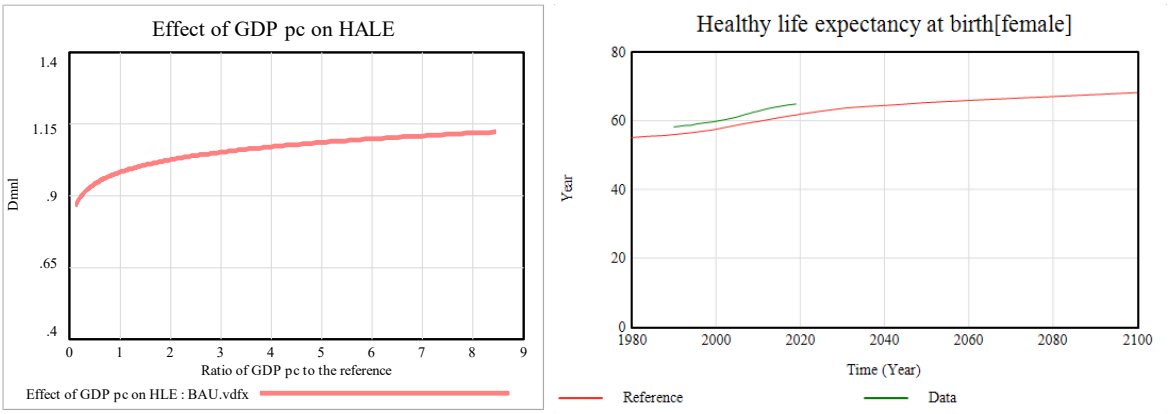

(a) (b)

Figure 44: (a) The impact of GDP on healthy life expectancy and (b) the simulation results for healthy life expectancy at birth of females (green) compared to the historical values (pink) obtained from GBD dataset.

13.3.Being cognitively enabled

In the original definition of YoGL, Lutz et al. use the results of well-established numeracy and memory tests recorded in a multi-national survey. In this global dynamic modelling setting, we use the fraction of population with minimum primary education as a proxy for the cognition component of YoGL. Therefore, the prevalence of cognition component of YoGL is formulated as the sum of primary, secondary and tertiary education graduates (See section 2.4), divided by the population for each age and gender, as denoted in Equation 4.10.

$$e_{ij}(t) = \frac{PEG_{ij}(t) + SEG_{ij}(t) + TEG_{ij}(t)}{Population_{ij}(t)} \tag{4.10}$$

14. Baseline Scenarios

Three baseline scenarios outline plausible future pathways aligned with the Shared Socioeconomic Pathways (SSPs) narratives on energy, land use, food, and climate policy (Riahi et al., 2017), following the calibration of the FeliX model to these narratives as described in Moallemi et al. (2022). These narratives inform the parameter assumptions of each baseline scenario. Specifically, the scenarios represent:

- a neutral "business-as-usual" (reference) future,
- a sustainable "green recovery" (optimistic) future, and

- an unsustainable "fragmented world" (pessimistic) future, corresponding to the SSP2, SSP1, and SSP3 trajectories, respectively.

Radiative forcing from non-CO_2 gases, exogenous to FeliX, is assumed to follow RCP 4.5, RCP 2.6, and RCP 6.0 for the reference, optimistic, and pessimistic scenarios, respectively. The key assumptions for each scenario are summarized below.

- **Reference scenario (SSP2 – Business-As-Usual):**

  This scenario adopts the SSP2 storyline for population, economic development, and policy, as implemented in Moallemi et al. (2022). Population growth, fertility, and life expectancy grow at moderate rates. Demographic indicators follow SSP2 projections, with one modification: climate-related mortality is included in FeliX, leading to lower life expectancy than SSP2 projections. These impacts are modeled using the temperature- and education-dependent estimates of Bressler et al. (2021). Economic growth is moderate, following historical patterns. However, unlike the original SSP2 projections, GDP per capita is endogenously determined in FeliX; this is done based on labor force, capital investment, and technological progress, while incorporating climate damages to economic output using the empirical damage function of Burke et al. (2015) which accounts for long-term impacts of a given temperature increase, pooled across all regions and income levels.

- **Optimistic scenario (SSP1 – Green Recovery):**

  This scenario reflects a sustainable development pathway emphasizing education, human capital investment, and fast technological advancement. Fertility rates are lower, and healthier lifestyles enable increased life expectancy, consistent with the SSP1 narrative. Climate impacts on mortality and economic output are included, as in the reference scenario, with the magnitude depending on the scenario's own temperature projections modelled endogenously in FeliX. Low challenges to mitigation and adaptation are assumed, and non-energy technological progress is set to be 50% higher by 2100 than in the reference case, representing spillover effects from accelerated technological change towards a green economy.

- **Pessimistic scenario (SSP3 – Fragmented World):**

  This pathway depicts a divided world with regional rivalry, characterized by high fertility, low life expectancy, and weak economic growth. Climate impacts on mortality and the economy are again incorporated as in the reference case, with outcomes depending on the scenario-specific temperature trajectory. Here, technological progress in the non-energy sector is assumed to be 50% lower by 2100 relative to the reference scenario, reflecting a sluggish pace of innovation in a persistently fossil-dependent world facing stronger climate damages (Donadelli et al., 2021).

To calibrate the demographic variables to the SSPs, we use the population projections updated in 2023 as provided by Wittgenstein Center for Demography and Global Human Capital (Wittgenstein Centre, 2023). For all other variables, we use the SSP baseline projections produced by the integrated assessment modelling community and published in the SSP scenario database (Huppmann et al., 2018). Appendix I lists parameter values of the FeliX model calibrated to each narrative, as described in Moallemi et al. (2022).

Figure 45 shows the dynamic trajectory of global population in the three baseline scenarios and the corresponding SSPs. The *Reference* scenario results in higher population values than SSP2, so does the *Optimistic* scenario but only marginally between 2030 and 2060. This is attributed to fertility rates being higher

than their SSP projection due to lower economic growth in the presence of climate damages and due to lower education embedded in the scenario narrative. Still, this means that the direct impact of climate on mortality is not stronger than the economic impact in these two scenarios. In the *Pessimistic* scenario, FeliX projections are lower than SSP3, due to the strong direct climate impact on mortality, and indirect effects through much lower economic growth. Similarly, Figure 46 shows the educational attainment differences between the baseline scenarios and the SSP2 projections, specifically for the global tertiary education graduates. In all three scenarios, FeliX projections are lower than the SSP ones, due to lower economic growth (Figure 47) and the sensitivity of tertiary education enrolment to GWP per capita (Figure 16a).

The three baseline scenarios deviate significantly from their corresponding SSPs in terms of projections of global economic output (GWP) as shown in Figure 47 due to the strong climate damage assumption in the former. Figure 48 shows the GWP projections in the three baseline scenarios without climate damages, where the difference from the SSPs is smaller, with remaining differences being attributed to the endogenous calculation of economic output in FeliX with different factors. The temperature projections in the three scenarios underlying the economic impacts of climate change are shown in Figure 49.

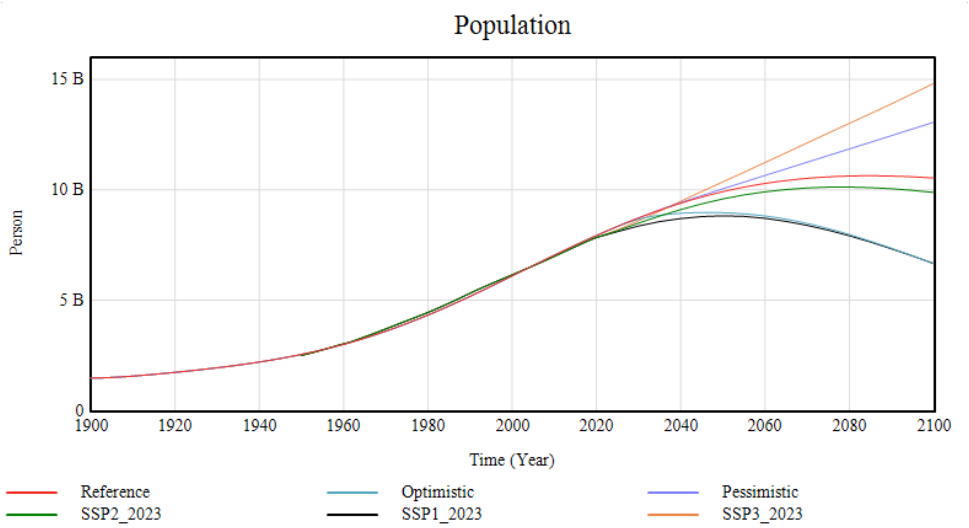

Figure 45: Global population over time in the three baseline scenarios generated by FeliX and in the corresponding SSP projections

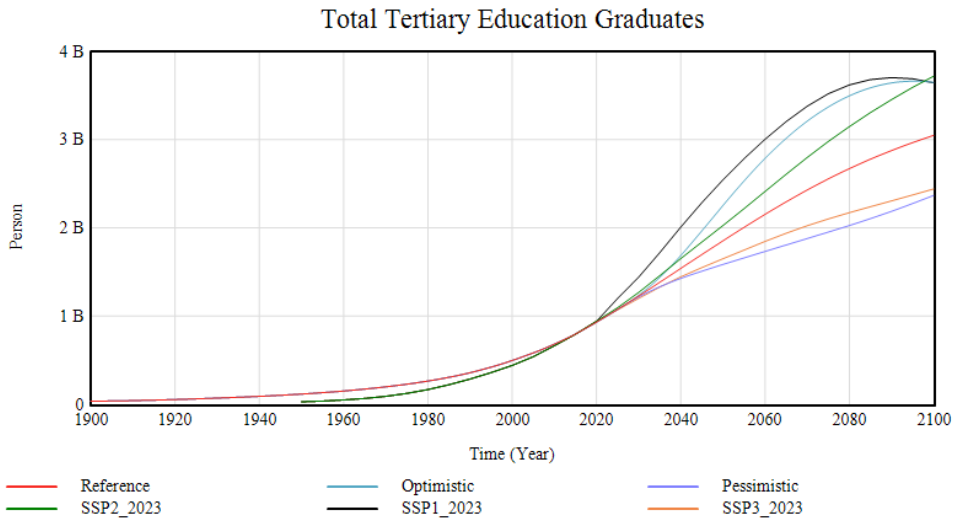

Figure 46: Global tertiary education graduates in the three baseline scenarios generated by FeliX and in the corresponding SSP projections

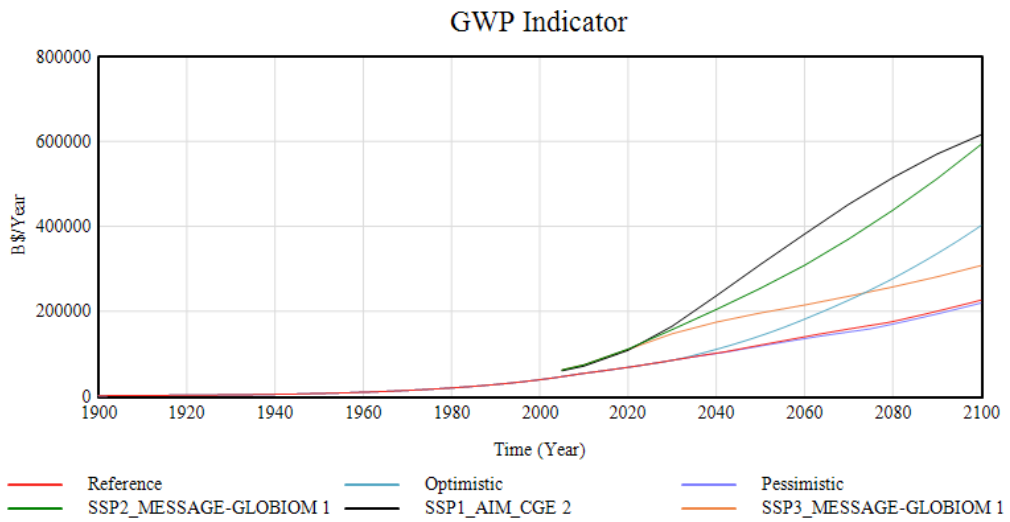

Figure 47: Global GDP (gross world product) in the three baseline scenarios generated by FeliX and in the corresponding SSP projections

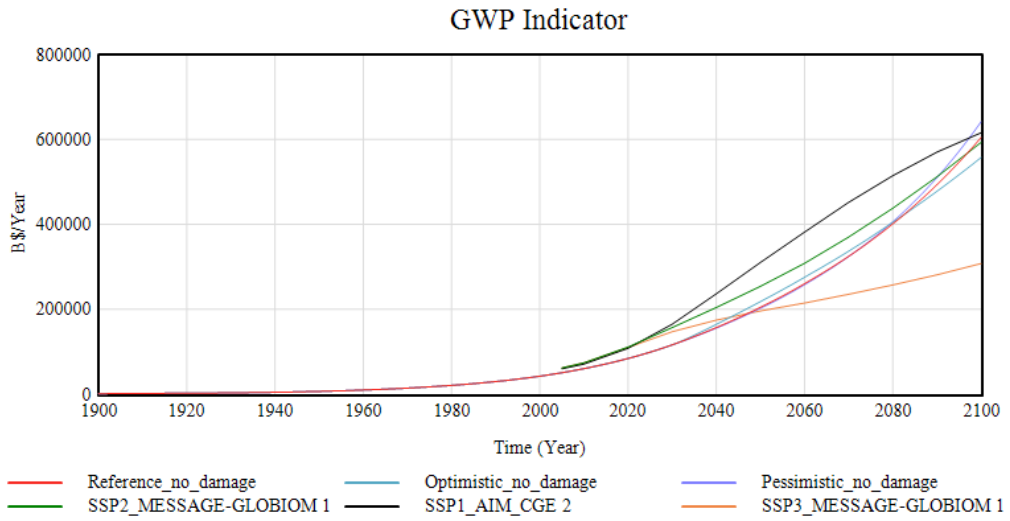

Figure 48: Global GDP (gross world product) in the three baseline scenarios generated by FeliX without climate damages taken into account and in the corresponding SSP projections

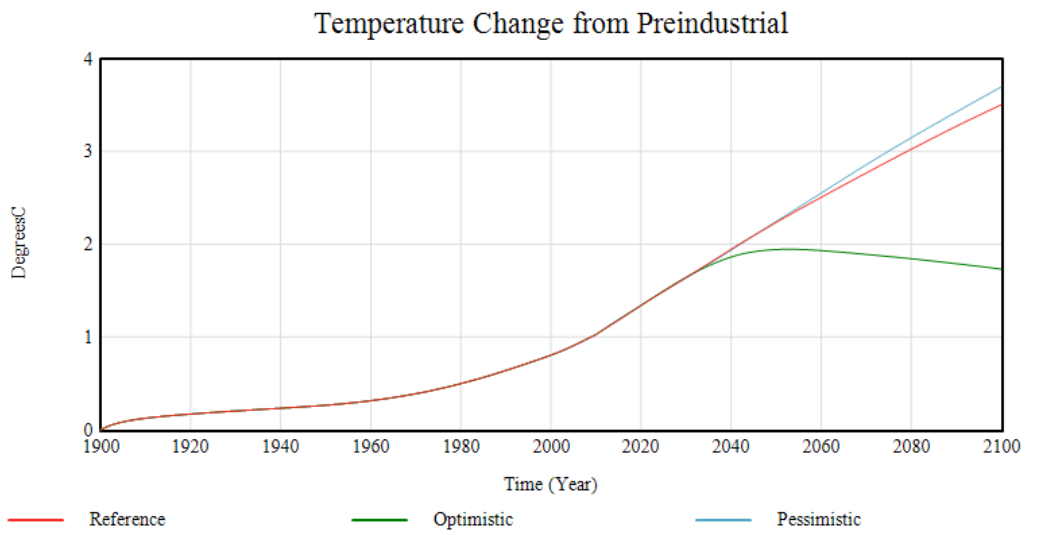

Figure 49: Global mean temperature change from preindustrial times in the three baseline scenarios generated by FeliX

Figure 50 - Figure 55 show the comparison of the FeliX projections in the *Reference* scenario to SSP2 projections of various integrated assessment models used in the IPCC assessments. FeliX projects *Total Radiative Forcing* within the range of projections created by other models, except the last two decades of the century, where the FeliX projection declines (Figure 50). This can be attributed to the decline in the CO_2 emissions in the FeliX output in those decades (Figure 51), which is otherwise around 5 Gt/yr higher than the SSP2 projections. Such higher emission projections in the FeliX compared to the other models is due to the differences in the agriculture and land use emissions, amongst other factors. As Figure 52 and Figure 53 show, FeliX projections for the agricultural production from non-energy crops fall within the range of projections by other models, yet the livestock production is on the higher end of that range in the FeliX model, similar to the projections by the REMIND-MAgPIE model. Considering the coal and wind energy production as the two indicators from the energy sector, FeliX projections similarly fall within the range of projections by other models (Figure 54 and Figure 55), with coal production already showing a decline in SSP2 towards the end of the century as in the WITCH-GLOBIOM model.

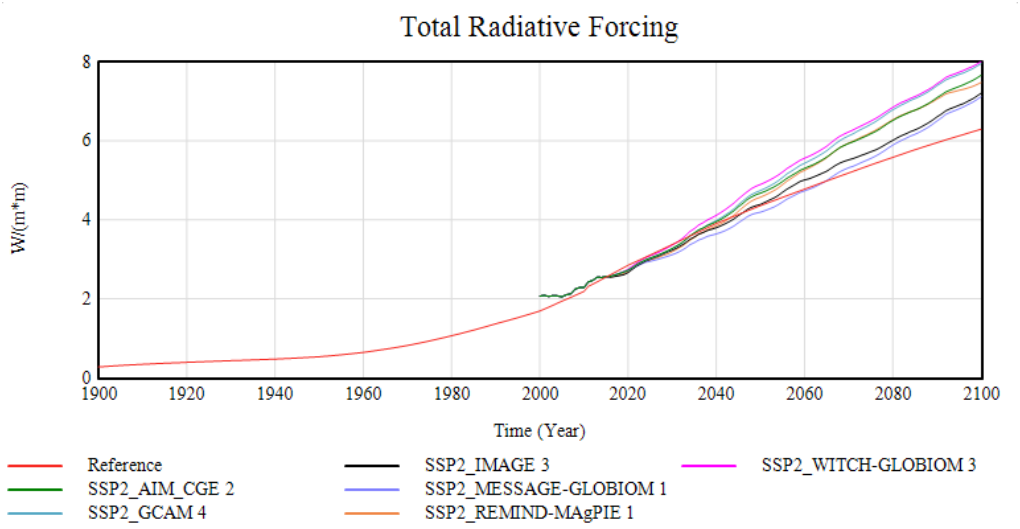

Figure 50:Total radiative forcing in the Reference scenario generated by FeliX and in the SSP2 projections created by six other integrated assessment models

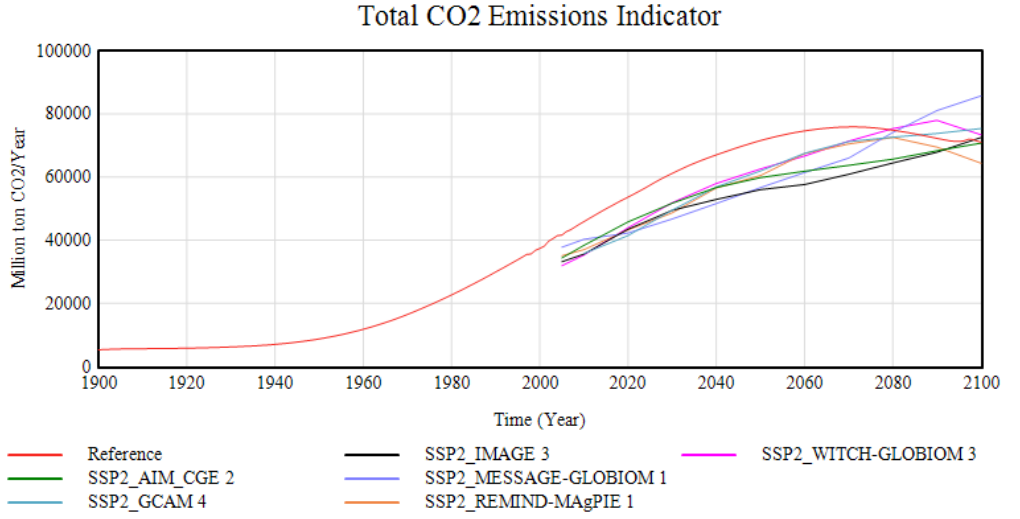

Figure 51: Total global CO_2 emissions in the Reference scenario generated by FeliX and in the SSP2 projections created by six other integrated assessment models

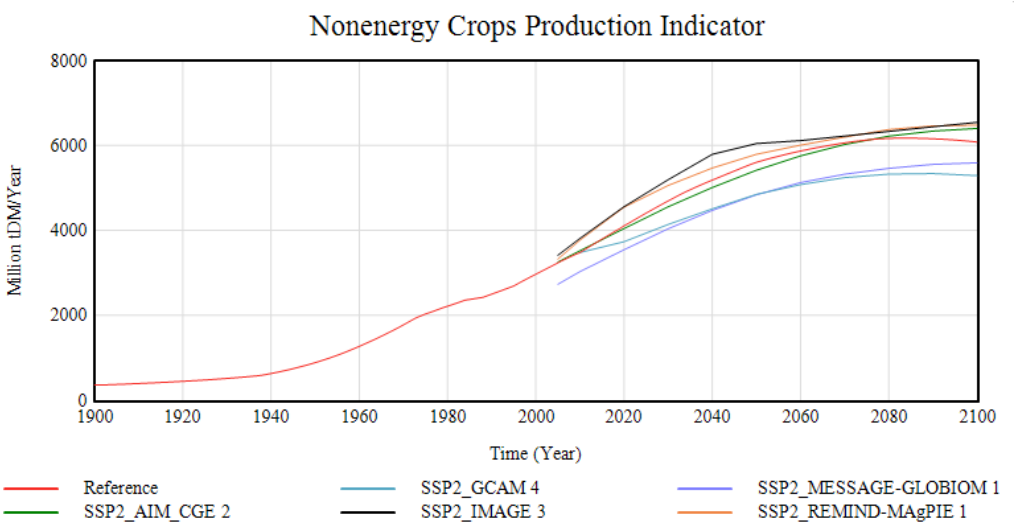

Figure 52: Total agricultural crop production from non-energy crops in the Reference scenario generated by FeliX and in the SSP2 projections created by six other integrated assessment models

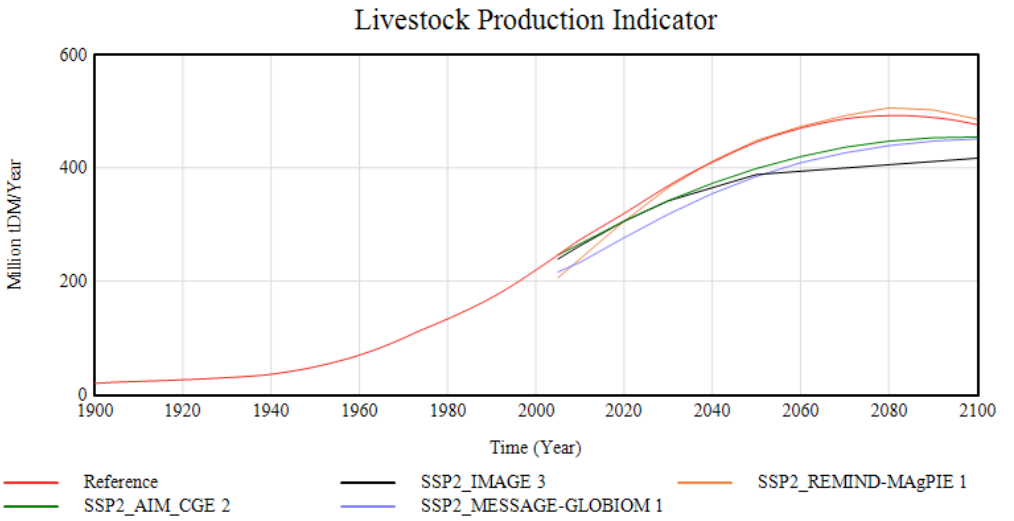

Figure 53: Total agricultural production from livestock in the Reference scenario generated by FeliX and in the SSP2 projections created by six other integrated assessment models

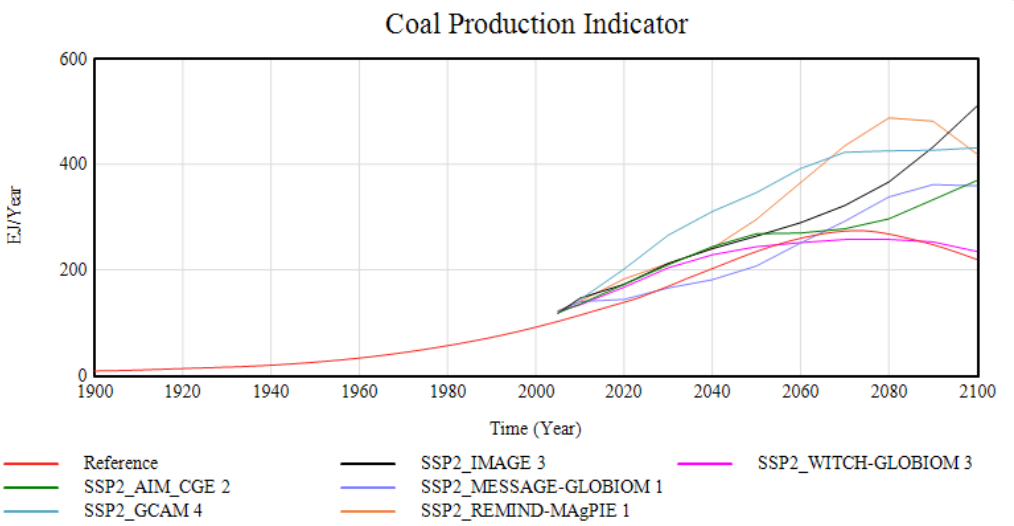

Figure 54: Global primary energy production from coal in the Reference scenario generated by FeliX and in the SSP2 projections created by six other integrated assessment models

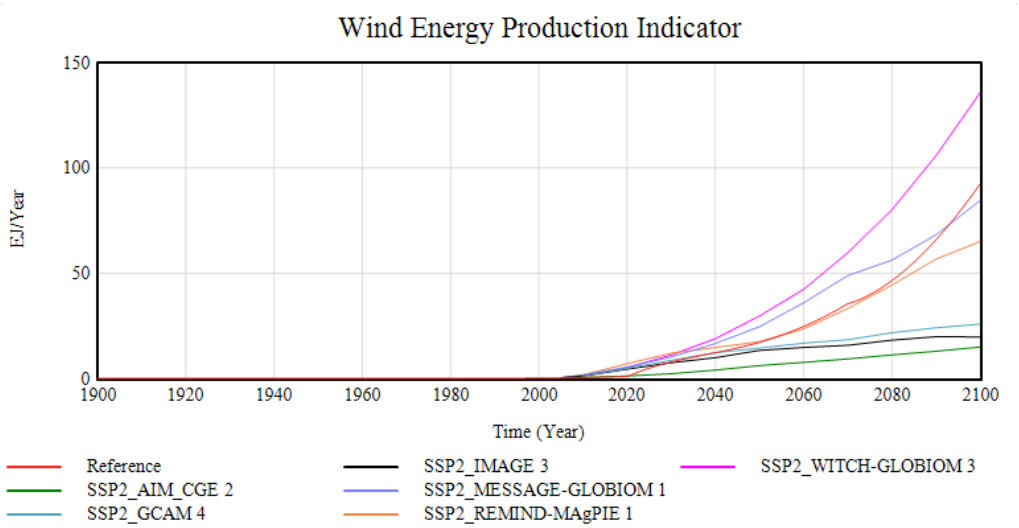

Figure 55: Global primary energy production from wind in the Reference scenario generated by FeliX and in the SSP2 projections created by six other integrated assessment models

15. Regional FeliX

Th global FeliX model does not facilitate fine-scale analysis of socioeconomic-environmental dynamics that take geographic, socioeconomic and cultural differences into account. To address this limitation, we regionalized the model to cover 5 distinct regions. Three main challenges are encountered when regionalizing such a feedback-rich system dynamics model: 1) The full connections and feedback among variables from different modules make the calibration processes involve multi parameters and/or dimensions and thus time-consuming; 2) Inter-regional trade should be considered and modelled for products especially fossil fuel products; 3) A large dataset covering regional even national historic data of key variables is requested for model validation, which involves collecting, cleaning, and processing of data from different data sources.

This section documents the regionalization procedures of FeliX (denoted as FeliX_R5). We break down the world into five regions according to United Nations' regional classifications (UN, 2024), that is, African States (Africa), Asia-Pacific States (AsiaPacific), Eastern European States (EastEu), Latin American and Caribbean States (LAC), and Western European and other States including the United States, Canada, Australia, and New Zealand (WestEu_Dev). The motivation for choosing five regions was to capture main geographic and socioeconomic differences without extending to the detail of geographically more heterogeneous models. Each regionalized module follows the global structure and associated variables at the regional scale are calibrated according to historical data of each region.

The first step is to create a subscript variable (index) *Regions* with five values according to the regional classification, representing the regional dimension of the FeliX model. As such, key variables, such as population, gross domestic production (GDP) per capita, oil demand, etc., will have an extra dimension after the regionalization. Seven modules (Table 5) are fully regionalized in the second version of regionalized FeliX, including population, education, economy, energy, land use, fertilizer use, and biodiversity. The water module is partly regionalized with regionalized water demand by three sectors. The climate module and carbon cycle module are kept globally (Figure 1). The following sub-sections describe the detailed regionalization procedures according to the aforementioned three main challenges.

Table 5: The geographical scales of key variables in FeliX_R5 version 2.0

Module	Geographical scale

	Global	Inter-regional	Intra-regional
Population			Population dynamics across age and gender; Life expectancies.
Education			Enrollment and graduation rates; Labour force.
Economy			Capital accumulation; Gross domestic product (gdp).
Energy		Trade of fossil fuels	Fossil fuel extraction; Investment; Technology advancements; Energy production; Market shares; Energy demands
Diet Change	Diet population shifts; Caloric demand change.		
Fertilizer Use			Nitrogen and phosphorus cycles; Fertilizer consumption; Yields.
Land Use		Trade of food categories	Land supply; Land use change; Land demand; Food demand; Agricultural yield.
Biodiversity			Species abundance dynamics.
Water	Water balance.		Water demand.
Carbon Cycle	Carbon accumulation and transfer rate in deep ocean.		Emissions from fossil fuels.
Climate	Heat transfer in atmosphere, upper and deep ocean.		

15.1. Adding an extra dimension for key parameters

This section describes the regionalization of the population module as an example to demonstrate how the regionalization process works.

As described in the section Population, population is modeled based on dynamic mechanisms of population development and population ageing in the five specified regions. FeliX didn't take migration into account when modelling regional population changes, and thus the population component stands alone at the regional dimension.

The ageing chain shown in Figure 3 can still represent population dynamics through age cohorts at the regional level. Population of each gender and age interval in each region ($Pop_{region,i,j}$) accumulates by birth rate ($Birth_{region,i,j}$), death rate ($Death_{region,i,j}$), and maturation rate ($Matur_{region,i,j}$) by gender (i) and age (j) in each region.

$$\frac{dPopulation_{region,i,j}(t)}{dt} = \begin{cases} Birth_{region,i}(t) - Maturation_{region,i,j}(t) - Death_{region,i,j}(t);\ if\ j = \text{'0-4'} \\ Maturation_{region,i,j-1}(t) - Maturation_{region,i,j}(t) - Death_{region,i,j}(t);\ if\ \text{'5-9'} < j < \text{'95-99'} \\ Matur_{region,i,j-1}(t) - Death_{region,i,j}(t);\ if\ j = \text{'100+'} \end{cases} \quad (14.1)$$

The birth rate (Equation 2.3) is modified as,

$$Birth_{region,i}(t) = g_{region,i} \times \frac{\sum_{j='15\text{-}19'}^{'45\text{-}49'} Population_{region,female,j}(t) \times ASFR_{region,j}(t)}{Age\ interval\ duration} \quad (14.2)$$

$$ASFR_{region,j}(t) = f_j^{asfr}(TotalFertility_{region}(t)) \quad (14.3)$$

$TotalFertility_{region}$ represents the number of births per woman at reproductive ages (between 15 and 50) in each region. It considers the effects of education ($Impact^{Education}_{Fertility,region}$) and wealth on fertility ($Impact^{GDP}_{Fertility,region}$).

$$TotalFertility_{region}(t) = NormalFertility_{region} \times Impact^{Education}_{Fertility,region}(t) \times Impact^{GDP}_{Fertility,region}(t) \quad (14.4)$$

where $NormalFertility_{region}$ is the reference value of fertility, equal to the historical value of each region in the year 2000. This formulation also prevents a strong assumption on the monotonic dependence of fertility solely on education or solely on economic output. Like global setting, $Impact^{Education}_{Fertility,region}$ and $Impact^{GDP}_{Fertility,region}$ at the regional level are also formulated as logistic functions based on mean years of schooling and $GDP\ per\ Cap_{region}$, respectively, following the observed relationship shown in in each region.

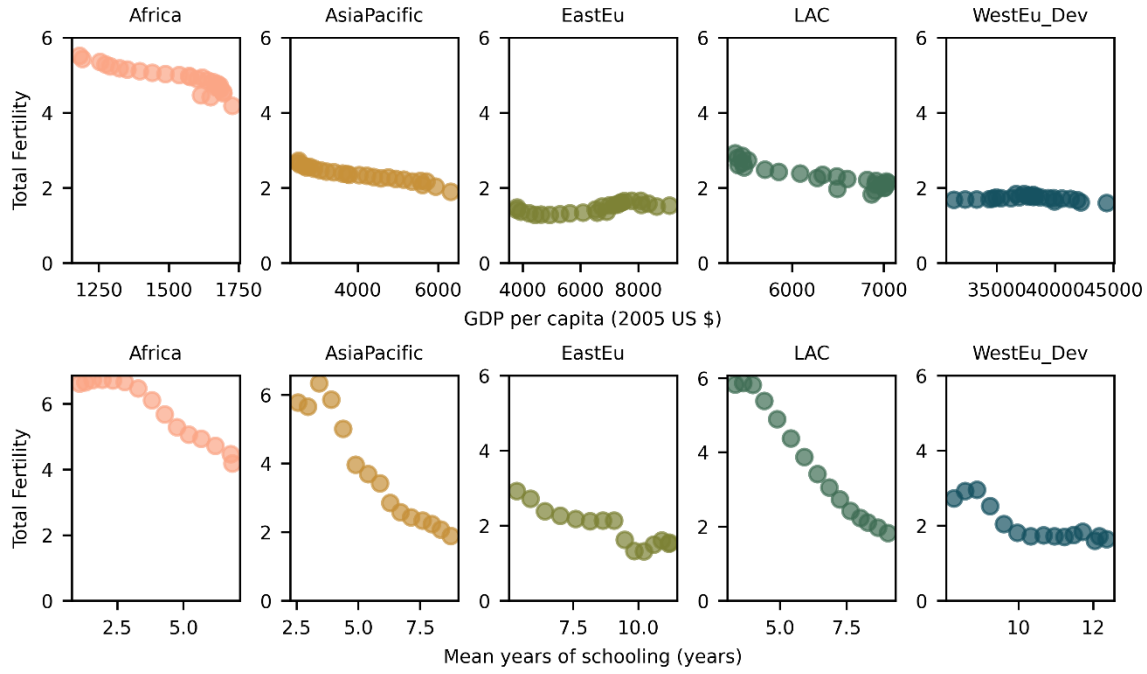

Figure 56: Observed relationship between total fertility rates and two drivers. The upper row shows the relationships between average total fertility rates (births per woman at the reproductive age) and GDP per capita between the years 1995–2023 in each region. The lower row presents relationships between average total fertility rates and mean years of schooling between the years 1950–2023 in each region.

Death rate ($Death_{region,gender,age}$) in each region is formulated as a fraction of the population of each group, following the global FeliX.

$$Death_{region,i,j}(t) = Population_{region,i,j}(t) \times M_{region,i,j}(t) \quad (14.5)$$

where $M_{region,i,j}$ is the mortality fraction by gender and age cohort in each region. $M_{region,i,j}$ is also calculated as a logistic function of regional average life expectancy at birth (LE_{region}), following the observed relationships shown in Figure 57 in each region.

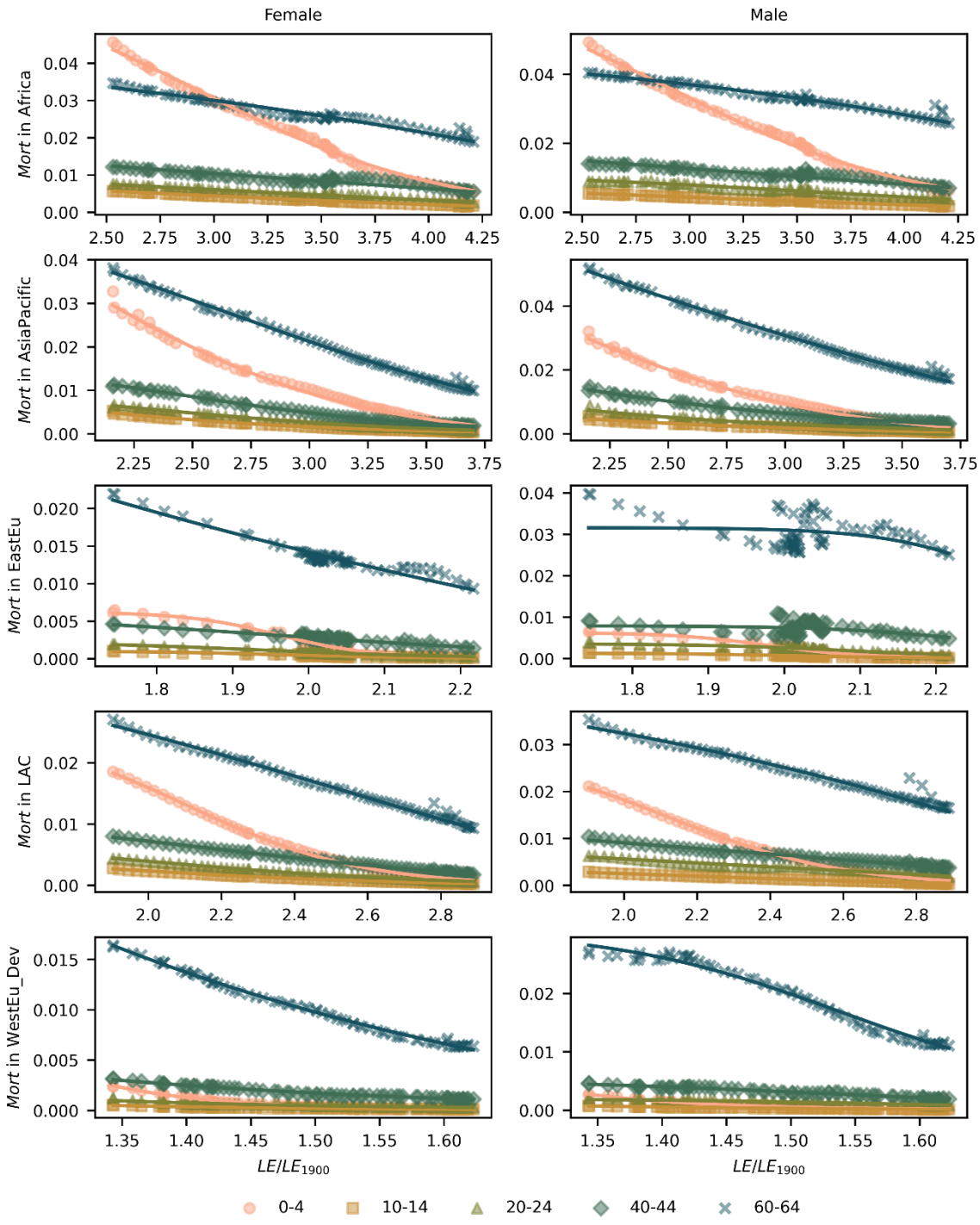

Figure 57: Observed relationship between mortality fractions (M) and life expectancy at birth (LE) between 1950 and 2022. Dots represent historic data. Lines represent the modeled values.

15.2. Modeling inter-regional trade

Trade becomes critically important in a regionalized model setting (Uno, 2002). In a global model, the assumption of perfect self-sufficiency (i.e., global production equals global demand) neglects the need to model trade flows. However, in a regionalized model setting, this assumption becomes unrealistic given high heterogeneity between regions in terms of resource endowments, technological capacity, environmental constraints, etc. Inter-regional trade plays a key role in benefiting the exporting regions from local advantages and also meeting local demands of the importing regions if there is a deficit between regional production and

demand (Dollar & Kraay, 2003). In this context, inter-regional trade must be explicitly modeled to capture the complex interactions and dependencies among regions. This also allows modelers to trace environmental responsibilities along the supply chain and quantify how one region's policy may influence economic outcomes or emissions in others (Peters & Hertwich, 2008; Wiedmann & Lenzen, 2018).

We develop an import-based trade mechanism to model the trade of fossil fuels and food products among the five regions. The other three renewable energy sources (i.e., biomass, solar, and wind) are assumed to be self-sufficient for each region. Figure 58 presents the trade mechanism of pasture meat (PasMeat), as a representative of all traded products, and the links between trade module and other modules. We use an Armington style to distinguish domestic goods from imported ones. The Armington approach assumes products are differentiated by source region, and consumers treat goods produced in different regions as imperfect substitutes (Armington, 1969). As such, imports of pasture meat in a region are from a single global pool that draws from all regions, and are also governed by a logit sharing function.

$$S_{rs} = \frac{\alpha_{rs} Price_r^{-\delta}}{\sum_k \alpha_{ks} Price_k^{-\delta}} \tag{15.6}$$

where S_{rs} is the share of region *r* in total import of region *s*; α_{rs} is the preference parameter for pasture meat from region *r* in region *s*; $Price_r$ is the price of pasture meat in region *r*; δ is the elasticity of substitution. The amount of pasture meat, either going into the international market for export or needed to be imported from international market, depending on the gaps between local demand and production of pasture meat. It indicates that the re-export of pasture meat is not taken into account in the trade mechanism. The modelling of trade starts from diet-based demands of pasture meat in regions. Since the dietary module has not been regionalized, we simply downscale global pasture meat demand into regional level based on population. Inter-regional import and export to meet the demand, based on the potential production rate, which links to land use, and yield in the regionalized land use module. Actual production of pasture meat in each region is calibrated to historic data at the regional level. The final trade matrix meets both the production and demand of pasture meat in each region.

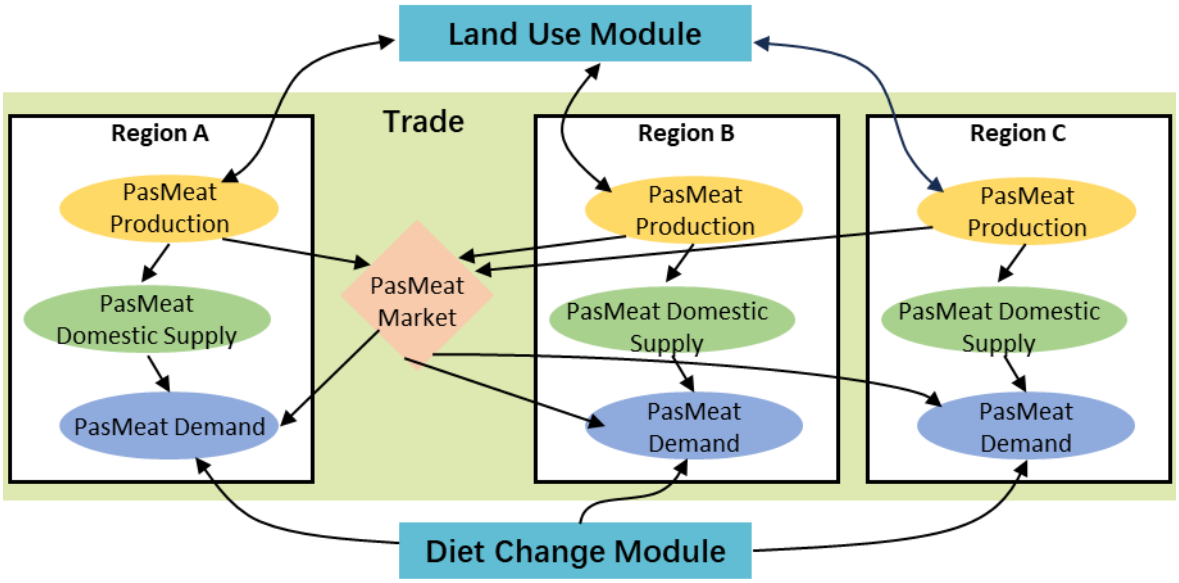

Figure 58: Import-based trade mechanism for a representative fossil fuel (i.e., oil) and three representative regions.

15.3. Historic data processing and data sources

This section gives an overview of the historical data of key variables in the regionalized FeliX, and associated data sources. Historical data exactly for the five regions specified in FeliX is rare. We collected most of the historical data at the national level and used concordances between individual country/economy and region to aggregate and/or process raw data into cleaned and harmonized ones at the regional level. This step requests substantial efforts. We use python to process all the data. Python scripts for data collection, cleaning, and processing can be found in the github repository of felix model, https://github.com/iiasa/Felix-Model.

Most of the demographic data are from United Nations Population Division (UNPD, United Nations (2022) and Wittgenstein Centre for Demography and Global Human Capital (named as 'Wittgenstein Centre' from hereon, Wittgenstein Centre, 2020). We collected national population by 5-year age group and by sex from UNPD and aggregated into regional population data at the same dimensions. Total birth rates and total death rates at the national level are also collected from UNPD as total number of live by sex and total deaths by sex, respectively, and summed up into the regional level. Processing fertility rate data (including total fertility rates, and age-specific fertility rates), mortality fraction data, and life expectancy at birth data requests additional work because they are expressed as fractions. Taking age-specific fertility rates as an example:

1) we first collect fertility rates by age of mother with 5-year interval, and female population by 5-year age groups at the national level from UNPD;

2) we multiply fertility rates by a certain 5-year age group with female population at the same age group in each country/economy as total birth rates by mothers at that age group for the country/economy;

3) we sum up total birth rates by mothers from the certain 5-year age group and female population from the certain 5-year age group into the regional level, and divide the former by the later as age-specific fertility rate of that age group by region.

$$ASFR_{region,j} = \frac{\sum_{country} ASFR_{country \in region,j} \times Population_{country \in region,female,j}}{\sum_{country \in region} Population_{country \in region,female,j}} \quad (15.7)$$

where j is the 5-year age group (e.g., '15–19') between 15 and 49.

In addition to UNPD, Wittgenstein Centre is the other data source that provides comprehensive demographic data, especially for education-related data. We collect national population by sex, by 5-year age groups and by level of educational attainment from Wittgenstein Centre. Four levels of educational attainment are distinguished in FeliX (see **Educational attainment and mean years of schooling**), that is, no education, primary education, secondary education, and tertiary education. We use regional concordances to sum up national population by sex, by 5-year age groups and by level of educational attainment into the regional level with same dimensions. FeliX also includes an important variable named 'mean years of schooling' in delineating the effect of education on fertility rates, life expectancy, and demand-side needs in other modules. Mean years of schooling is formulated as the weighted average of the duration of each education level (Equation 2.24). The weights are determined by the total number of graduates for the respective education level relative to the population aged 15 and above. Raw mean years of schooling at the national level is also from Wittgenstein Centre. We use the same calculation procedure of age-specific fertility rate to calculate mean years of schooling at the regional level.

Economic data is mainly from the World Bank (The World Bank, 2023), and Groningen Growth and Development Centre (Feenstra et al., 2015). We collect GDP, GDP per capita, share of consumption of fixed capital formation in GDP, and share of gross fixed capital formation in GDP, all at the national level, from The World Bank. The latter three are also expressed as fractions. As such, we use the same calculation procedure of age-specific fertility rate to calculate associated data at the regional level. Capital stock time series is collected from Groningen Growth and Development Centre, and summed up from the national level into the regional level. Capital stock is also used to calculated capital intensity of output, which serves as input variable when modelling GDP based on the Cobb-Douglas production function. It should also be noted that all the monetary units are converted into 2005 US dollars based on the inflations of US dollars from The World Bank.

The production and demand of fossil fuel-based energy at the national level are collected from Statistical Review of World Energy Data (Energy Institute, 2024). The production and demand of biomass energy at the national level are collected from IEA (IEA, 2024), while production and demand of solar and wind energy are from IRENASTAT (IRENA, 2024). We use the concordance between individual country/economy and region to aggregate national energy production and demand data into the regional ones. Market shares of six energy sources in a certain region are calculated as the share of energy demand by each source in total energy demand of the region. In addition, variables in the carbon cycle module are highly relevant to energy production. These variables include carbon emissions from coal energy, gas energy, and oil energy. We use national CO_2 emissions by energy source from IEA (IEA, 2024) and convert national CO_2 emissions into carbon emissions equivalent.

Historic data for key variables in land use and water modules are from FAO-based dataset, FAOSTAT (FAO, 2025d) and AQUASTAT (FAO, 2025a), respectively. For the land module, agricultural land areas, arable land areas, and forest land areas are collected at the national level. In addition, annual production, harvest areas, food demand, and yields of eight food categories are also collected from FAOSTAT (FAO, 2025c). For the water module, water withdrawal by agriculture, by industry, and by domestic sector are collected at the national level. All the national data are aggregated into the regional ones based on the concordance. Percentage of irrigated land is expressed as fraction, and hence use the same calculation procedure of age-specific fertility rate to calculate the percentage of irrigated land at the regional level based on agriculture areas actually irrigated and agricultural land areas.

Lastly, mean species abundance at the regional level is collected from Secretariat of the Convention on Biological Diversity and Netherlands Environmental Assessment Agency (Secretariat of the Convention on Biological Diversity and Netherlands Environmental Assessment Agency, 2007).

Appendix 1: Parameterization of the Baseline Scenarios

This parameterization follows the procedure described in Moallemi et al. (2022) for the calibration of the FeliX model to the SSP-RCP baseline scenarios obtained from the AR6 Scenario Database. These parameters were chosen by the modeling team as they best represent the SSP narratives, and the calibrated values were checked for their compliance with the narratives. For instance, *Normal Fertility Variation*, which represents the reference value of the fertility rate, is lower in the Optimistic, SSP1-like scenario, yet higher in the Pessimistic, SSP3-like scenario.

Parameter	**Reference**	**Optimistic**	**Pessimistic**
Birth Gender Fraction Variation	0.515	0.508	0.511

Normal Fertility Variation	2.630	1.689	3.101
Life Expectancy Variation	65.680	66.668	58.512
Secondary education enrollment Variation [male, "10–14"]	1.000	1.000	1.000
Secondary education enrollment Variation [female, "10–14"]	0.900	1.000	1.000
Secondary education enrollment Variation [male, "15–19"]	0.850	1.000	0.438
Secondary education enrollment Variation [female, "15–19"]	0.850	1.000	0.400
Tertiary education enrollment Variation [male]	0.390	0.690	0.392
Tertiary education enrollment Variation [female]	0.400	0.499	0.381
Persistence Tertiary Variation [male]	0.806	0.880	0.642
Persistence Tertiary Variation [female]	0.829	0.999	0.629
Capital Elasticity Output Variation	0.425	0.478	0.279
Effect of GDP on Urban Land Requirement l Variation	1.250	1.125	0.938
Effect of GDP on Urban Land Requirement x_0 Variation	5.000	5.500	6.250
Max Energy Demand per Capita Variation	0.000002	0.0000014	0.0000019
Price Elasticity of Demand Oil Variation	0.600	0.450	1.000
Price Elasticity of Demand Gas Variation	0.540	0.945	0.638
Price Elasticity of Demand Coal Variation	0.890	0.801	1.250
Price Elasticity of Demand Wind and Solar Variation	1.000	1.250	0.500
Price Elasticity of Demand Biomass Variation	0.800	0.800	1.200
Reference Change in Fossil Fuel Market Share Variation	1.000	1.800	2.200

Reference Change in Market Share Solar Variation	8.000	8.125	1.000
Reference Change in Market Share Wind Variation	6.000	2.250	1.000
Reference Change in Market Share Biomass Variation	3.250	5.250	6.000
Relative Productivity of Investment in Fossil Fuel Production Compared to Exploration Variation	10	10	10
Relative Productivity of Investment in Oil Exploration Variation	1.000	0.500	0.800
Relative Productivity of Investment in Gas Exploration Variation	1.250	0.938	1.438
Relative Productivity of Investment in Coal Exploration Variation	0.150	0.113	0.173
SSP Demographic Variation Time	5	10	10
SSP Economic Variation Time	5	10	10
SSP Energy Demand Variation Time	5	10	10
SSP Energy Technology Variation Time	5	10	10
SSP Energy Production Variation Time	5	10	10
SSP Land Use Change Variation Time	5	10	10
SSP Food and Diet Variation Time	5	10	10
RCP Scenario	3	1	4
Climate Policy Scenario	0	1	0
Carbon Price Slope	5	6	0
Climate Action Year	2020	2025	2100
Land Mitigation Policy Multiplier	0.5	0.07	0
Reference CO_2 Removal Rate	3.70×10^7	1.75×10^7	0.00×10^0

References

Aanegola, R., Nakamura Sakai, S., & Kumar, N. (2022). Longitudinal analysis of the determinants of life expectancy and healthy life expectancy: A causal approach. *Healthcare Analytics*, *2*, 100028. https://doi.org/10.1016/j.health.2022.100028

Armington, P. S. (1969). A Theory of Demand for Products Distinguished by Place of Production. *Staff Papers - International Monetary Fund*, *16*(1), 159. https://doi.org/10.2307/3866403

Bar-Haim, E., Chauvel, L., Gornick, J. C., & Hartung, A. (2023). The Persistence of the Gender Earnings Gap: Cohort Trends and the Role of Education in Twelve Countries. *Social Indicators Research*, *165*(3), 821–841. https://doi.org/10.1007/s11205-022-03029-x

Bressler, R. D., Moore, F. C., Rennert, K., & Anthoff, D. (2021). Estimates of country level temperature-related mortality damage functions. *Scientific Reports*, *11*(1), 20282. https://doi.org/10.1038/s41598-021-99156-5

Burke, M., Hsiang, S. M., & Miguel, E. (2015). Global non-linear effect of temperature on economic production. *Nature*, *527*(7577), 235–239. https://doi.org/10.1038/nature15725

Butz, W. P., Lutz, W., & Sendzimir, J. (Eds.). (2014). *Education and differential vulnerability to natural disasters* (Special Issue, Ecology and Society, Vol. 19). Resilience Alliance.

Byers, E., Krey, V., Kriegler, E., Riahi, K., Schaeffer, R., Kikstra, J., Lamboll, R., Nicholls, Z., Sandstad, M., Smith, C., van der Wijst, K., Al -Khourdajie, A., Lecocq, F., Portugal-Pereira, J., Saheb, Y., Stromman, A., Winkler, H., Auer, C., Brutschin, E., … van Vuuren, D. (2022). *AR6 Scenarios Database* (Version 1.1) [Dataset]. Integrated Assessment Modeling Consortium & International Institute for Applied Systems Analysis. https://doi.org/10.5281/ZENODO.5886911

Chotikapanich, D., Valenzuela, R., & Prasada Rao, D. S. (1997). Global and regional inequality in the distribution of income: Estimation with limited and incomplete data. *Empirical Economics*, *22*(4), 533–546. https://doi.org/10.1007/BF01205778

Crespo Cuaresma, J., Fengler, W., Kharas, H., Bekhtiar, K., Brottrager, M., & Hofer, M. (2018). Will the Sustainable Development Goals be fulfilled? Assessing present and future global poverty. *Palgrave Communications*, *4*(1), 29. https://doi.org/10.1057/s41599-018-0083-y

Davidsen, P. I., Sterman, J. D., & Richardson, G. P. (1990). A petroleum life cycle model for the United States with endogenous technology, exploration, recovery, and demand. *System Dynamics Review*, *6*, 66–93.

Desai, M., Sen, A., Boltvinik, J., & UNDP Regional Project to Overcome Poverty in Latin America and the Caribbean. (1992). *Social progress index: A proposal*. United Nations Development Programme (UNDP).

Dietz, S., & Stern, N. (2015). Endogenous Growth, Convexity of Damage and Climate Risk: How Nordhaus' Framework Supports Deep Cuts in Carbon Emissions. *The Economic Journal*, *125*(583), 574–620. https://doi.org/10.1111/ecoj.12188

Dixon, P. M., Weiner, J., Mitchell-Olds, T., & Woodley, R. (1987). Bootstrapping the Gini Coefficient of Inequality. *Ecology*, *68*(5), 1548–1551. https://doi.org/10.2307/1939238

DoE. (2022). *Land-Based Wind Market Report*. US Department of Energy (DoE), Office of Energy Efficiency and Renewable Energy.

Dollar, D., & Kraay, A. (2003). Institutions, trade, and growth. *Journal of Monetary Economics*, *50*(1), 133–162. https://doi.org/10.1016/S0304-3932(02)00206-4

Donadelli, M., Grüning, P., Jüppner, M., & Kizys, R. (2021). Global temperature, R&D expenditure, and growth. *Energy Economics*, *104*, 105608. https://doi.org/10.1016/j.eneco.2021.105608

Dong, H., Mangino, J., McAllister, T. A., Hatfield, J. L., Johnson, D. E., Lassey, K. R., de Lima, M. A., Romanovskaya, A., Bartram, D., Gibb, D., & Martin, Jr., J. H. (2009). Chapter 10: Emissions from Livestock and Manure Management. In *2006 IPCC Guidelines for National Greenhouse Gas Inventories: Vol. Volume 4: Agriculture, Forestry and Other Land Use*.

Dumas, M., Frossard, E., & Scholz, R. W. (2011). Modeling biogeochemical processes of phosphorus for global food supply. *Chemosphere*, *84*(6), 798–805. https://doi.org/10.1016/j.chemosphere.2011.02.039

Eker, S. (2016). *Dealing with Uncertainties in the Dutch Gas Sector: An Exploratory Modeling and Analysis Approach* [Delft University of Technology]. https://doi.org/10.4233/UUID:1C03192C-135D-4DB0-8DF9-49CF1D52540B

Eker, S., Reese, G., & Obersteiner, M. (2019). Modelling the drivers of a widespread shift to sustainable diets. *Nature Sustainability*, *2*(8), 725–735. https://doi.org/10.1038/s41893-019-0331-1

Energy Institute. (2024). *Statistical Review of World Energy 2024 (73rd edition)*.

Enevoldsen, P., & Jacobson, M. Z. (2021). Data investigation of installed and output power densities of onshore and offshore wind turbines worldwide. *Energy for Sustainable Development*, *60*, 40–51. https://doi.org/10.1016/j.esd.2020.11.004

FAO. (2008). *FAO methodology for the measurement of food deprivation: Updating the minimum dietary energy requirements*. Statistics Division, Food and Agriculture Organization (FAO) of the United Nations. https://www.fao.org/fileadmin/templates/ess/documents/food_security_statistics/metadata/undernourishment_methodology.pdf
FAO. (2014). *Revision of the methodology for the estimation of the prevalence of undernourishment*. https://www.fao.org/fileadmin/templates/ess/documents/apcas25/APCAS-14-8.2-PoU-Method.pdf
FAO. (2015). *Food loss and waste facts*.
FAO. (2025a). *AQUASTAT Dissemination System, Food and Agriculture Organization (FAO)* [Dataset]. https://data.apps.fao.org/aquastat/?lang=en
FAO. (2025b). *FAOSTAT Database Emissions totals domain, Food and Agriculture Organization (FAO)* (Version updated on November 14, 2024) [Dataset]. https://www.fao.org/faostat/en/#data/GT
FAO. (2025c). *FAOSTAT Database Food Balance Sheets, Food and Agriculture Organization (FAO)* (Version updated on August 19, 2024) [Dataset].
FAO. (2025d). *FAOSTAT Database Land Use domain, Food and Agriculture Organization (FAO)* (Version updated on August 19, 2024) [Dataset]. https://www.fao.org/faostat/en/#data/RL
Feenstra, R. C., Inklaar, R., & Timmer, M. P. (2015). The Next Generation of the Penn World Table. *American Economic Review*, *105*(10), 3150–3182. https://doi.org/10.1257/aer.20130954
Fiddaman, T. S. (2002). Exploring policy options with a behavioral climate–economy model. *System Dynamics Review*, *18*(2), 243–267. https://doi.org/10.1002/sdr.241
Fosu, A. K. (2010). Inequality, Income, and Poverty: Comparative Global Evidence. *Social Science Quarterly*, *91*(5), 1432–1446. https://doi.org/10.1111/j.1540-6237.2010.00739.x
Hegerl, G. C., Zwiers, F. W., Braconnot, P., Gillett, N. P., Luo, Y., Marengo Orsini, J. A., Nicholls, N., Penner, J. E., & Stott, P. A. (2007). *Understanding and Attributing Climate Change* (Climate Change 2007: The Physical Science Basis. Contribution of Working Group I to the Fourth Assessment Report of the Intergovernmental Panel on Climate Change). Cambridge University Press.
Hughes, B. B. (2015, July). *International Futures (IFs) ECONOMIC MODEL DOCUMENTATION*. Frederick S. Pardee Institute for International Futures, University of Denver. https://pure.iiasa.ac.at/id/eprint/11267/1/RP-14-001.pdf
Huppmann, D., Rogelj, J., Kriegler, E., Krey, V., & Riahi, K. (2018). A new scenario resource for integrated 1.5 °C research. *Nature Climate Change*, *8*(12), 1027–1030. https://doi.org/10.1038/s41558-018-0317-4
IEA. (2024). *World Energy Statistics and Balances* (No. IEA, Paris) [Dataset]. https://www.iea.org/data-and-statistics/data-product/world-energy-statistics-and-balances
IEA (2025). Greenhouse Gas Emissions from Energy Data Explorer. Available at: https://www.iea.org/data-and-statistics/data-tools/greenhouse-gas-emissions-from-energy-data-explorer
IPCC. (2000). *Good Practice Guidance and Uncertainty Management in National Greenhouse Gas Inventories: CH4 Emissions from Solid Waste Disposal* (IPCC National Greenhouse Gas Inventories Programme).
IPCC (Ed.). (2014). *Climate change 2014: Mitigation of climate change Working Group III contribution to the fifth assessment report of the Intergovernmental Panel on Climate Change*. Cambridge university press.
IPCC. (2023). *Climate Change 2021 – The Physical Science Basis: Working Group I Contribution to the Sixth Assessment Report of the Intergovernmental Panel on Climate Change* (1st ed.). Cambridge University Press. https://doi.org/10.1017/9781009157896
IPCC, Eggleston, H. S., Buendia, L., Miwa, K., Ngara, T., & Tanabe, K. (Eds.). (2006). *2006 IPCC guidelines for national greenhouse gas inventories*. Institute for Global Environmental Strategies.
IRENA. (2024). *IRENASTAT Online Data Query Tool of International Renewable Energy Agency (IRENA)* [Dataset]. https://www.irena.org/Data/Downloads/IRENASTAT
Kalkuhl, M., & Wenz, L. (2020). The impact of climate conditions on economic production. Evidence from a global panel of regions. *Journal of Environmental Economics and Management*, *103*, 102360. https://doi.org/10.1016/j.jeem.2020.102360
Kemp-Benedict, E. (2001). *Income distribution and poverty: Methods for using available data in global analysis*. PoleStar Technical Notes.
Kot, S. M. (2016). *Estimates of the world distribution of personal incomes based on country sample clones* (No. No. 11/2016 (41); GUT FME Working Paper Series A). Gdańsk University of Technology, Faculty of Management and Economics. https://www.econstor.eu/bitstream/10419/173337/1/wp-gut-fme-a-41-Kot.pdf
Lakner, C., Mahler, D. G., Negre, M., & Prydz, E. B. (2022). How much does reducing inequality matter for global poverty? *The Journal of Economic Inequality*, *20*(3), 559–585. https://doi.org/10.1007/s10888-021-09510-w

LBL. (2025). *Wind Energy Capital Expenditures* [Dataset]. https://emp.lbl.gov/wind-energy-capital-expenditures-capex
Leach, N. J., Jenkins, S., Nicholls, Z., Smith, C. J., Lynch, J., Cain, M., Walsh, T., Wu, B., Tsutsui, J., & Allen, M. R. (2021). FaIRv2.0.0: A generalized impulse response model for climate uncertainty and future scenario exploration. *Geoscientific Model Development*, *14*(5), 3007–3036. https://doi.org/10.5194/gmd-14-3007-2021
Leclère, D., Obersteiner, M., Barrett, M., Butchart, S. H. M., Chaudhary, A., De Palma, A., DeClerck, F. A. J., Di Marco, M., Doelman, J. C., Dürauer, M., Freeman, R., Harfoot, M., Hasegawa, T., Hellweg, S., Hilbers, J. P., Hill, S. L. L., Humpenöder, F., Jennings, N., Krisztin, T., … Young, L. (2020). Bending the curve of terrestrial biodiversity needs an integrated strategy. *Nature*, *585*(7826), 551–556. https://doi.org/10.1038/s41586-020-2705-y
Liu, Q., Gao, L., Guo, Z., Dong, Y., Moallemi, E. A., Eker, S., Yang, J., Obersteiner, M., & Bryan, B. A. (2023). Robust strategies to end global poverty and reduce environmental pressures. *One Earth*, *6*(4), 392–408. https://doi.org/10.1016/j.oneear.2023.03.007
Lopez, A. D., & Murray, C. C. J. L. (1998). The global burden of disease, 1990–2020. *Nature Medicine*, *4*(11), 1241–1243. https://doi.org/10.1038/3218
Lopez, J. H., & Luis, S. (2006). *A Normal Relationship? Poverty, Growth, and Inequality*. The World Bank. http://hdl.handle.net/10986/8791
Lutz, W., Goujon, A., KC, S., Stonawski, M., & Stilianakis, N. (2018). *Demographic and human capital scenarios for the 21st century: 2018 assessment for 201 countries.* European Commission, Joint Research Centre, Publications Office of the European Union. https://data.europa.eu/doi/10.2760/835878
Lutz, W., Muttarak, R., & Striessnig, E. (2014). Universal education is key to enhanced climate adaptation. *Science*, *346*(6213), 1061–1062. https://doi.org/10.1126/science.1257975
Lutz, W., Striessnig, E., Dimitrova, A., Ghislandi, S., Lijadi, A., Reiter, C., Spitzer, S., & Yildiz, D. (2021). Years of good life is a well-being indicator designed to serve research on sustainability. *Proceedings of the National Academy of Sciences*, *118*(12), e1907351118. https://doi.org/10.1073/pnas.1907351118
MacDonald, G. K., Bennett, E. M., Potter, P. A., & Ramankutty, N. (2011). Agronomic phosphorus imbalances across the world's croplands. *Proceedings of the National Academy of Sciences*, *108*(7), 3086–3091. https://doi.org/10.1073/pnas.1010808108
Meadows, D., Richardson, J., & Bruckmann, G. (1983). Groping in the dark: The first decade of global modelling. *Strategic Management Journal*, *4*(4), 384–385. https://doi.org/10.1002/smj.4250040412
Meinshausen, M., Nicholls, Z. R. J., Lewis, J., Gidden, M. J., Vogel, E., Freund, M., Beyerle, U., Gessner, C., Nauels, A., Bauer, N., Canadell, J. G., Daniel, J. S., John, A., Krummel, P. B., Luderer, G., Meinshausen, N., Montzka, S. A., Rayner, P. J., Reimann, S., … Wang, R. H. J. (2020). The shared socio-economic pathway (SSP) greenhouse gas concentrations and their extensions to 2500. *Geoscientific Model Development*, *13*(8), 3571–3605. https://doi.org/10.5194/gmd-13-3571-2020
Mendez Ramos, F. (2019). *Uncertainty in Ex-Ante Poverty and Income Distribution: Insights from Output Growth and Natural Resource Country Typologies*. World Bank, Washington, DC. https://doi.org/10.1596/1813-9450-8841
Mincer, J. (1989). Human Capital and the Labor Market: A Review of Current Research. *Educational Researcher*, *18*(4), 27–34. https://doi.org/10.3102/0013189X018004027
Moallemi, E. A., Eker, S., Gao, L., Hadjikakou, M., Liu, Q., Kwakkel, J., Reed, P. M., Obersteiner, M., Guo, Z., & Bryan, B. A. (2022). Early systems change necessary for catalyzing long-term sustainability in a post-2030 agenda. *One Earth*, *5*(7), 792–811. https://doi.org/10.1016/j.oneear.2022.06.003
Naiken, L. (2002). *Keynote Paper: FAO methodology for estimating the prevalence of undernourishment* (Measurement and Assessment of Food Deprivation and Undernutrition) [Proceedings of the International Scientific Symposium]. Agriculture and Economic Development Analysis Division, Food and Agriculture Organization (FAO) of the United Nations. https://www.fao.org/4/y4249e/y4249e06.htm
Nicholls, Z. R. J., Meinshausen, M., Lewis, J., Gieseke, R., Dommenget, D., Dorheim, K., Fan, C.-S., Fuglestvedt, J. S., Gasser, T., Golüke, U., Goodwin, P., Hartin, C., Hope, A. P., Kriegler, E., Leach, N. J., Marchegiani, D., McBride, L. A., Quilcaille, Y., Rogelj, J., Salawitch, R. J., Samset, B. H., Sandstad, M., Shiklomanov, A. N., Skeie, R. B., Smith, C. J., Smith, S., Tanaka, K., Tsutsui, J., and Xie, Z., 2020. Reduced Complexity Model Intercomparison Project Phase 1: introduction and evaluation of global-mean temperature response. Geosci. Model Dev., 13, 5175–5190. https://doi.org/10.5194/gmd-13-5175-2020
Nordhaus, W. (2007, October). *Accompanying Notes and Documentation on Development of DICE-2007 Model: Notes on DICE-2007.delta.v8*. Yale University. https://people.anu.edu.au/jack.pezzey/Nordhaus2007DICEnotes.pdf
Nordhaus, W. D. (1992). The 'Dice' Model: Background and Structure of a Dynamic Integrated Climate-Economy Model of the Economics of Global Warming. *Cowles Foundation Discussion Papers*, 1252.

Nordhaus, W. D. (2017). Revisiting the social cost of carbon. *Proceedings of the National Academy of Sciences*, *114*(7), 1518–1523. https://doi.org/10.1073/pnas.1609244114
NREL. (2025). *Champion Photovoltaic Module Efficiency Chart* [Dataset]. https://www.nrel.gov/pv/module-efficiency
Obersteiner, M., Rydzak, F., Fritz, S., & McCallum, I. (2012). Valuing the Potential Impacts of GEOSS: A Systems Dynamics Approach. In R. Laxminarayan & M. K. Macauley (Eds.), *The Value of Information* (pp. 67–90). Springer Netherlands. https://doi.org/10.1007/978-94-007-4839-2_4
Peters, G. P., & Hertwich, E. G. (2008). CO_2 Embodied in International Trade with Implications for Global Climate Policy. *Environmental Science & Technology*, *42*(5), 1401–1407. https://doi.org/10.1021/es072023k
Polachek, S. W. (Ed.). (2003). *Worker Well-Being and Public Policy* (Vol. 22). Emerald Group Publishing Limited. https://doi.org/10.1016/S0147-9121(2003)22
Ranganathan, J., Vennard, D., Waite, R., Lipinski, B., Searchinger, T., & Dumas, P. (2016). *Shifting Diets for a Sustainable Food Future: Creating a Sustainable Food Future, Installment Eleven*.
Riahi, K., Van Vuuren, D. P., Kriegler, E., Edmonds, J., O'Neill, B. C., Fujimori, S., Bauer, N., Calvin, K., Dellink, R., Fricko, O., Lutz, W., Popp, A., Cuaresma, J. C., Kc, S., Leimbach, M., Jiang, L., Kram, T., Rao, S., Emmerling, J., … Tavoni, M. (2017). The Shared Socioeconomic Pathways and their energy, land use, and greenhouse gas emissions implications: An overview. *Global Environmental Change*, *42*, 153–168. https://doi.org/10.1016/j.gloenvcha.2016.05.009
Rydzak, F., Obersteiner, M., & Kraxner, F. (2010). Impact of Global Earth Observation – Systemic view across GEOSS Societal Benefit Areas. *International Journal of Spatial Data Infrastructures Research*, *5*, 216–243. https://doi.org/10.2902/1725-0463.2010.05.art9
Schipper, A. M., Hilbers, J. P., Meijer, J. R., Antão, L. H., Benítez-López, A., De Jonge, M. M. J., Leemans, L. H., Scheper, E., Alkemade, R., Doelman, J. C., Mylius, S., Stehfest, E., Van Vuuren, D. P., Van Zeist, W., & Huijbregts, M. A. J. (2020). Projecting terrestrial biodiversity intactness with GLOBIO 4. *Global Change Biology*, *26*(2), 760–771. https://doi.org/10.1111/gcb.14848
Secretariat of the Convention on Biological Diversity and Netherlands Environmental Assessment Agency. (2007). *Cross-roads of Life on Earth—Exploring means to meet the 2010 Biodiversity Target. Solution-oriented scenarios for Global Biodiversity Outlook 2.* (Technical Series No. 31, p. 90 pages). Secretariat of the Convention on Biological Diversity.
Skirbekk, V. (2004). Age and Individual Productivity: A Literature Survey. *Vienna Yearbook of Population Research*, *2*, 133–153.
Soergel, B., Kriegler, E., Bodirsky, B. L., Bauer, N., Leimbach, M., & Popp, A. (2021). Combining ambitious climate policies with efforts to eradicate poverty. *Nature Communications*, *12*(1), 2342. https://doi.org/10.1038/s41467-021-22315-9
Springmann, M., Clark, M., Mason-D'Croz, D., Wiebe, K., Bodirsky, B. L., Lassaletta, L., De Vries, W., Vermeulen, S. J., Herrero, M., Carlson, K. M., Jonell, M., Troell, M., DeClerck, F., Gordon, L. J., Zurayk, R., Scarborough, P., Rayner, M., Loken, B., Fanzo, J., … Willett, W. (2018). Options for keeping the food system within environmental limits. *Nature*, *562*(7728), 519–525. https://doi.org/10.1038/s41586-018-0594-0
Sterman, J. D., Fiddaman, T., Franck, T., Jones, A., McCauley, S., Rice, P., Sawin, E., & Siegel, L. (2013). Management flight simulators to support climate negotiations. *Environmental Modelling & Software*, *44*, 122–135. https://doi.org/10.1016/j.envsoft.2012.06.004
Sterman, J., Fiddaman, T., Franck, T., Jones, A., McCauley, S., Rice, P., Sawin, E., & Siegel, L. (2012). Climate interactive: The C-ROADS climate policy model. *System Dynamics Review*, *28*(3), 295–305. https://doi.org/10.1002/sdr.1474
Striessnig, E., Lutz, W., & Patt, A. G. (2013). Effects of educational attainment on climate risk vulnerability. *Ecology and Society*, *18*(1), 16. https://doi.org/10.5751/ES-05252-180116
Sullivan, D. F. (1971). A single index of mortality and morbidity. *HSMHA Health Reports*, *86*(4), 347–354.
The World Bank. (2023). *World Bank Open Data* [Dataset].
UN. (2024). *Regional groups of Member States of United Nations (UN)*. https://www.un.org/dgacm/en/content/regional-groups#
United Nations. (2022). *World Population Prospects 2022, Online Edition* (Version Department of Economic and Social Affairs, Population Division) [Dataset].
Uno, K. (Ed.). (2002). *Economy-Energy-Environment Simulation* (Vol. 20). Kluwer Academic Publishers. https://doi.org/10.1007/0-306-47549-9
USDA. (2020). *USDA Food Composition Databases* [Dataset].
Walsh, B., Ciais, P., Janssens, I. A., Peñuelas, J., Riahi, K., Rydzak, F., Van Vuuren, D. P., & Obersteiner, M. (2017). Pathways for balancing CO2 emissions and sinks. *Nature Communications*, *8*(1), 14856. https://doi.org/10.1038/ncomms14856

Walsh, B. J., Rydzak, F., Palazzo, A., Kraxner, F., Herrero, M., Schenk, P. M., Ciais, P., Janssens, I. A., Peñuelas, J., Niederl-Schmidinger, A., & Obersteiner, M. (2015). New feed sources key to ambitious climate targets. *Carbon Balance and Management*, *10*(1), 26. https://doi.org/10.1186/s13021-015-0040-7

Weitzman, M. L. (2012). GHG Targets as Insurance Against Catastrophic Climate Damages. *Journal of Public Economic Theory*, *14*(2), 221–244. https://doi.org/10.1111/j.1467-9779.2011.01539.x

WHO. (2025). *Length/height-for-age—WHO Child Growth Standards*. https://www.who.int/tools/child-growth-standards/standards/length-height-for-age

Wiedmann, T., & Lenzen, M. (2018). Environmental and social footprints of international trade. *Nature Geoscience*, *11*(5), 314–321. https://doi.org/10.1038/s41561-018-0113-9

Wittgenstein Centre. (2023). *Wittgenstein Centre human capital data explorer* [Dataset]. http://dataexplorer.wittgensteincentre.org/wcde-v2/

Wullschleger, S. D., Post, W. M., & King, A. W. (1995). On the Potential for a CO2 Fertilization Effect in Forests: Estimates of the Biotic Growth Factor Based on 58 Controlled-Exposure Studies. In G. M. Woodwell & F. T. Mackenzie (Eds.), *Biotic Feedbacks in the Global Climatic System* (pp. 85–107). Oxford University PressNew York, NY. https://doi.org/10.1093/oso/9780195086409.003.0005

Yin, X., & Struik, P. C. (2010). Modelling the crop: From system dynamics to systems biology. *Journal of Experimental Botany*, *61*(8), 2171–2183. https://doi.org/10.1093/jxb/erp375

Zellner, A., Kmenta, J., & Dreze, J. (1966). Specification and Estimation of Cobb-Douglas Production Function Models. *Econometrica*, *34*(4), 784. https://doi.org/10.2307/1910099